NORTHWESTERN UNIVERSITY

Non-Equilibrium Thermodynamics of Quench and Partition (Q&P) Steels

A DISSERTATION

SUBMITTED TO THE GRADUATE SCHOOL
IN PARTIAL FULFILMENT OF THE REQUIREMENTS

for the degree

DOCTOR OF PHILOSOPHY

Field of Materials Science and Engineering

By

Amit Kishan Behera

EVANSTON, ILLINOIS

June 2018

ABSTRACT

Non-equilibrium Thermodynamics of Quench and Partition (Q&P) Steels

Amit Kishan Behera

In support of a scientific foundation for the predictive design of composition and processing of quench and partition (Q&P) martensite/austenite TRIP steels, theory of coupled diffusional/displacive transformation is experimentally calibrated to control austenite carbon content and its associated mechanical stability. Under paraequilibrium constraint, the calibration quantifies an effective BCC stored energy that incorporates both stored and dissipated energy associated with displacive interfacial motion during the partitioning treatment. Consistent with prior study of bainitic transformations, the effective stored energy is found to decrease linearly with partitioning temperature, attributed to the effect of dislocation recovery on the forest hardening contribution to interfacial friction. The calibrations are based on highly accurate experimental measurements using electron microscopy, high-energy x-ray diffraction and 3D atom probe tomography to quantify the amount and carbon content of retained austenite as a function of Q&P treatment. Varying the initial quench temperature to vary the initial retained austenite amount, it is demonstrated that the effective BCC stored energy changes with the direction of motion of the interface in association with a sign change of the dissipation contribution, favoring greater C partitioning for BCC->FCC motion. The minimum time for completion of partitioning at the partitioning temperature is consistent with DICTRA paraequilibrium diffusion simulations incorporating the effective stored energy. Measuring retained austenite mechanical stability by the characteristic Ms^{σ} temperature below which transformation controls yielding, martensite nucleation theory is calibrated using the forest hardening friction derived from the partitioning experiments to define the characteristic

nucleation site potency in the retained austenite. Model predictions of austenite carbon content and stability were validated using a set of new designed alloys with individually optimized Q&P cycles.

Comparison of the stress-strain curves of the Q&P martensite/austenite samples with fully martensitic material shows little influence of the austenite on yield strength, but a dramatic reduction of the ultimate tensile strength by transformation softening which greatly reduces initial strain hardening, retaining higher hardening to higher strains for greatly enhanced flow stability. An unusual correlation between Ms^{σ} and the temperature of maximum ductility is attributed to a bimodal austenite stability associated with two morphologies of blocky vs thin-film in the martensite microstructure.

A principal limitation of the Q&P martensite/austenite steels relative to their bainite/austenite counterparts is the more rapid tempering of martensite leading to a major fraction of the alloy carbon being lost to carbides. A preliminary parametric analysis correlating rate of carbide precipitation to paraequilibrium cementite driving force and coarsening rate constant predicts Cr as the most effective alloying element to retard carbide precipitation, with some support from literature data. Predictive design of carbide-free Q&P martensite/austenite steels could double the amount of optimal stability austenite for greatly enhanced TRIP to achieve useful ductility of significantly higher strength levels.

ACKNOWLEDGEMENTS

In my four and a half years at Northwestern university, I have come across many people that includes fellow graduate students, professors, lab managers and friends who have contributed in innumerable ways to the success of my PhD adventure. Looking back, it would have been impossible to make it through graduate school without the steady support and amazing company of friends and family. I would like to express my heartfelt gratitude towards all those who have supported me and my work here at Northwestern.

First and foremost, I will be eternally thankful to you, Prof. Olson for providing me with the opportunity to pursue graduate research under his guidance and advising me over the years to learn about the field of computational material science. Your endless knowledge in the field of materials science especially steels has amazed me right from the first meeting and continues to increasingly amaze me as I understand little by little more of it. Your ever-enthusiastic attitude towards work and inspiring personality has always been a key motivation for everyone in the steel research group. I am indebted to you for introducing me to the world of computational materials design and helping me pursue my aim of doing industrially relevant application oriented research. And I shall remember to always…Expect Victory!

Thank you to all my thesis committee members for their support and guidance. Dr. Shrikant Bhat: I am grateful for your advice over the years regarding my research work and overall professional development. I really appreciate your constant encouragement to explore the science behind Q&P steels and not just aim for better properties. Prof. Voorhees and Prof. Chung: Thank you for agreeing to serve on my thesis committee and for your useful insights regarding my

work. I am also thankful to late Prof. Morris Fine for serving on my qualifying committee and offering his useful suggestions.

I am deeply obliged to the Research Engineers at ArcelorMittal Global R&D in East Chicago especially in the product development team. The assistance of Dr. Rashmi Mohanty, Dr. Jun Hyun and Dr. Damon Panahi over the years in providing the raw materials, performing heat treatments and dilatometer experiments was critical to the completion of my thesis research. In addition to these, numerous useful scientific discussions with Dr. Panahi and other researchers at AM helped shape up my research objectives. Dr. Narayan Pottore: I am grateful to you for taking the time for our research discussions and for ensuring that I get all the possible assistance from AM to complete my research work.

Thank you to all the present and past members of the Olson research group who have shared time with me in the last four and half years at NU. Jiayi and Dana: Thanks for your help in the early years of PhD life. Dr. Komai: I really appreciate all your help on innumerable occasions whether it be work related or otherwise. Looking forward to working with you on the other side. Nick: Thanks for sharing the expectations of steel research in the Steel research group. Andrew: It was great fun having the endless discussions about precipitates in Al, Atom probe, TEM and so much more. Also, cheers to your beer enthusiasm and those home brews! Fuyao: It was great to have another group member in the same year. It was great to share office space, endless jokes, pokemons… although I am still sad that I learnt about your marriage from ‘rumors’. Fan: Forever baby Fan! It was always nice to have a relaxing conversation with you and see your exciting results on Ti. Good luck going forward! Chuan, Kazu and Clay: Thanks guys for keeping the group spirit high! Keep marching ahead and expect victory! Make Steel Proud!

I am grateful to all the department faculty members, lab managers and office staff for their help over the years. Thank you, Mark Seniw for all your help with tensile testing equipment and for the honest discussions about politics! Thank you, Karl, Ben and Eric for all your assistance with NUANCE facilities over the years. Carla, thanks for maintaining the OMM lab facility and your help restoring those old equipment. Dieter, I am grateful for your assistance with the LEAP experiments and data analysis.

A big cheer to all my friends here at NU over the years. Without you guys, it would have been impossible to live through grad school and have the most amazing memories. To my friends in the department; Karl, Karen, Charlotte, HK, Vinay, Shawn, Yue, Shannon, Janak and so many others… it was fun growing old with you guys! We aged well with time going from birthday parties for everyone in the first year to seeing each other only at department coffee hours in the last year…lol. The highlight of my NU days would be the time with G-ISA, IGSSA and Multi-Cultural Dialogue group (MDG). I am thankful for meeting some of my best friends at NU through these groups. I am lucky to have met Miss Fujisaki and Rose, Ann, Priyankar, Partha, Sanket, Ettore, Vidushi, Madhurya and so many others and share their friendship over the years.

I am forever grateful to my loving huge family for their constant support and encouragement to follow my dreams. I love and really respect you Bapa for your inspiring work and for always making me realize the bigger purpose of life. To my ‘Mummy’, your determination and prayers wishing me to be successful is one of the key reasons for my achievements. I am fortunate to be part to two big and amazing families; ‘Sushling’ and ‘Kalpataru’ family and have the support and blessings of so many elder family members along with the love of younger siblings.

Finally, thank you God for this privileged life and all your blessings! Jai Jagannath!

Table of Contents

LIST OF FIGURES

LIST OF TABLES

Chapter 1. Introduction and Background

Automotive manufacturing is one of the major global industries that drives innovation and research in the field of structural materials which primarily includes iron based alloys, aluminum and titanium alloys. The demands of the industry are determined by governmental regulations, consumer choices and competition in the market among other things. Some of these demands such as improved fuel efficiency, better driver safety, ensure product reliability and increase affordability have resulted in the development of a wide range of material solutions for automotive applications. Some of the solutions incorporated are based on developing newer lightweight materials, utilization of downgauging, product design optimization etc. Steels are one of the most used materials in the car body and the type of steel used depends on the specific part of the car body. The desired strength-ductility combinations for the critical parts of the car are shown in Figure 1 [1]. High strength with minimal deformation during crash is required for maximizing passenger safety while excellent formability or ductility is required for deep drawn parts. A combination of both is required for components that are needed for energy absorption, durability and load bearing strength of the car. Modern cars use a wide variety of materials in their manufacturing. Some of the prominent materials used for light weighting purposes are Aluminum and Titanium alloys. Carbon fiber is also another alternative that has significant lightweight benefits. In addition to these new material systems, new high strength steel grades have also been under development to compete with these alternatives on basis of cost, performance and manufacturability. A study of these materials as percentage of the total car weight over the years is shown in Figure 2(a) [2]. Although the fraction usage of aluminum alloys and other newer metal systems is on the rise, the amount of medium, high and advanced high strength steels (AHSS) in cars has also been constantly increasing. Figure 2(b) shows the

increase in absolute AHSS content along with the percentage of overall car weight as a function of model year of North American vehicles [3]. The data suggests the potential of AHSS as a cost effective lightweight and high-performance material that would constitute a major fraction of the automobile body-in-white (BIW).

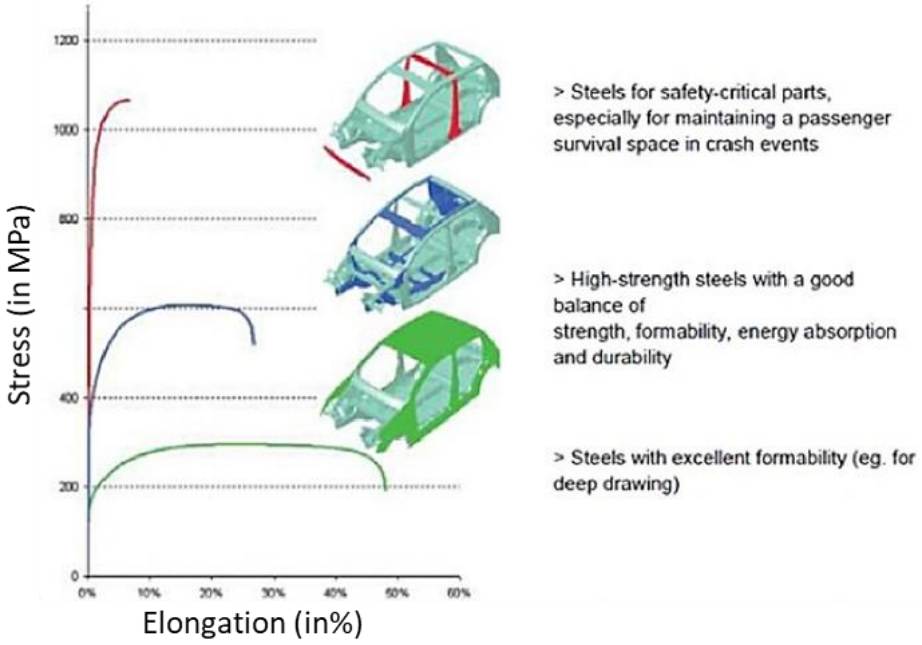

Figure 1: Stress versus elongation for different types of steel categorized according to their usage in the car body structure [1]

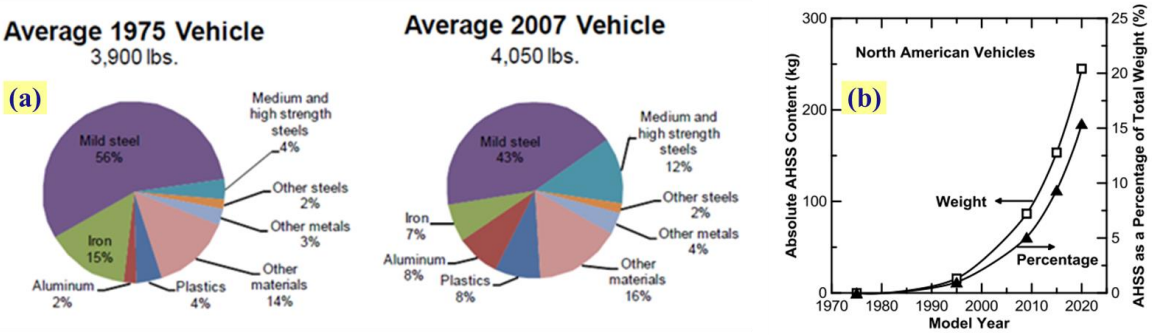

Figure 2(a) Comparison of materials used by weight in average 1975 vs 2007 vehicle [2], (b) AHSS content in North American vehicles [3]

1.1. Advanced high strength steels (AHSS)

At the core of the development of modern automotive steels with improved properties is the effort focused on Advanced high strength steels or AHSS. This new category of steels has remarkable mechanical properties that includes very high tensile strength along with a considerable amount of ductility. These steels are not lighter than other steel types but due to their strength it is possible to use thinner gauges in automotive applications. This results in light weighting benefits in addition to the regular advantages of steel because of its affordability, performance, manufacturability and recyclability. In the automotive industry, current trends show the potential replacement of traditional high strength steel (HSS) with advanced high strength steel (AHSS) with similar levels of formability.

The development of automotive AHSS can be categorized into three generations as marked in Figure 3 [2]. The ‘first’ generation of AHSS were low alloyed steels with good combination of tensile strength and total elongation. These included the widely used dual phase (DP) steels, high strength low alloy (HSLA) steels, transformation induced plasticity (TRIP) steels and others. The ‘second’ generation of austenitic AHSS was explored next and demonstrated remarkably high strength values along with significant high elongation standards. These included the fully austenitic TRIP steels as well as the twinning induced plasticity (TWIP) steels which had a considerable amount of alloying additions (12%-30% Mn) that made the steel too expensive for practical applications along with issues of mass production and weldability. Also denoted in Figure 3 is a ‘Generation 0’ of the high-strength austenitic TRIP steels developed in 1967 [4,5] that triggered high scientific interest in the TRIP phenomenon. The cost of austenitic steels led to the ‘third’ generation of AHSS which were intended to have better property combinations than

the first generation while maintaining the low alloying conditions to be cost-effective. The third generation comprises of the carbide free bainitic steels, medium manganese steels (5-10wt%) and the quench and partition (Q&P) steels. These steels are more feasible for industrial applications and have been commercialized in some cases by industrial manufacturers.

Thermomechanical processing of AHSS grades is crucial in generating the requisite microstructure that results in the desired mechanical properties. Most of the processing cycles start with a starting austenitization (full or partial) step and then cooling to different temperature regimes. The wide number of microstructural phases in iron-based alloys makes it possible for an array of resulting microstructures depending on the cooling rate. Subsequent heat treatment after the cooling step could vary from isothermal annealing at a fixed temperature to interrupted quenching and isothermal annealing at higher temperature depending on the desired microstructure. The microstructure after thermomechanical processing can constitute a mixture of the following phases: ferrite, bainite, retained austenite, martensite, carbides. The final steel properties are dependent on the composition, phase fraction and distribution of these phases in the microstructure.

AHSS are specifically developed to use as structural members in automotive applications. Some of the key attributes of AHSS in this regard include high strength and enhanced ductility, toughness, crashworthiness and formability. Amongst the different grades of AHSS, the strength levels can vary from 300MPa to as high as 1800MPa depending on the microstructure of the material. Significant ductility along with very high strength is also achievable by use of TWIP or TRIP phenomenon. Longer fatigue life and higher fatigue strength levels are observed for AHSS compared to lower strength grade steels.

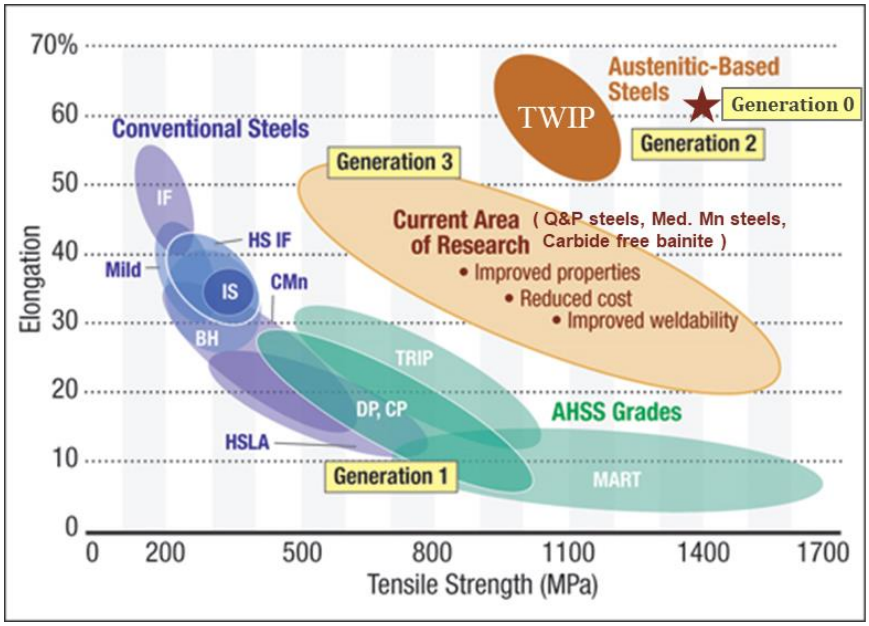

Figure 3: Total elongation versus tensile stress plot showing the different generations of AHSS

Crashworthiness of a material depends on both its ability to resist plastic deformation and its ability to absorb energy during crash. Thus, a material with high strength and high toughness is desirable for practical use. TRIP, TWIP and Austenitic stainless steels are some of the AHSS grades most suitable for these applications. Formability is defined as the ability of a material to be formed into simple and complex shapes by deformation processes. It is measured by using a variety of tests such as uniaxial tension tests, hemispherical punch forming, deep drawing and hole expansion tests. Depending on the AHSS grade, it is possible to combine good formability with high strength. A comparison of AHSS with aluminum in terms of application in the automobile body is shown in Figure 4(a). A major fraction of the body-in-white uses AHSS while the powertrain and heat transfer components preferably use aluminum [6]. The percentage of flat rolled AHSS in the curb weight of a car can be seen to be on constant rise over the years compared to other materials [6] as shown in Figure 4(b).

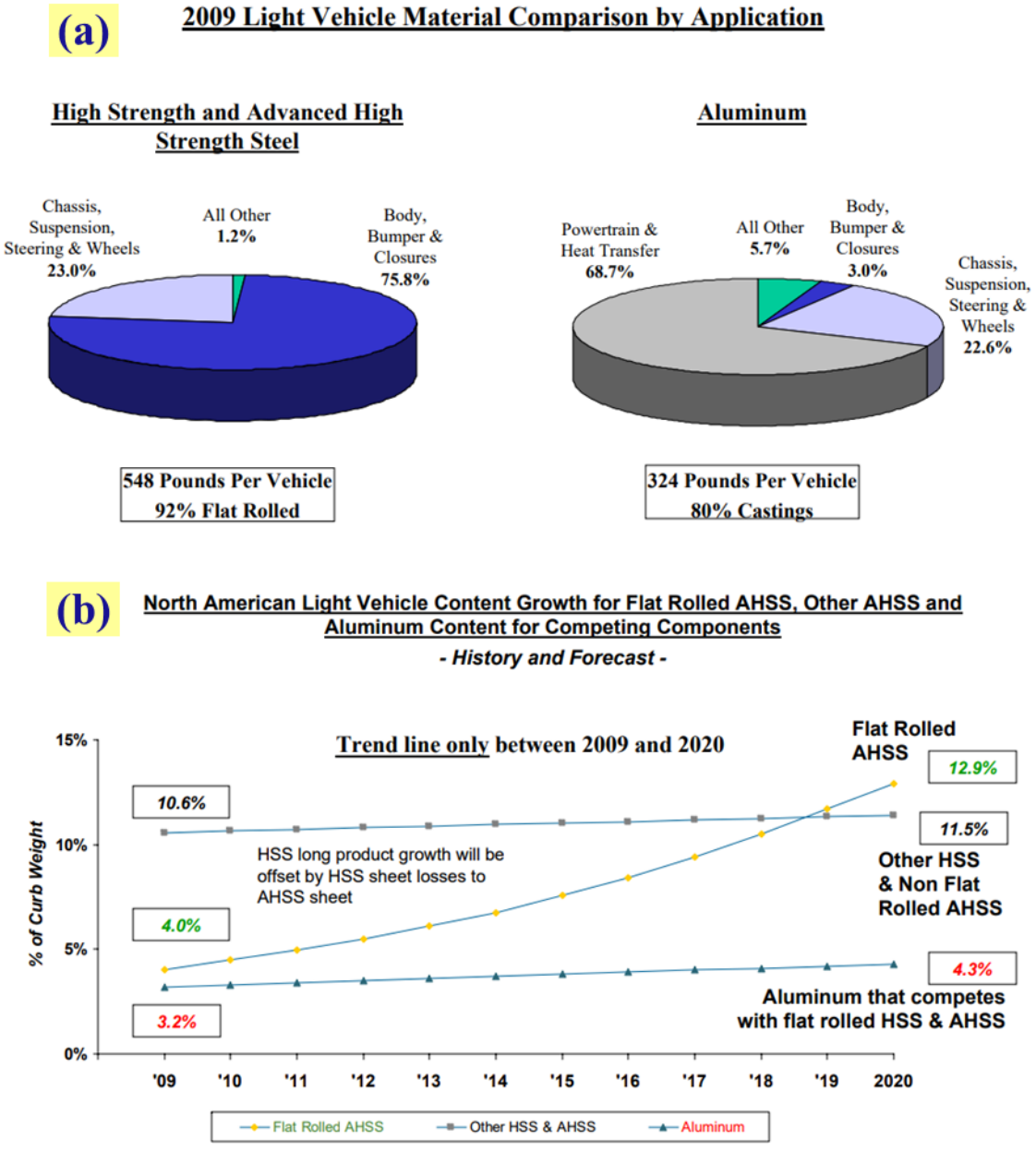

Figure 4: (a) 2009 light vehicle material comparison by application,
(b) North American light vehicle material content growth for flat rolled AHSS etc [6]

1.2. Transformation induced plasticity (TRIP)

Transformation induced plasticity is one the most exciting phenomenon in steel metallurgy that enables unique strength ductility combinations in high strength steels. TRIP refers to a deformation mechanism in which austenite transforms to hard martensite during mechanical deformation. The transformation provides additional ductility by stabilizing plastic deformation and delaying tensile necking. The excellent combination of strength and ductility make these steels suitable for wide ranging applications. The class of steels with improved properties due to austenite to martensitic transformation during deformation are commonly deemed TRIP steels.

1.2.1. TRIP phenomenon and associated phase transformations

The concept of transformation plasticity was first popularized by Zackay and Parker in 1967 [4] demonstrating radically improved tensile ductility in medium carbon warm-work-strengthened austenitic steels. Transformation plasticity with regards to martensitic transformations arises due to 1) biasing of accommodation slip triggered by transformation shape strain, 2) martensitic transformation net shape strain due to stress biasing of martensite orientation variants[7]. Transformation plasticity and detailed understanding of the transformation kinetics have been shown to be invaluable in designing metastable materials with exceptional mechanical properties ranging from fully austenitic steels to low carbon steels with dispersed austenite. The enhancement of properties due to transformation is not limited to steels as similar observations are reported in other alloy systems such as titanium, zirconium or cobalt alloys [8,9].

The martensitic transformation during deformation results in controlled strain hardening which is crucial to inhibit flow instability and delay the onset of necking. Subsequent studies [5,7] on TRIP effect showed the improvement in mechanical properties due to reverse curvature of the σ-

ε curve that postpones plastic localization such as tensile necking and shear fracture. Improvement of ductility in multi-component steels due to the TRIP effect of metastable retained austenite has been reported in multiple research efforts [7,9,10]. The interplay of transformation kinetics and plastic flow behavior in TRIP steels has been studied in depth by Olson and Azrin [11] by measuring the stress strain behavior during uniform as well as localized deformation.

The Gibbs free energy of individual phases plotted as a function of temperature in Figure 5(a) shows austenite to martensite transformation can occur spontaneously at pre-existing defects below a temperature defined as martensite start (Ms) temperature[12]. The free energy difference between austenite and martensite at Ms equals the critical free energy required for transformation. At temperature above Ms and below M_d, transformation can occur aided by a mechanical driving force (U') in addition to the chemical driving force ($\Delta G_T^{\gamma-\alpha'}$). Above M_d temperature the total driving force (chemical + mechanical) is unable to surpass the critical driving force making transformation no longer possible. At temperatures in between Ms and M_d, the deformation induced transformation behavior is divided into two different transformation modes (as shown in Figure 5(b)):

1) Stress assisted mode at low temperatures ($Ms < T < Ms^{\sigma}$) with yielding by transformation

2) Strain induced mode at higher temperatures (above $Ms^{\sigma} < T < M_d$) with yielding by slip.

Ms^{σ} is the temperature at which the material can withstand the maximum stress before yielding due to martensitic transformation or slip deformation. It is also the temperature at which the deformation induced transformation mode changes from stress assisted to strain induced.

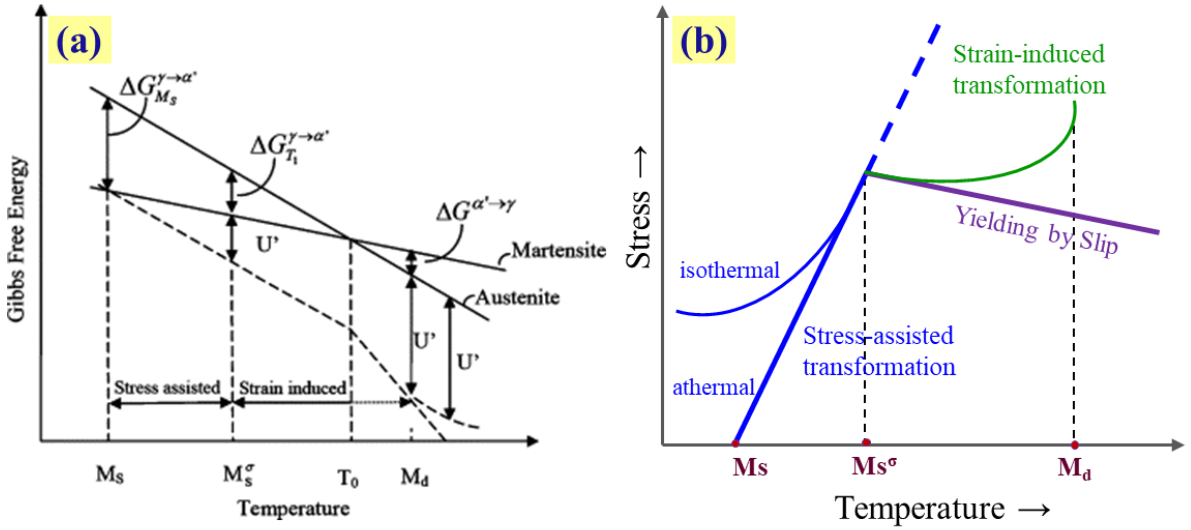

Figure 5 (a) Gibbs free energy versus temperature plot showing possible transformation scenarios [12], (b) Yield stress versus temperature plot showing the two different modes of deformation induced martensitic transformation

Stress Assisted transformation

In the stress-assisted regime of deformation induced martensitic transformation below Ms^{σ}, the applied stress assists the transformation at pre-existing nucleation sites by modifying the effective potency distribution of the sites in the austenite phase through a distribution of orientation-dependent mechanical work. The potency of a nucleation site is described in terms of thickness ***n*** (number of crystallographic planes) of the stabilized nucleus based on the dislocation dissociation model of classical heterogeneous martensite nucleation theory [13]. The critical potency for nucleation, $\boldsymbol{n_o}$ for stress assisted transformation to occur is given by

$$n_o = \frac{-2\gamma_s/d}{\Delta G_{ch} + \frac{1}{3}\Delta G_{\sigma}^{max} + W_F}$$

and the available potency of sites in annealed austenite is expressed by a defect potency distribution, $N_v = N_v^o \exp(-\alpha n)$, where γ_s is the semi-coherent nucleus specific interfacial

energy, *d* is interplanar spacing, W_F is the frictional work of interfacial motion. ΔG_{ch} & ΔG_{σ}^{maz} are the chemical and maximum mechanical driving force for transformation respectively. The $1/3^{rd}$ factor for mechanical driving force is under the assumption of a fully random orientation distribution of nucleation sites. N_v^o is the total number of nucleation sites of all potencies and α is a constant.

For dispersed austenite, the fraction of transformed particles is equal to the probability of finding at least one nucleation site in the particle of volume Vp with Nv as cumulative number density of nucleation sites. It is given by

$$f = 1 - \exp(-N_v.V_p)$$

The effect of applied stress on the onset of deformation in the original high-strength austenitic TRIP steels was initially shown in the work by Olson and Azrin [11,14], where plastic strain and fraction of martensite formed were measured as functions of applied stress and plotted against test temperature. The stress values that resulted in 0.2% strain and 1% martensite fraction formed are shown in Figure 6. The correspondence of the two plots in the temperature range ($M_s < T < M_s^{\sigma}$) showed that onset of plastic deformation is controlled by stress assisted transformation in this temperature range. In this regime, the volume fraction of transformed martensite is linearly related to the applied strain, as given by $f^{\alpha'} = k\varepsilon$ where ε is plastic strain and *k* is a constant. During the stress-assisted transformation process, the martensite formed has the same lenticular plate morphology as that formed upon cooling to low temperatures.

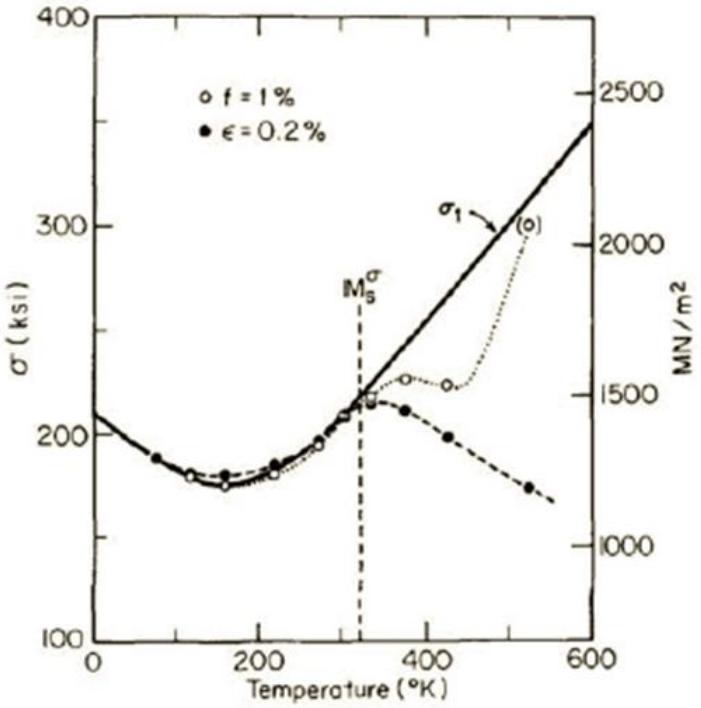

Figure 6 Experimental measurements for 0.2% yield stress and stress at which 1% martensite is detected in case of a high strength TRIP steel by Olson and Azrin [11,14]

Strain induced transformation

In the strain-induced regime of deformation induced transformations ($Ms^\sigma < T < M_d$), plastic deformation precedes martensitic transformation and results in the formation of new potent nucleation sites suitable for transformation. These new nucleation sites are located at regions of intersection of shear bands formed by plastic deformation. Based on this developed understanding of strain-induced nucleation of martensite, Olson and Cohen[15] derived a model for kinetics of strain-induced transformation. The model describes the relation between the fraction of martensite ($f^{\alpha'}$) formed with the applied plastic strain (ε) as expressed below. The developed model is seen to accurately fit experimental data obtained at different test temperatures as shown in Figure 7(a).

$$f^{\alpha'} = 1 - \exp\{-\beta[1 - \exp(-\alpha\varepsilon)]^{n}\}$$

where β is a temp. dependent term defined by the potency distribution of shear-band intersections and α is constant defining the rate of shear-band formation, in turn dependent on the temperature-dependent stacking fault energy.

The plastic flow behavior in the strain-induced regime depends on the slip behavior of parent austenite and the simultaneously occurring martensitic transformation. A constitutive model to describe this behavior in fully austenitic steels was derived by Narutani, Olson and Cohen [16,17] by combining the two competing effects of (1) a static hardening effect due to transformed martensite and (2) a dynamic softening effect due to parallel deformation by martensitic transformation. The dominance of the dynamic softening effect at low strains plus the dominance of static hardening at high strains results in the unusual upward curving stress-strain curves shown in Figure 7(b). The effect of transformation can be seen comparing the shape of the curves at different test temperatures. By measuring both softening and hardening contributions, a constitutive relationship was developed for plastic flow of a metastable austenitic steel [16].

$$\sigma = \{[1 - f^{\alpha'}]\,\sigma_{\gamma}(\varepsilon - \alpha.f^{\alpha'}) + f^{\alpha'}\sigma_{\alpha'}(\varepsilon - \alpha.f^{\alpha'})\}\,[1 - \beta(df^{\alpha'}/d\varepsilon)]$$

where σ is the calculated flow stress, f α’ is the fraction of transformed martensite, ε is the total plastic strain, σγ is the flow stress of the austenite, σα’ is the flow stress of the martensite, (df α’/dε) is the transformation rate, α and β are constants.

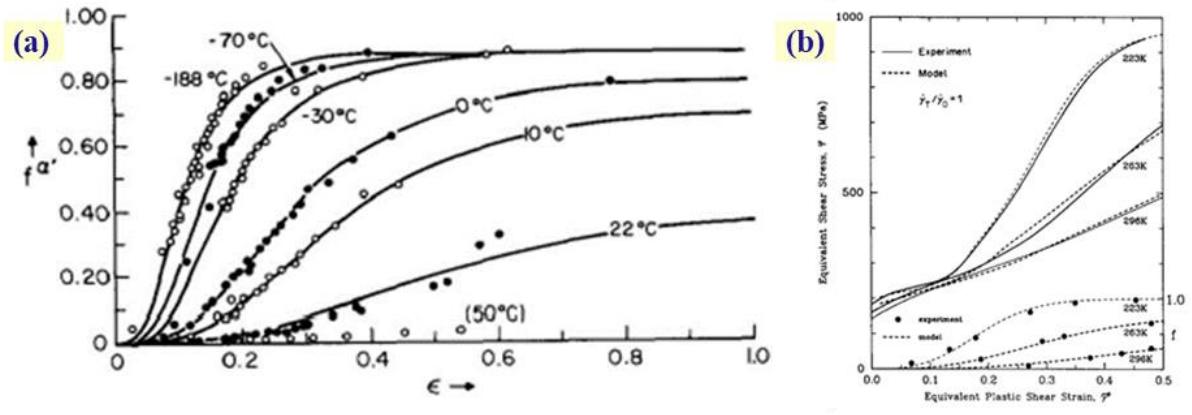

Figure 7 (a) Martensite fraction versus plastic strain for different temperatures in a 304 Stainless steel, dots represent experimental datapoints, line represent calculated curves [15],
(b) Comparison of experimental and calculated stress strain curves showing strain induced transformation effect [16,17]

1.2.2. Characteristics of multiphase TRIP steels

Multiphase TRIP steels are iron based alloys with alloyed carbon (generally 0.1% – 0.4wt%) and other common alloying additions such as manganese, silicon, aluminum, chromium, titanium, nickel, vanadium etc. Each of the added alloying elements serves a specific purpose in the overall alloy. Manganese is added to act as an austenite stabilizer while silicon and aluminum are used as inhibitors for carbide precipitation. The addition of nickel, titanium, vanadium can provide additional strength to the steel via solid solution strengthening, precipitation strengthening or other mechanisms.

The conventional multiphase TRIP steel microstructure consists of a complex mixture of intercritical ferrite, bainite, a small fraction of possible martensite phase along with 5 to 20 volume% of metastable retained austenite which gradually transforms to martensite during subsequent mechanical deformation. The austenite fraction can provide high formability of the steel during initial deformation processing while maintaining high strength values subsequent to

martensite formation. Depending on the required strength level for an application, the fraction of constituent phases can be varied to achieve desired properties. One of the essential conditions for the TRIP phenomenon to occur at room temperature is for the Ms temperature of the retained austenite to be below room temperature. Mechanical stress can result in martensitic transformation of retained austenite only if the use temperature is between the Ms and M_d temperature for the retained austenite. Changes in transformation stability of retained austenite can occur due to carbon enrichment during different stages of common heat treatment processes: 1) upon intercritical holding in the austenite + ferrite phase region and 2) during cooling to the isothermal annealing temperature and 3) upon isothermal holding at low temperature to promote bainite transformation.

Multiphase TRIP steels are generally characterized by their high strength and high strain hardening. The strength values can range from 500 to 1000 MPa while elongation can vary from 12 to 30% [18]. The curvature-reversing effect of transformation can move the stress-strain curve from a typical power law behavior for slip deformation towards an ideal exponential strain hardening behavior for flow stability ($d\sigma/d\varepsilon \geq \sigma$) as shown in Figure 8(a). This can provide exceptional energy absorption properties due to the combination of strength and ductility. At similar strength levels, fatigue properties of these steels are also generally better than other high strength steels such as HSLA steels. The amount of improvement in uniform elongation due to transformation depends sensitively on the austenite stability. The effect of change in test temperature i.e. austenite stability at the test temperature, on true stress – true strain curve was shown for the first time in fully austenitic steels with arrows indicating the point of tensile

necking, as shown in Figure 8(b) [7]. Similar effects of transformation on mechanical deformation behavior of multiphase TRIP steels has been since shown as well.

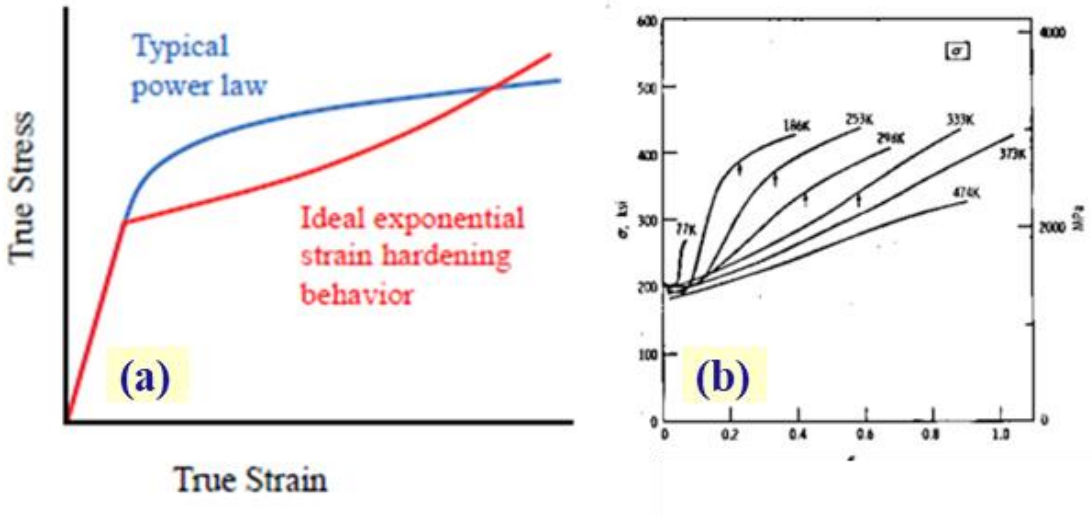

Figure 8 (a) Schematic true stress – true strain plot showing the ideal effect of strain hardening, (b) True stress-strain plots showing the effect of test temperature on stress-strain behavior of high-strength fully austenitic TRIP steels [7]

1.2.3. Austenite stability in multiphase TRIP steels

Consistent with heterogeneous nucleation theory, the mechanical stability of retained austenite in TRIP steels has been confirmed to be controlled by numerous factors:

a) Austenite composition: Austenite transformation temperatures vary predictably with composition and thus change its thermal and mechanical stability. The change in composition (especially carbon) can significantly modify the available chemical free energy for transformation and its effect on stability has been confirmed by various experimental studies [19–21]. In homogeneous systems, an increase in carbon content of remaining austenite due to progressive transformation to martensite in low alloy TRIP steel has been confirmed by

Blonde et al [20] using high energy XRD. For best performance, such studies confirm that the RA should have the optimal mechanical stability and not the maximum stability.

b) Austenite size/morphology: Consistent with nucleation potency distributions, the stability of RA has been experimentally confirmed to be higher for smaller particle sizes. Jimenez-Melero et al. show evidence that carbon content is a dominant parameter governing stability of larger austenite particles while particle volume strongly influences stability below 15μm^3 [21]. The effect of morphology is also related to size of austenite. While equiaxed particles tend to fully transform upon nucleation, film morphologies show a more gradual spread of transformation. [22,23]

c) Neighboring phases: The stability of austenite can also be influenced by the strength and load sharing characteristics of the neighboring phases[22,24]. The presence of a harder phase around austenite causes a stress shielding effect that could slow down martensitic transformation. The stability of RA inside perlitic ferrite was found to be significantly more sensitive to temperature compared to RA inside bainitic ferrite by Zhang et al. [25]. These factors can influence the pattern of accommodation slip associated with martensite growth, in turn influencing associated forest hardening effects.

Experimental measurement of austenite stability is often carried out with interrupted tensile test experiments to evaluate austenite transformation with respect to applied strain. The evolution of austenite phase fraction and its composition with strain gives insight regarding its stability. In-situ characterization experiments during tensile testing are also utilized to reveal the transformation characteristics. In-situ high energy x-ray diffraction is helpful to study the

variation of remaining austenite carbon content with applied strain[20] while in-situ EBSD analysis is helpful to quantify the role of austenite morphology and location on its stability[26].

While there have been numerous experimental studies to quantify austenite stability in recent literature, there has been limited efforts to provide predictive models for stability. Bolling and Richman originally introduced the concept of 'Ms^{σ} temperature' to quantify austenite stability against mechanical transformation. Thermodynamic modeling for the Ms^{σ} temperature was fully developed in the work of Olson and Cohen. Modeling of retained austenite stability in 4340 steel taking into account the effect of composition on thermodynamic driving force for transformation showed good agreement with experimental results [27]. These models account for all the factors influencing austenite stability and have been used to optimize the processing conditions to ensure optimal austenite stability in low alloy TRIP steels[28]. Modeling of austenite stability has also been used to improve fracture ductility of ferrite/bainite/austenite steels in the works of Brandt[29] and Gong[30]. The predictive models for Ms^{σ} temperature are used to design alloy composition and processing parameters to ensure peak fracture ductility at the material application temperature. A similar approach to predict austenite stability has been undertaken in the current research work and will be elaborated in section 2.3.4.

1.3. Nonequilibrium partitioning and coupled diffusional-displacive transformations

1.3.1 Types of restricted equilibrium states

Equilibrium phase diagrams are one of the basic tools used by metallurgists in the analysis of phase transformations in multi-component alloys. These equilibrium calculations provide much insight into the phase transformation behavior which includes the sequence of transformation and equilibrium composition of phases. However, in carbon containing iron alloys it's well known that austenite-ferrite transformations can occur by a rapid carbon diffusion controlled process followed by diffusion of slow diffusing substitutional species. Depending on the temperature-time regime of the steel heat treatment, it is possible for the alloy to be far from a full equilibrium state and thus limit the utility of full equilibrium calculations. It is in these cases that non-equilibrium constructions such as para-equilibrium are especially useful in describing the transformation behavior.

The higher mobility of interstitial elements compared to substitutional additions gives rise to two possible restricted equilibrium scenarios depending on the distribution of the elements at the interface [31,32]. Schematic isothermal sections of Fe-C-X ternary diagram illustrating the partitioning of alloying elements under the different modes are shown in Figure 9. The concentration profile of C and substitutional alloying element (X) across the austenite/ferrite interface is shown adjacent to the corresponding axis.

Non-partitioning local equilibrium (NPLE): In this case, there is no long-range partitioning of the substitutional elements (X) between the two phases and therefore it remains the same as initial composition (X_O) except right at the interface. Local enrichment occurs in the austenite phase close to the interface matching chemical potentials of the α phase. There is partitioning of carbon

across the interface which ensures carbon activity to be same everywhere. The tie line for partitioning and the concentration profiles for C and X are shown in Figure 9(b).

Para-equilibrium (PE): This is a kinetically constrained equilibrium where local equilibrium is achieved at the interface through interstitial partitioning with no partitioning of substitutional elements. In contrast to the NPLE mode, there is no local enrichment of substitutional elements at the interface. The chemical activity of the interstitial element is equal in all phases and the ratio of substitutional atoms to iron atoms remains constant for all phases. The kinetics of PE is governed by the fastest diffusing species usually C or N in the case of steels. The schematic in Figure 9(b) shows the new phase boundaries in dashed lines along with the constrained tie line, K_{PE} and the concentration profiles across the interface.

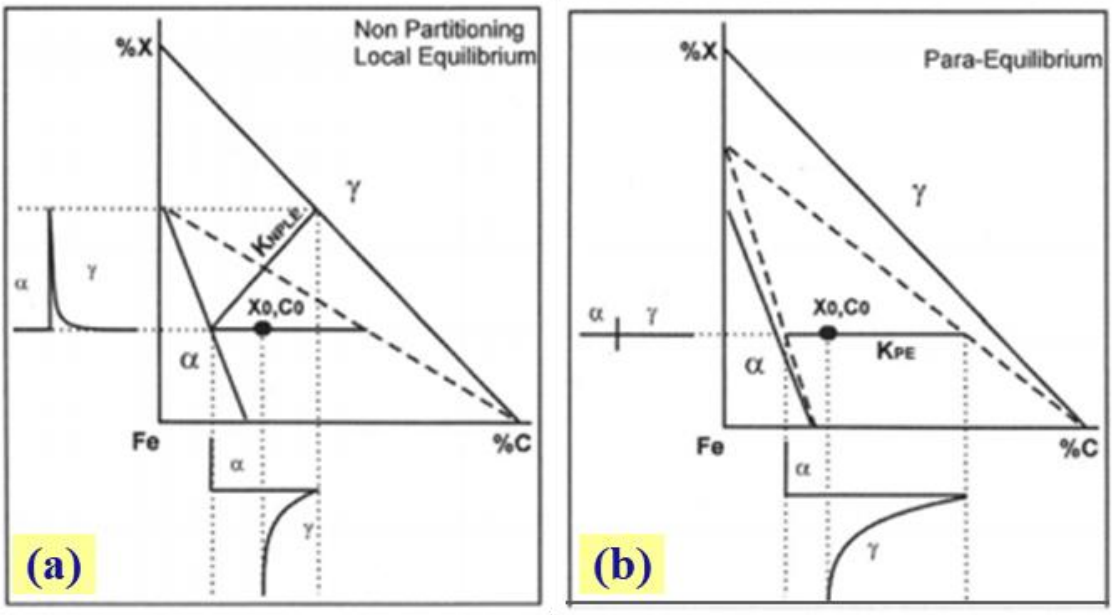

Figure 9: Schematic isothermal sections of Fe-C-X ternary diagram for the two different modes of equilibrium at the austenite/ferrite interface; (a) Non partitioning local equilibrium, (b) Para-equilibirum (Adapted from [31])

1.3.2. Coupled diffusional/displacive transformations

Solid-solid phase transformation in materials can result in non-equilibrium growth of a product phase with or without any associated composition change. Martensitic transformation is an example of non-equilibrium growth of a phase without any composition change. On the other hand, restricted equilibrium conditions such as para-equilibrium result in interstitial diffusion that results in equilibration of their chemical potential while substitutional additions are frozen in place. A more general case of non-equilibrium growth with compositional change would be the case where there is partial supersaturation of interstitials in the product phase and growth is mediated by the process of structural change across the interface. Olson, Bhadeshia & Cohen [33,34] modeled the non-equilibrium growth of ferrite plates from austenite in Fe-C alloys where the structural transformation is displacive and derived how partitioning of solute would modify the nucleation and growth behavior during bainite transformation as a coupled process. The partitioning of carbon increases the available free energy for transformation thus allowing for assisted displacive transformation above the Ms temperature. This defined the so called 'coupled diffusional/displacive' transformation. The coupled model can be used to predict the growth rate and carbon supersaturation of the product phase at any given transformation temperature.

The model derived the result by simultaneous solution of three interface response functions [35];

1) the intrinsic velocity of a glissile interface, $V_i = V_o \exp\{-Q^*/kT\}$

where $V_o=30ms^{-1}$ and Q^* is free energy of activation and can be expressed as a function of the net interfacial driving force.

$$Q(\Delta G,T) = Q_o(T) [1 - (\Delta g_n/ \Delta g')^p]^q$$

where Q(Δg, T) is the activation energy of the obstacle at a volume driving force - Δg, Q_0(T) is the activation energy in the absence of a driving force, -Δg_n is the net volume driving force, -Δg' is the net "threshold" volume driving force where Q(Δg, T) = 0. *p = 0.5 and q = 1.5*

$$\text{and } \Delta g_n = \Delta g_{ch} + (g_{el} + w_\mu + 2\gamma/nd) \text{ ; where } w_\mu = W_F^D + W_F^{SS}$$

g_{el} is the elastic free energy, w_μ is the athermal friction work done for interface motion against forest dislocations (W_F^D) and solution hardening (W_F^{SS}), γ is the interfacial energy.

2) interstitial diffusional field velocity obtained by solving:

$$\frac{x'-x_1}{x_\alpha - x_1} = (\pi p)^{0.5} \exp\{p\} \operatorname{erfc}\{p^{0.5}\} \text{ ; } p = V_d\rho/2D$$

where x'-steel composition, x_α- ferrite composition, x_1- carbon conc. in austenite at interface, *p* is peclet number given by ($p = V_d\rho/2D$); where ρ- effective plate tip radius, D-diffusion coefficient, V_d -velocity.

3) velocity consistent with solute trapping, $V_k = \frac{D\{x_1\}}{\lambda} \left(\frac{k_p - k_e}{1 - k_p} \right)$;

where $D\{x_1\}$ is the carbon diffusivity in austenite of composition x_1, λ is intersite distance of ~0.25nm, k_p - partitioning coefficient, k_e – equilibrium partitioning coefficient.

The model predicts an increasing nucleation and growth rate and supersaturation for lower transformation temperatures. The C-curve kinetics of transformation is associated with maxima of the nucleation velocity. The coupled diffusional/displacive model has been shown to accurately predict the martensite start temperature in Fe-C alloys and other alloyed steels by Mujahid et al. [36,37]. They also found good predictions for the bainite start (Bs) temperature with a stored energy term added to ferrite phase that varies with temperature.

The addition of stored energy to ferrite phase during para-equilibrium calculations was shown to accurately predict the austenite carbon enrichment during bainitic transformation in the thesis work of Mitchell Brandt [29]. Subsequently, in the thesis work of Jiadong Gong[30], the stored energy was confirmed to be a function of temperature and was modeled to predict the austenite carbon content in low carbon TRIP steels at different annealing temperatures. The predicted carbon content was used to optimize the austenite stability to maximize the benefits from transformation induced plasticity. The effect of stored energy addition to BCC phase on the para-equilibrium austenite carbon content is represented with help of schematic diagram shown in Figure 10. Stored energy addition lowers the predicted austenite carbon enrichment thus matching closely with experimental measurements. The physical understanding of stored energy has been further investigated in the current work and is discussed in section 2.3.3.

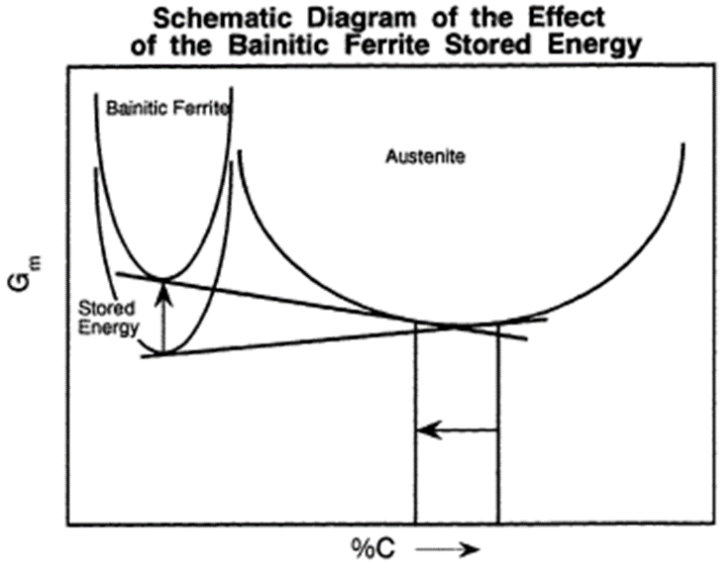

Figure 10: Schematic illustration of the effect of addition of stored energy to bainitic ferrite on the PE austenite carbon content determined by common tangent method [29]

1.4. Quench and Partitioning (Q&P)

The Quench and Partitioning concept is a novel processing route developed to produce steels with stabilized retained austenite surrounded by a martensite matrix. It was originally proposed by Speer and coworkers at CSM [38–40] and has been an area of active research ever since. The Q&P concept is based on carbon diffusion from the martensite to austenite phase during isothermal annealing. A schematic of the heat treatment cycle is shown in Figure 11. The different stages of the heat cycle are as follows:

1. The Q&P cycle begins with a full austenitization step where the material is held above the Ac3 temperature for a certain limited time to ensure complete transformation.
2. The steel is then quenched to a temperature between the martensite start (Ms) and finish (Mf) temperatures called the quench temperature (QT). This step usually results in a desired martensite fraction, usually 70-80% in the microstructure with remaining metastable retained austenite.
3. The material is then reheated and isothermally held at a higher temperature, called the partition temperature (PT) for a defined partition time. This step helps in stabilizing the retained austenite by enabling carbon diffusion to austenite phase from the martensite matrix.
4. The increased carbon content of austenite helps it withstand the final quenching step to room temperature.

The ideal Q&P microstructure after the above-described cycle contains stabilized austenite phase in a martensite matrix. This however is not actually achieved as other competing phase transformations also occur during the process cycle. The final microstructure thereby consists of

retained austenite in a martensitic matrix with other phases such as bainite and carbides. Efforts are made to limit other competing transformations by appropriate alloying additions and careful selection of heat treatment parameters.

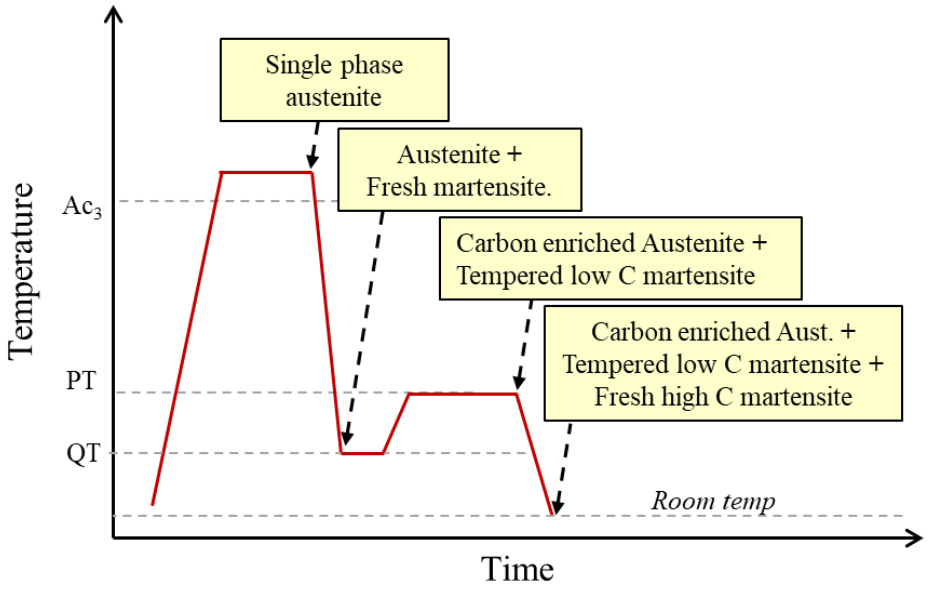

Figure 11: Schematic of Q&P heat cycle with description of the microstructure at different stages of heat treatment

1.4.1. Role of alloy composition and initial microstructure

Low alloy TRIP steel compositions are generally used in the Q&P concept. In addition to carbon, the other major alloying additions are manganese and silicon. Small additions of chromium, molybdenum, nickel, titanium and others are also added for specific property improvements. The individual amount of alloying additions of C, Mn and Si frequently lie in the ranges of 0.1-0.5 wt%, 0.2-2.5wt%, 0.4-1.8wt% respectively [41]. The effect of individual alloying element on the TRIP microstructure and mechanical properties has been reported over the years in published

experimental studies: i.e. carbon[42,43], manganese[42,44], silicon[45], aluminum, chromium and molybdenum[46].

Carbon increases the strength of martensite and helps in stabilizing retained austenite. The strength of martensite is also affected by its dislocation density. Morito et. al. [47] reported an increase in the dislocation density of as-quenched martensite with alloy carbon content up to 0.6wt%. De Moor et. al. [42] showed that in the fully austenitized condition, increasing alloy carbon from 0.2 to 0.3 wt% increased the tensile strength as well as total elongation. The results from this work are summarized in Figure 12(a). Similar observations were made by Kahkonen et. al. [43] in their work comparing mechanical properties of alloys with 0.3 and 0.4wt% carbon. The higher carbon content resulted in higher strength values and improved ductility associated with higher fraction of retained austenite.

Manganese is one of the most common alloying addition in steels next to carbon. It is known to improve hardenability of steel, strengthen the steel via solid solution strengthening and potentially act as an austenite stabilizer. A wide range of manganese levels in steels processed under various Q&P cycles have been examined in experimental studies [42,48–51]. It is often difficult to empirically isolate the effect of one single parameter on the properties when there are multiple parameters affecting the final properties.

The addition of silicon and aluminum has been known to retard cementite precipitation in steels, due to negligible solubility of silicon in cementite. For precipitation to occur, silicon needs to diffuse to the matrix. For higher silicon content in the alloy, the rate of precipitation is limited by the rate of diffusion of silicon which is quite low compared to carbon. Some of the recent studies[52–54] on the silicon effect on cementite precipitation demonstrate that it plays a

significant role in pacing carbide growth. The studies also indicate the possible precipitation of other metastable carbides and carbon segregation during early stages of tempering. The role of silicon in carbon partitioning in martensite/austenite structures was studied in a 1C-1Mn (wt%) steel by Kim et. al. [53]. Si was confirmed to stabilize the austenite phase during partitioning stage and retard the austenite decomposition process. Empirical studies by De Moor et. al.[46] explored the addition of aluminum as a partial replacement for silicon and examined the effect of molybdenum addition. The results indicated a decrease in the final retained austenite fraction upon partial replacement of silicon by aluminum. The addition of Mo to the CMnSi alloy appeared to improve the retained austenite fraction. The tensile mechanical properties for the different steels under different partitioning conditions are summarized in Figure 12. Amongst the different alloys examined, the CMnSi and MoCMnSi steels gave the best combinations of mechanical properties.

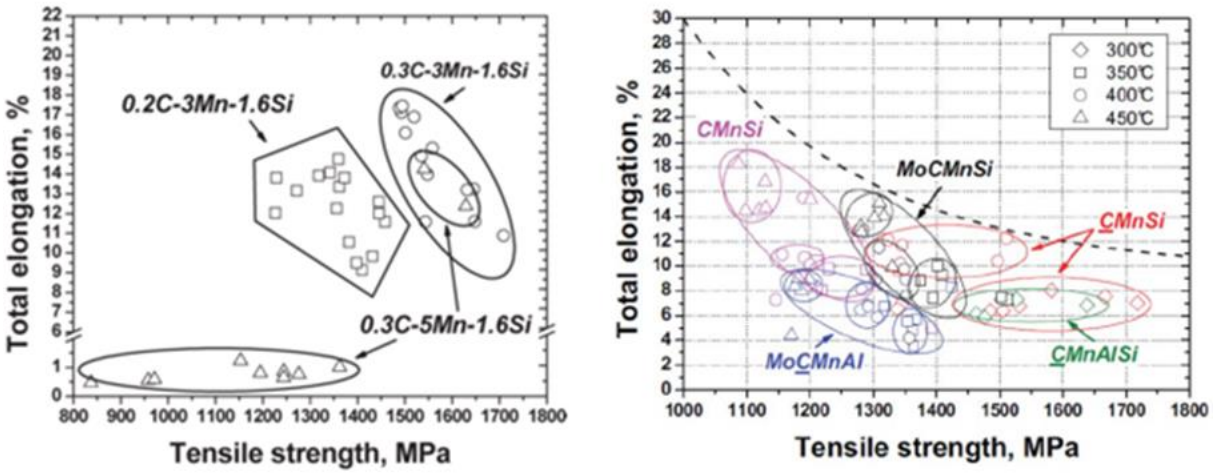

Figure 12: Total elongation versus tensile strength (a) for alloys with different C and Mn levels [42], (b) for alloys with Mo, Al additions [46]

1.4.2. Role of processing parameters: FA vs IA, QT, PT and P-time

The final performance of a Q&P alloy depends on the microstructural features developed during the different stages of the heat treatment cycle. The key processing parameters that influence the final microstructure include the initial microstructure, austenitizing temperature, cooling rate, quench temperature (QT), reheating rate from QT to PT, partition temperature (PT) and partition time. The effect of each of these parameters has been studied experimentally by various researchers over the years. A selected few of those efforts are summarized below.

Prior Q&P microstructure: The effect of initial microstructure has been studied by Zhang et. al. in an inter-critically annealed low carbon Nb-microalloyed Si-Mn steel with composition 0.18C-1.44Mn-1.48Si-0.15Al-0.025Nb [55]. They compared material processed by conventional Q-P processing and material that underwent prior quenching to Q&P processing designated as Q&Q-P. The authors confirmed that the double austenitizing Q&Q-P treatment helped refine the prior austenite grain size promoting a higher fraction of film type retained austenite vs blocky austenite compared to conventional Q-P processing. Santofimia et. al. [56] studied the effect of initial microstructure before Q&P treatment on the final microstructure and mechanical properties of a 0.2C-3.5Mn-1.5Si alloy. The starting martensite-ferrite microstructure of the alloy was QP processed after partial austenitization to produce martensite with film-like ferrite and significant amount of retained austenite. The resulting microstructure was shown to have excellent combination of mechanical properties[57].

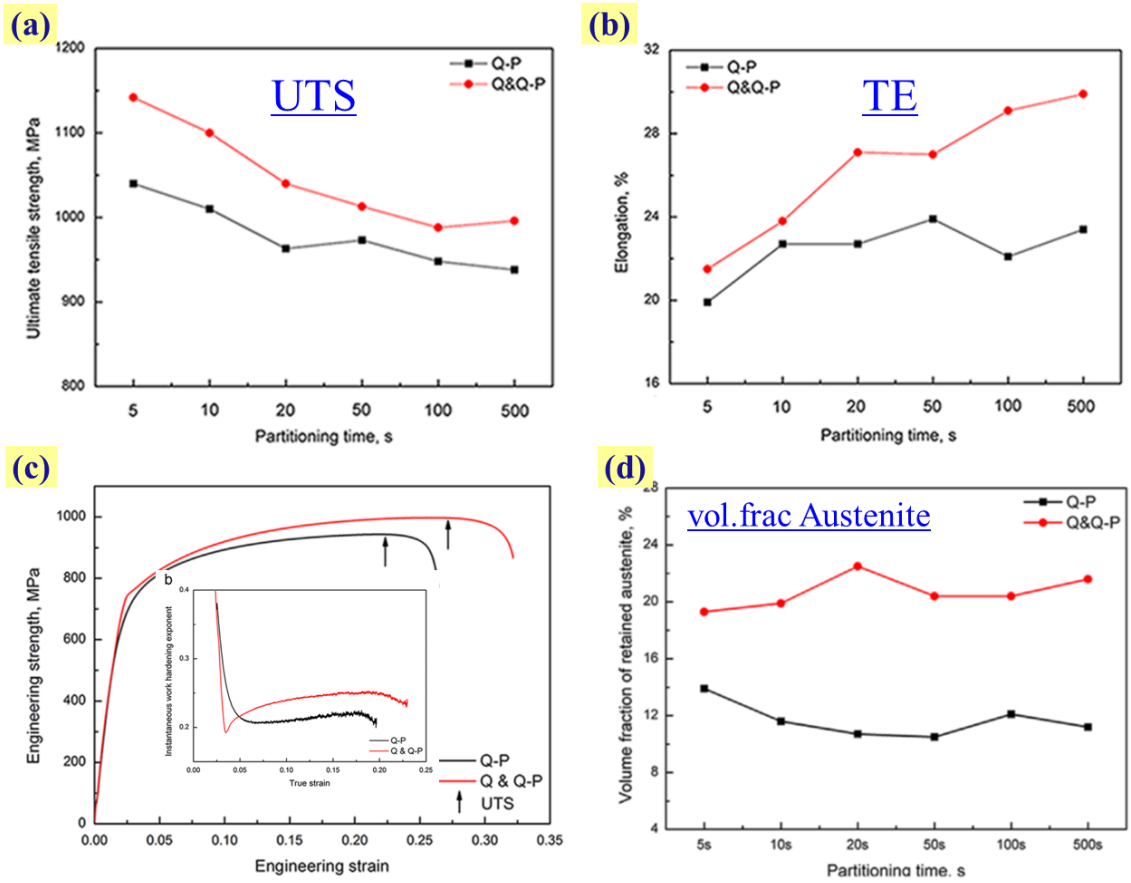

Figure 13: Mechanical properties (a) UTS, (b) TE, (c) Stress-strain curves and (d) austenite volume fraction in the steel processed by Q&Q-P processing in work of Zhang et al [55].

Full vs Intercritical austenitization (FA vs IA): A comparative study of the effect of full versus partial austenitization (F-QP vs I-QP) on a 0.2C-1.55Mn-1.58Si alloy was performed by Yan et. al.[58]. The work concluded that F-QP resulted in relatively lower fraction of retained austenite compared to I-QP; however blocky austenite constituted a major fraction of the austenite in the case of I-QP. The I-QP samples showed higher ranges for product of strength and elongation (PSE) but lower strength values as expected for a ferrite containing microstructure. The work by Wan-song et al. [59] examined the microstructural evolution and mechanical

properties of a 0.176C-1.58Mn-1.3Si-0.26Al-0.3Cr subjected to three different levels of partial austenitization and full austenitization with QT_240/15s and PT_420 for different times. They reported a higher fraction of retained austenite after partial austenitization compared to full austenitization. This results in an approximately 15-20% higher elongation but at the cost of lowering strength by about 200 MPa. In her doctoral thesis, Amy Clarke reported the effect of IA vs FA for different combinations of Q&P parameters [60]. The IA samples, as shown for the case of QT240_PT400 in Figure 14, have a higher volume fraction of retained austenite along with higher overall austenite carbon content.

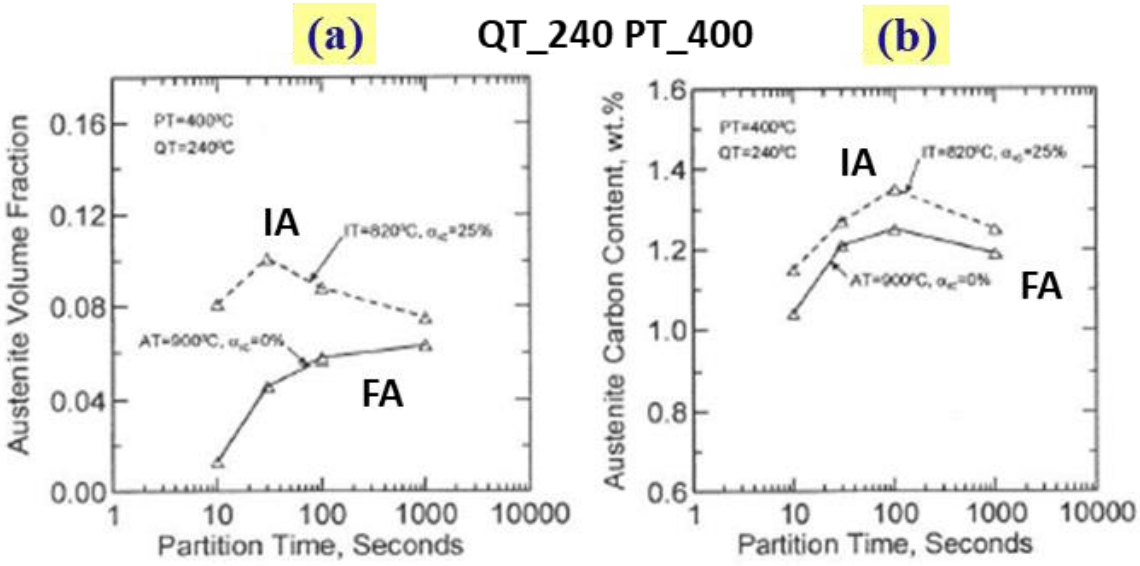

Figure 14: Comparison of IA vs FA reported in the doctoral thesis of Amy Clarke [60]

Quench temperature (QT): QT is one of the key parameters that determines the final microstructure after Q&P processing. The selection of QT determines the tempered martensite phase fraction in the alloy and thus affects the strength level directly. The amount of martensite is also key to ensure sufficient carbon is available to partition and stabilize the remaining

austenite. Lesser quenched martensite (QT close to Ms temperature) increases the possibility of bainite transformation during partitioning and also formation of fresh martensite during final quenching. On the other hand, too much quenched martensite (QT far below Ms temperature) results in less than optimal amount of austenite with potentially excessive carbon stabilization. An optimal quench temperature is desirable to achieve a maximum amount of retained austenite with the optimal stability or carbon content. The effect of quench temperature on retained austenite fraction and carbon partitioning has been measured by various researchers in the last decade. These include low carbon alloys with low to medium manganese content and other alloying additions such as Cr, Mo and Al. The alloy composition and processing conditions for some of these studies are listed in Table 1 and discussed below.

Koopmans in his thesis work studied the effect of varying QT on the retained austenite fraction and its carbon content [61]. The 0.2C alloy was fully austenitized and quenched to different QT followed by partitioning at 400^{o}C for 50 seconds. The results plotted in Figure 15(a) show retained austenite fraction increasing with QT to its maximum at around 260^{o}C. The austenite carbon content decreased with decreasing QT to around 240^{o}C after which it increased for further decrease in QT. The high Mn content of the alloy along with the short partition time of 50s at 400^{o}C led to fresh martensite formation during final quenching. Thus, the austenite fraction sharply decreased for higher quench temperatures. The increase in austenite carbon content with decreasing quench temperature was attributed to the increasing martensite fraction which would mean a higher amount of carbon available for partitioning. Sun et al. [62] studied an intercritically annealed low carbon alloy that was QP processed with different QT and partitioned at 350^{o}C for 100seconds. The maximum austenite fraction measured was around 10%

for QT of 140^{o}C. The measured austenite carbon content was measured to be higher for the lowest QTs shown in Figure 15(b). Research work by Seo et al. [49] showed similar variation of austenite fraction, in Figure 15(c), with QT for their medium Mn steel with added Cr. The higher manganese content and chromium additions result in higher fraction (more than 30%) of retained austenite. The austenite carbon content is however much lower which could also be a result of the high partition temperature of 450^{o}C. Austenite carbon content is seen to be increase in the case of lower QT. The same authors reported increasing amount of retained austenite with increase in QT for a lower Mn steel as shown in Figure 16(a). No sharp decrease in austenite fraction was observed for higher QT conditions. This would perhaps be due to lower manganese content resulting in faster diffusion and/or due to lower PT that produces a more stable austenite. Lower fraction of austenite with higher carbon content was shown for the alloy when partitioned at 400^{o}C for 180secs. Similar results were reported in work of other researchers [63–66] shown in Figure 16(b-e). A peak in austenite fraction is observed in all steels with high manganese content (>2.5%) or in the case of intercritically annealed low manganese alloys. This is likely due to lower carbon diffusivity in high manganese containing austenite phase that results in fresh martensite formation from the inhomogeneous austenite upon final quenching. Insufficient time at the partition temperature would also result in an inhomogeneous carbon distribution promoting fresh martensite formation. The work of Huyghe et al. [64] on a fully austenitized 0.2C 2.3Mn 1.4Si 0.2Cr alloy showed the variation in austenite fraction with QT and P-time as shown in Figure 16(d). Peak austenite fraction is achieved at longer P-time for higher QTs. The effect of varying stability and austenite fraction can be seen on the true stress-true strain plots shown in Figure 17. For lower QT of 280^{o}C maximum ductility is achieved after 120s of partitioning

compared to after 1000s of partitioning for QT of 320^{o}C and 360^{o}C. The overall strength level of the steel can be seen to decrease with increasing QT due to lesser fraction of tempered martensite in the microstructure. The role of QT was also reported in the work of De Moor et al. [42] which also compared the effect of different alloy carbon content. The reported austenite fraction, carbon content and mechanical properties are listed in Table 2. The austenite carbon content seems to initially decrease with QT before increasing for the lowest temperatures corresponding to different direction of interface motion during partitioning treatment. Higher yield strength values were reported for lower QT while the ultimate tensile strength remained approximately at the same level for each of the alloys. Higher alloy carbon content resulted in higher ductility despite having lesser austenite fraction with similar austenite carbon content. The optimal carbon content for maximum ductility seems to be at a lower value around ~0.98 wt% for the 0.2C alloy compared to ~1.1wt% for the 0.3C alloy. Analysis of Q&P samples with varying quench temperature was undertaken in the thesis research of J. Kahkonen [67] in 2016 and Maria Calderon [68] in 2015. The results from their work on alloy compositions listed in Table 3 are summarized in Table 4 and Table 5. In most examples, the measured austenite carbon content in both studies is lower for low QT samples compared to higher QT. This is different from the observations made earlier and could be due to the tested QTs not being low enough to show a reversal of the direction of interfacial motion at PT.

Table 1: Literature studies on effect of QT on Q&P microstructure

Koopmans et al. 2015	0.2C 3.5Mn 1.5Si 0.5Mo 0.03Al	FA, PT400C/50s	[61]
Sun et al. 2013	0.2C 1.9Mn 1.5Si	**IA**, PT350C/100s	[62]
Seo et al. 2016	0.2C 4.0Mn 1.6Si 1Cr	FA, PT450C/300s	[49]
Seo et al. 2014	0.28C 1.5Mn 1.6Si 1Cr 0.02Ti	FA, PT400C/180s	[69]
HajyAkbary et al. 2016	0.3C 3.5Mn 1.6Si	FA, PT400C	[63]
Santofimia et al. 2011	0.2C 2.5Mn 1.5Si 1.5Ni 1Cr	FA, PT400C/100s	[65]
Clarke et al. 2008	0.19C 1.59Mn 1.63Si 0.036Al	**IA**, PT400C	[66]
Huyghe wt al. 2017	0.2C 2.3Mn 1.4Si 0.2Cr	FA, PT400C	[64]
De Moor et al. 2011	0.2C 3Mn 1.6Si	FA, PT400C/100s	[42]
	0.3C 3Mn 1.6Si	FA, PT400C/100s	[42]

Table 2: Mechanical properties and austenite characteristics for Q&P cycles with varying quench temperature (selected data from work of De Moor et al. [42])

	QT (°C)	PT (°C)	Pt (s)	YS (MPa)	UTS (MPa)	UE (pct)	TE (pct)	RA (vol pct)	C_{aust} (wt%)
0.3C 3Mn 1.6Si	180	400	100	1055	1492	15	17	6.2	1.10
	200	400	100	1119	1495	15	17	2.8	1.11
	220	400	100	967	1489	15	17	1.0	0.97
	250	400	100	937	1543	10	12	14.6	1.05
0.2C 3Mn 1.6Si	190	400	100	1234	1371	6	12	7.2	1.12
	210	400	100	1182	1362	8	13	6.8	1.05
	230	400	100	1095	1318	10	14	8.4	0.98
	250	400	100	960	1228	10	14	6.1	1.03

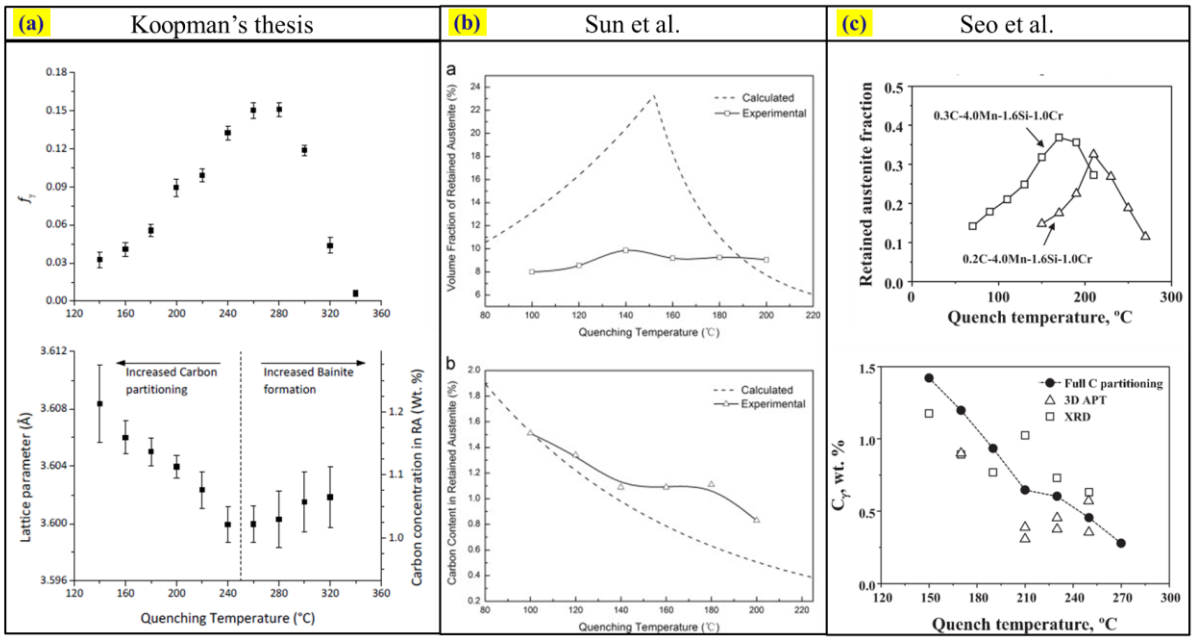

Figure 15 Experimental measurements for retained austenite fraction and carbon content from different research efforts by (a) Koopmans et al. [61] (b) Sun et al. [62] (c) Seo et al. [49]

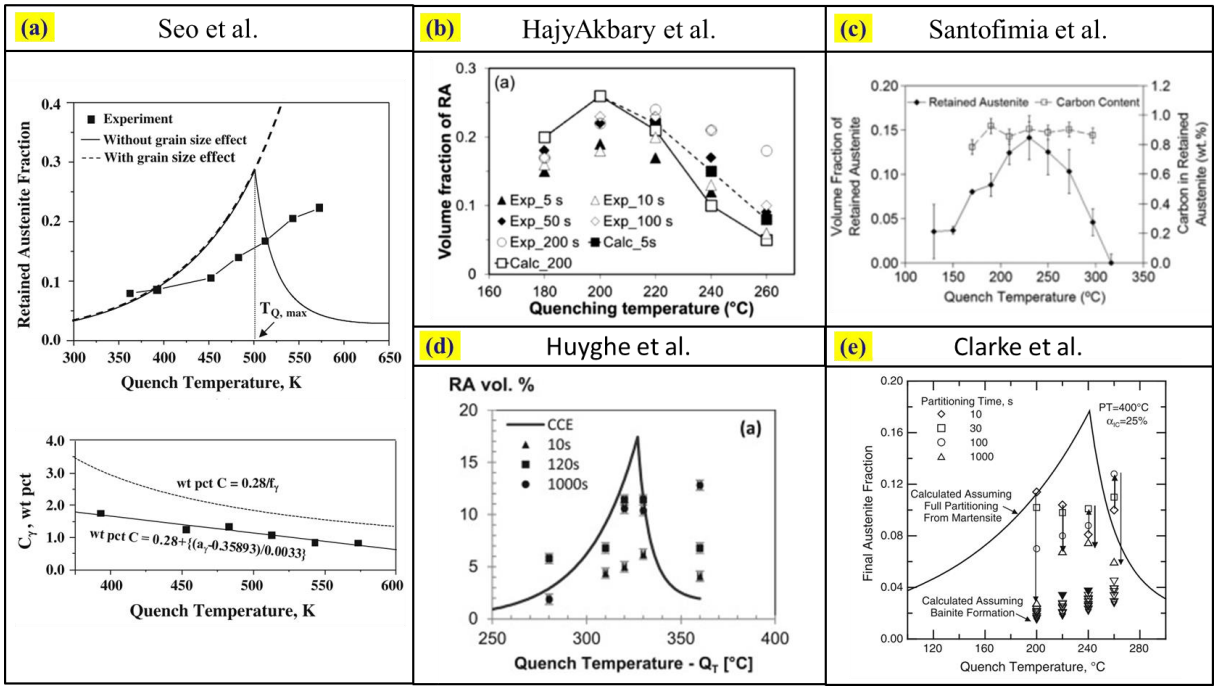

Figure 16 Experimental measurements for ret. austenite frac. and carbon content from work of (a) Seo et al. [69] (b) HajyAkbary et al. [63] (c) Santofimia et al. [65] (d) Huyghe et al. [64] (e) Clarke et al. [66]

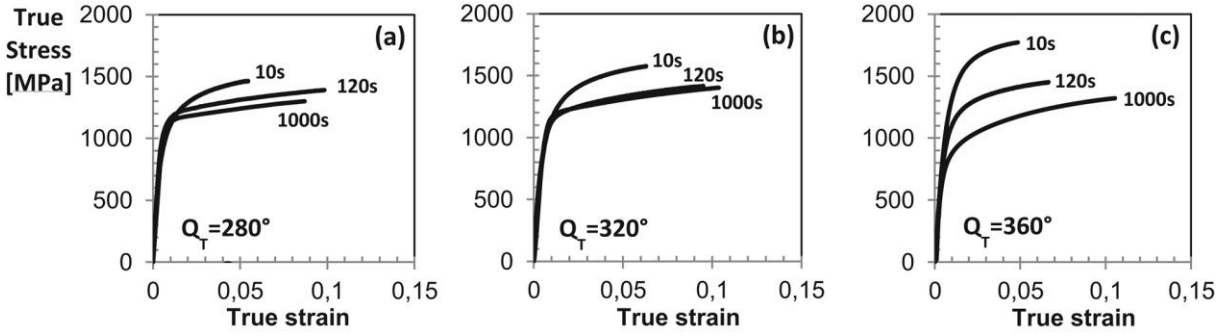

Figure 17:True stress-strain plots for Q&P processed samples with different QT (adapted from Huyghe et al. [64])

Partition temperature (PT):

While the quench temperature can have significant impact on the retained austenite fraction, partition temperature is by far the most crucial factor controlling final austenite carbon content and thus its stability. The PT in combination with partition time also affects competing carbide precipitation which impacts the retained austenite fraction by mass balance. In recent literature, while the role of QT on Q&P microstructure has been extensively investigated, the influence of PT has comparatively received surprisingly limited attention. Some of these works are tabulated with their alloy composition and processing parameters in Table 3.

The effect of partitioning temperature on the microstructure of a low carbon alloy was reported in the doctoral thesis of Amy Clarke [60]. The measured variation of austenite fraction and carbon content are shown in Figure 18(a). The austenite fraction is seen to reach its maximum much faster at higher partition temperature (450^{o}C compared to 400^{o}C). Decrease in the austenite fraction at longer partition times was suggested to be due to carbide precipitation. Consistent with expectation from thermodynamic Paraequilibrium, the austenite carbon content was reported to be maximum for lowest partition temperature at the longest partition time. Zhou et al. [70] studied the effect of different PT on the austenite characteristics and mechanical properties on a low carbon alloy with nickel addition. The measured variation of austenite phase fraction and carbon content are plotted in Figure 18(b). For the short partition time of 30sec, the austenite carbon content is seen to increase upon decreasing PT initially after which it decreases with further decrease in PT consistent with kinetic limitation. The austenite fraction showed similar trends as well. The short partition time of 30s would be insufficient time for complete partitioning for lower temperatures and is clearly the reason for lower austenite fraction and

austenite carbon content for lower partition temperatures. Santofimia et al. reported higher amount of retained austenite for lower partition temperatures as shown in Figure 18(c). The austenite carbon content was also reported to be the highest for the lowest PT of 350^{o}C. In the thesis research work of J. Kahkonen [67], the austenite fraction and carbon content was measured as a function of PT for different QT conditions. The austenite carbon content in Table 4 can be seen to be higher at a PT of 400^{o}C compared to 450^{o}C in almost all cases. This was not the case for the lowest PT of 350^{o}C possibly due to increased carbide precipitation at this temperature, reducing the austenite carbon content. The austenite phase fraction remained similar for different PTs while showing an increase with increase in alloy carbon or manganese content. The research work of Maria Calderon performed similar measurements in a 0.25C-3Mn-1.5Si alloy as shown in Table 5. Lower partition temperature can be seen to result in higher partitioning but these observations are likely influenced by overriding effects of carbide precipitation.

Table 3: Literature studies on role of PT on Q&P processing

Amy Clarke [60]	0.19C 1.59Mn 1.63Si 0.036Al	FA, QT220/240,	PT350/400/450	Pt 10-1000s
Zhou et al. [70]	0.26C 1.48Mn 1.2Si 1.5Ni 0.05Nb	FA, QT290	PT350-450	Pt 30s
Santofimia 2011 [65]	0.2C 2.5Mn 1.5Si 1.47Ni 1.01Cr	FA, QT275	PT350,400,450	Pt10-2000s
Kahkonen 2016 [67]	0.3C 1.5Mn 1.5Si	FA, QT215,242,265	PT350,400,450	Pt 10-300s
	0.4C 1.5Mn 1.5Si	FA, QT200,225,250	PT350,400,450	Pt 10-300s
	0.3C 3Mn 1.5Si 0.25Mo	FA, QT150,175,200	PT350,400,450	Pt 10-300s
Maria 2015 [68]	0.25C 3Mn 1.5Si 0.023Al 0.015Cr	FA, QT224,244,264	PT300,350,400	Pt100-1000s

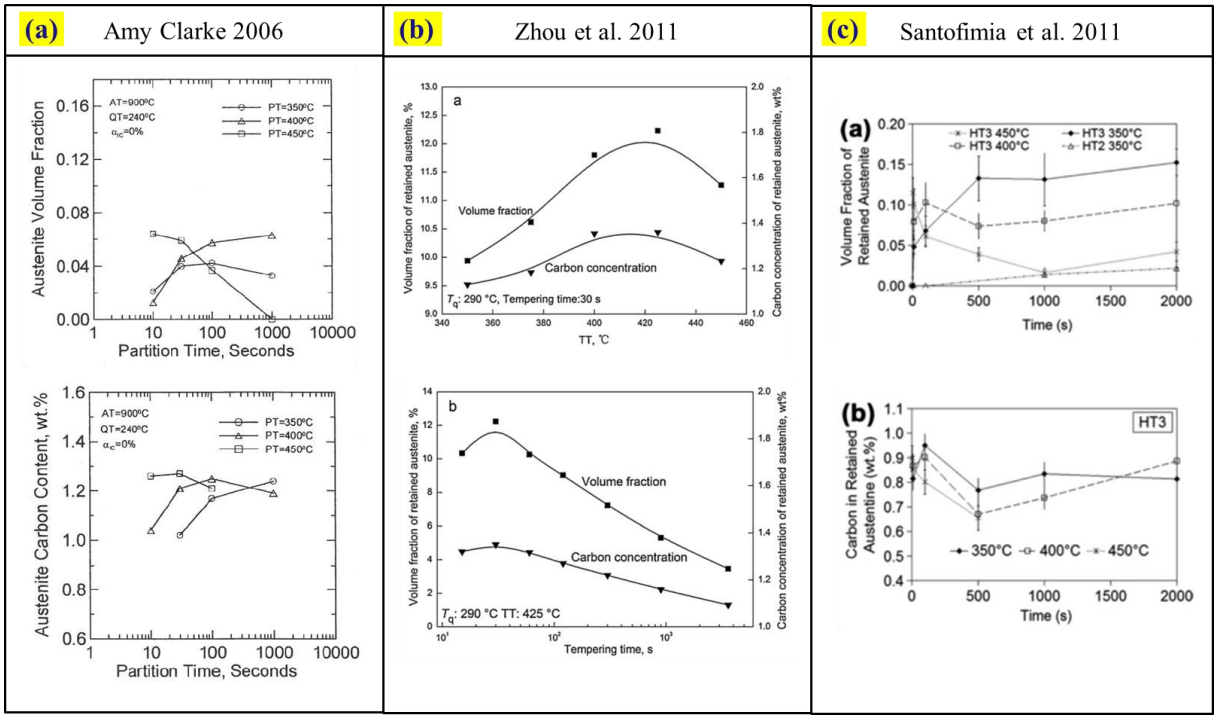

Figure 18: Austenite phase fraction and carbon content variation with PT reported in the work of (a)Amy clarke, (b) Zhou et al. [70], (c) Santofimia et al. [65]

Table 4: Selected data from masters work of Kahkonen at CSM 2016 [67]

	QT (°C)	PT (°C)	Pt (s)	RA (vol pct)	C in Aust
0.3C 1.5Mn 1.5Si	215	400	60	10.5	0.92
	242	400	60	8.4	1.20
	265	400	60	11.6	1.14
	242	350	300	10.1	1.13
	242	400	60	8.4	1.20
	242	450	30	10.2	1.13
0.4C 1.5Mn 1.5Si	200	400	60	11.6	1.29
	225	400	60	17.4	1.28
	250	400	60	17.4	1.33
	225	350	300	13.3	1.11
	225	400	60	17.4	1.28
	225	450	30	17.9	1.29
0.3C 3Mn 1.5Si + 0.25Mo	150	400	60	12.2	0.59
	175	400	60	18.8	0.88
	200	400	60	17.4	0.74
	175	350	300	16.7	0.74
	175	400	60	18.8	0.88
	175	450	30	19.9	0.67

Table 5: Selected data from doctoral thesis of Maria Calderon UCM 2015 [68]

0.25C 3Mn 1.5Si	224	350	500	14.2	0.91
	244	350	500	14.4	0.99
	264	350	500	13.5	1.11
	244	300	500	14.7	1.05
	244	350	500	14.4	0.99
	244	400	100	18.3	0.84
	244	400	500	17.9	1.03
	244	400	1000	20.2	1.01

Partition time:

Partition time (P-time) plays a vital role in determining the final phase fraction in the Q&P microstructure. Isothermal hold at the PT for a certain P-time results in tempering of the martensite formed during initial quenching that leads to softening of the alloy. Bainite transformation and carbide precipitation during the P-time impacts the final austenite fraction and its carbon content. The variation in these quantities with partition time is expected to vary with alloy composition, quench and partition temperature. In an inter-critically annealed alloy (0.19C-1.59Mn-1.63Si), the variation of austenite fraction and carbon content was studied as a function of partition time for varying QT and PT by Clarke et al. [66] as shown in Figure 16(e) and Figure 18(a). The partition time required to reach maximum austenite carbon content increases with austenite thickness associated with an increase in QT for PT of 400^{o}C. The maxima in austenite fraction with partition time was seen to be dependent on the starting martensite fraction (or quench temperature). Significant decrease in austenite fraction at higher partition times for all QT cases was attributed to carbide precipitation. The work by Clarke on a fully austenitized 0.19C-1.59Mn-1.63Si-0.036Al alloy showed the role of partition time on austenite fraction and carbon content at different PTs using a fixed QT. The results shown in Figure 18(a) suggest a peak value for carbon content and austenite fraction with partition time. The peak time is shorter at higher partition temperatures.

Sun et al. [71] studied the effect of partition time on an inter-critically annealed 0.2C-1.9Mn-1.5Si alloy quenched to 160^{o}C for 5secs and partitioned at 400^{o}C for 10-1000secs. The reported variation in austenite fraction, carbon content and overall mechanical properties are shown in Figure 19. The austenite fraction is seen to come down initially and then remain quite stable for

long partition times. The austenite carbon content meanwhile increases and saturates around 1000s of partition time. The long P-time for reaching peak austenite carbon content could possibly be due to inter-critical annealing that results in larger austenite blocks with higher diffusion distance. The variation in UTS was attributed to the tempering (or softening) of martensite. The yield stress variation at early partition times was suggested to be due to bainite transformation at the partitioning temperature which stops after a few seconds. The increase in sample length during partitioning shown in Figure 19(d) supports bainite transformation. The elongation values were confirmed to mostly depend on the stability and amount of retained austenite. Zhou et al. [70] showed mostly a continuous decrease in austenite volume fraction and carbon content with partition time for a FA 0.26C-1.48Mn-1.2Si-1.5Ni-0.05Nb alloy partitioned at 425^{o}C. The variation in austenite fraction and carbon content along with mechanical properties is shown in Figure 20. Longer partition times led to reduction in austenite fraction, austenite carbon content and UTS of the alloy attributed to increasing carbide precipitation. The effect of partition time at different QT and fixed PT has been shown in the work of Huyghe et al. [64]. Figure 16(a) confirms longer partition time are required to achieve maximum austenite fraction for the same PT and coarser austenite associated with higher QT. Longer partition time is also required to finish carbon partitioning that results in the best mechanical properties as shown in Figure 17.

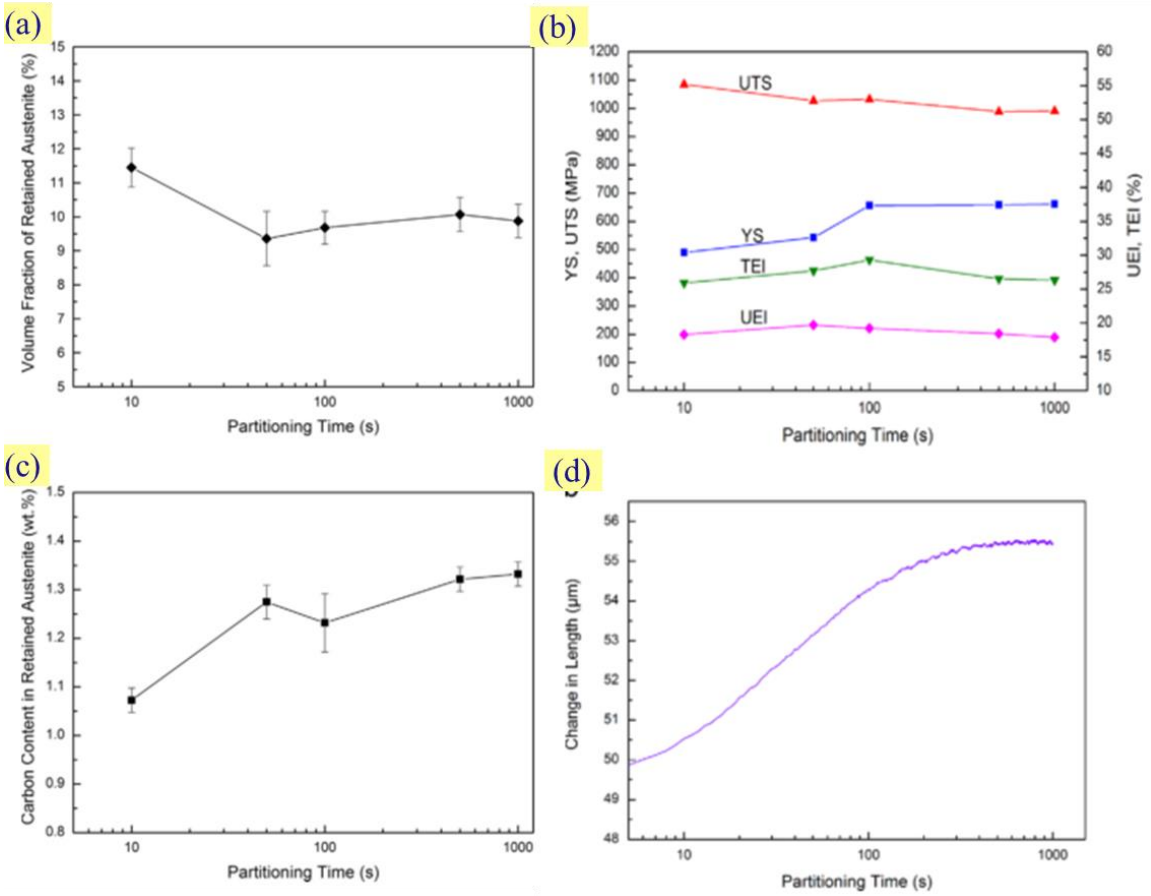

Figure 19: Variation of (a) austenite fraction, (c) carbon content and (b) mechanical properties and (d) length change with partition time at PT of 400°C as reported in work of Sun et al. [71]

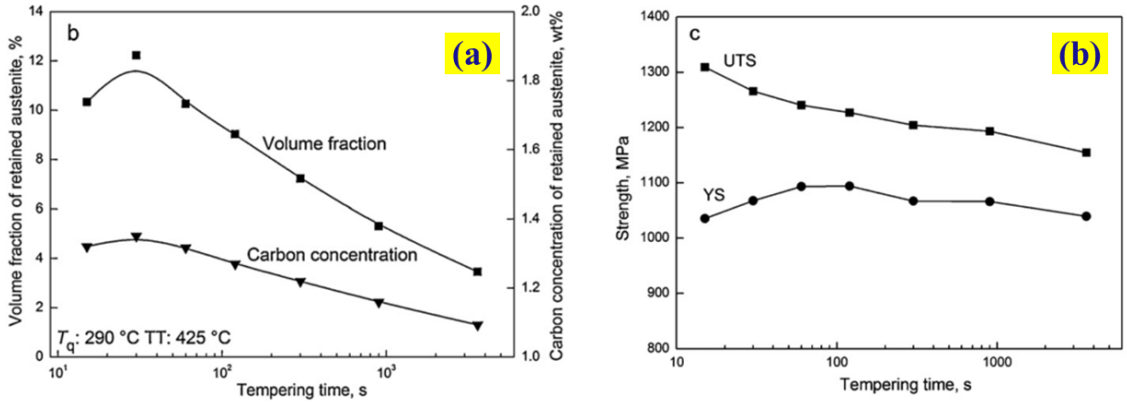

Figure 20: Effect of partitioning time on (a)austenite fraction and carbon content, (b) UTS and YS at PT of 425°C from work of Zhou et al. [70]

1.4.3. Austenite stability in Q&P steels

In comparison to other TRIP steels, austenite stability in Q&P steels is further complicated by the multiphase microstructure comprised of martensite, bainite, austenite and carbides. The factors affecting austenite stability are similar to TRIP steels however they could have significantly larger variations. The morphology of austenite is distributed between blocky and film-type austenite that is usually between martensite laths. The presence of considerably harder martensite phase around austenite grains is also likely to influence its mechanical stability through the distribution of transformation accommodation slip.

The carbon content of remaining austenite is noted to increase during plastic straining due to earlier transformation of austenite grains with lower C content in the work of Tan et al. [72]. This indicates a variation of austenite stability in Q&P steels due to difference in austenite carbon content. Contrary to common expectations, recent investigations have concluded that stabilized blocky austenite grains are more carbon enriched than the film type austenite. Xiong et al. [73] studied the mechanical stability of retained austenite in a 0.22C-1.8Mn-1.4Si steel with ferrite-martensite-austenite multiphase microstructure and concluded that despite its lower carbon content, film type austenite is mechanically more stable than high carbon blocky austenite during deformation. The study used synchrotron based HEXRD and TEM studies to investigate the austenite characteristics after interrupted tensile tests. The possible factors suggested were the presence of harder martensite phase around film type austenite or higher residual stresses. Choi et al. [74] studied the distribution of carbon in the Q&P microstructure of a fully austenitized 0.29C-2.95Mn-1.59Si steel using a multi-model characterization technique that combines nanoscale secondary ion mass spectroscopy (Nano-SIMS) and electron back scattered

diffraction (EBSD). Line scans for austenite carbon content showed the film type austenite to have much lower carbon content compared to the blocky austenite. Knijf et al. [75] investigated the different factors affecting mechanical stability of austenite in Q&P steels and listed them in order of increasing importance: (i) particle size, (ii) morphology and (iii) crystallographic orientation. Larger particles were reported as the first to transform during plastic straining while the smaller particles survived to higher strain levels. Lamellar grains with large aspect ratio were found to be less stable than globular ones. The grains oriented perpendicular and under 45^{o} with respect to the tensile direction transformed more rapidly on application of stress. Li et al. [76]carried out in-situ study of deformation-induced transformation of retained austenite in a partially austenitized 0.176C-1.58Mn-1.3Si-0.26Al-0.3Cr processed with QT of 240^{o}C and PT of 420^{o}C for 1000secs. They classified retained austenite into four types according to their locations in the microstructure; 1) RA at grain triple edges, 2) twinned austenite, 3) film type austenite in between martensite laths and 4) RA completely surrounded by ferrite grains. The reported results showed that the first two types of RA had lower stability and transformed at early stages of deformation. The latter two went through grain rotation during initial stages of deformation and eventually transformed at higher levels of deformation. The observations were attributed to different stress effects on austenite stability. Hidalgo et al. [77] studied the impact of martensite tempering on mechanical and thermal stability of RA in a fully austenitized 0.2C-3.5Mn-1.5Si-0.5Mo alloy that went through Q&P processing. The thermal stability measurements done via reheating experiments in a dilatometer showed that thermal recovery of martensite during reheating reduced the austenite stability. This was attributed to shrinkage and softening of martensite due to reduction in dislocation density and martensite carbon content.

1.4.4. Carbide precipitation in Q&P steels

The observed carbon content of austenite phase in the final Q&P microstructure is usually far less than that calculated for complete partitioning of carbon from martensite to austenite phase. The lower values are variously reasoned to be due to incomplete partitioning, carbon clustering or trapping at defects or formation of carbides such as cementite or transition carbides. Cementite is a common carbide observed by various researchers upon partitioning commonly at temperatures above 400^{o}C. At temperatures below 400^{o}C, there have also been studies reporting presence of transition carbides as they are favored by the short partition times associated with Q&P cycle. Silicon is also known to be less effective in suppressing transition carbides compared to cementite[78]. Quantitative analysis of the amount of carbide formed at different temperatures are not found in the literature due to the difficulties in measuring them. Quantitative XRD is a challenge owing to the small volume fraction, nanometer size scale and numerous overlapping peaks. TEM analysis is also difficult due to small size and complex diffraction patterns for carbides. APT studies provide useful insight into the composition of carbides but provide no structural information. Other techniques such as Mossbauer effect spectroscopy (MES) have the potential to provide quantitative information about carbides and are being used in more recent work.

Pierce et al. [79] in their work on a fully austenitized Q&P alloy (0.38C-1.54Mn-1.48Si, QT225_PT400) reported the presence of so-called η-transition carbides, (ordered ε) including non-stoichiometric carbides. The observations confirmed by TEM investigations estimated a substantial fraction (~24% to 41%) of alloy carbon lost in the form of carbides. Higher fraction of transition carbides (5at% vs 2.4at% in Q&P samples) were observed in quench and tempered

(Q&T) specimens of the same alloy. The authors also studied the effect of partition temperature and time on carbide precipitation in the same alloy [80]. The η-carbides were observed at both partition temperatures of 400^{o}C and 450^{o}C however, dissolving at longer partition times at 450^{o}C due to cementite precipitation. For longer partition time of 300s at 450^{o}C, the amount of alloy carbon lost to carbides increases to more than 70 percent. HajyAkbary et al. [63] identified the presence of transition ε-carbides using TEM selected area diffraction patterns in their fully austenitized alloy (0.3C-1.6Si-3.5Mn, QT180_PT400). The authors based on thermodynamic calculations suggest that metastable ε-carbides precipitate during the first quenching and dissolve upon holding at the partition temperature due to precipitation of more stable cementite.

Santofimia et al. [81] showed the presence of carbide precipitates inside tempered martensite using SEM micrographs in an inter-critically annealed 0.19C-1.6Mn-0.3Si-1.1Al alloy partitioned at 350^{o}C. Their study along with other similar studies[82] conclude that replacement of silicon with aluminum leads to a higher amount of carbide precipitation. Carbide precipitates were observed in 3DAPT reconstructions by Toji et al. [83] on a Q&P processed 0.59C-2.9Mn-2Si alloy. The carbides contained more than 20at% of carbon while no significant partitioning of substitutional solutes was observed after tempering for 300s at 400^{o}C, indicating carbide paraequilibrium.

Jiang et al. [84] reported the presence of cementite precipitates in a fully austenitized 0.2C-1.84Mn-1.5Si alloy processed with QT of 240^{o}C and partitioned at 400^{o}C for 60sec. The carbides were confirmed to be cementite using TEM SAD diffraction pattern. The cementite particles were found depleted in silicon while manganese content was closer to the bulk alloy content. Zhou et al. [70,85] reported the presence of hcp ε-carbides in their work on fully

austenitized 0.25C-1.48Mn-1.2Si-1.5Ni-0.05Nb alloy. At a PT of 350°C, parallel flakes of fine carbides were identified to be transitional hcp ε-carbides. They also noted precipitation of fine Nb containing complex alloying carbides at PT of 425°C from TEM analysis. Longer time at this temperature resulted in cementite precipitation.

The presence of cementite, NbC and ε-carbides has been shown with help of TEM diffraction study by Zhou et al. [70] on Q&P processed Fe-0.25C-1.5Mn-1.2Si-1.5Ni-0.05Nb alloy. Bright and dark field micrographs with SAD patterns for the three carbides are shown in Figure 23. Silicon addition to the alloy was confirmed to help prevent cementite precipitation at shorter partition times. However, it could not suppress cementite precipitation at longer partition times or ε-carbides at lower partition temperatures.

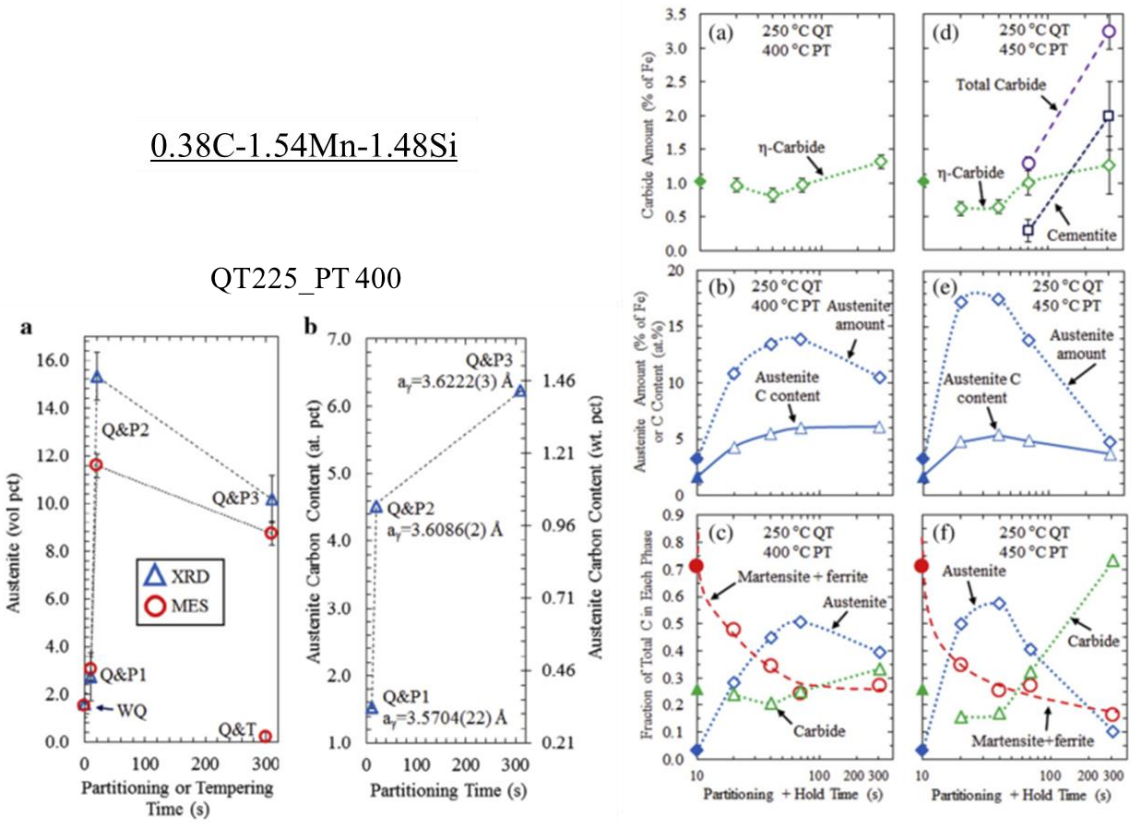

Figure 21: Quantitative analysis of carbide precipitation in Q&P alloy by Pierce et al. [79] [80]

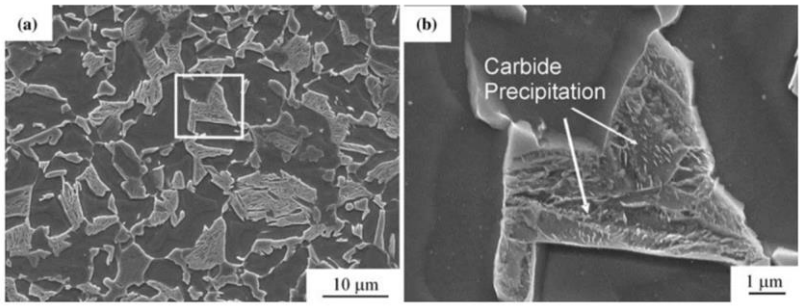

Figure 22: SEM micrographs showing carbide precipitation inside tempered martensite in the study by Santofimia et al. [81]

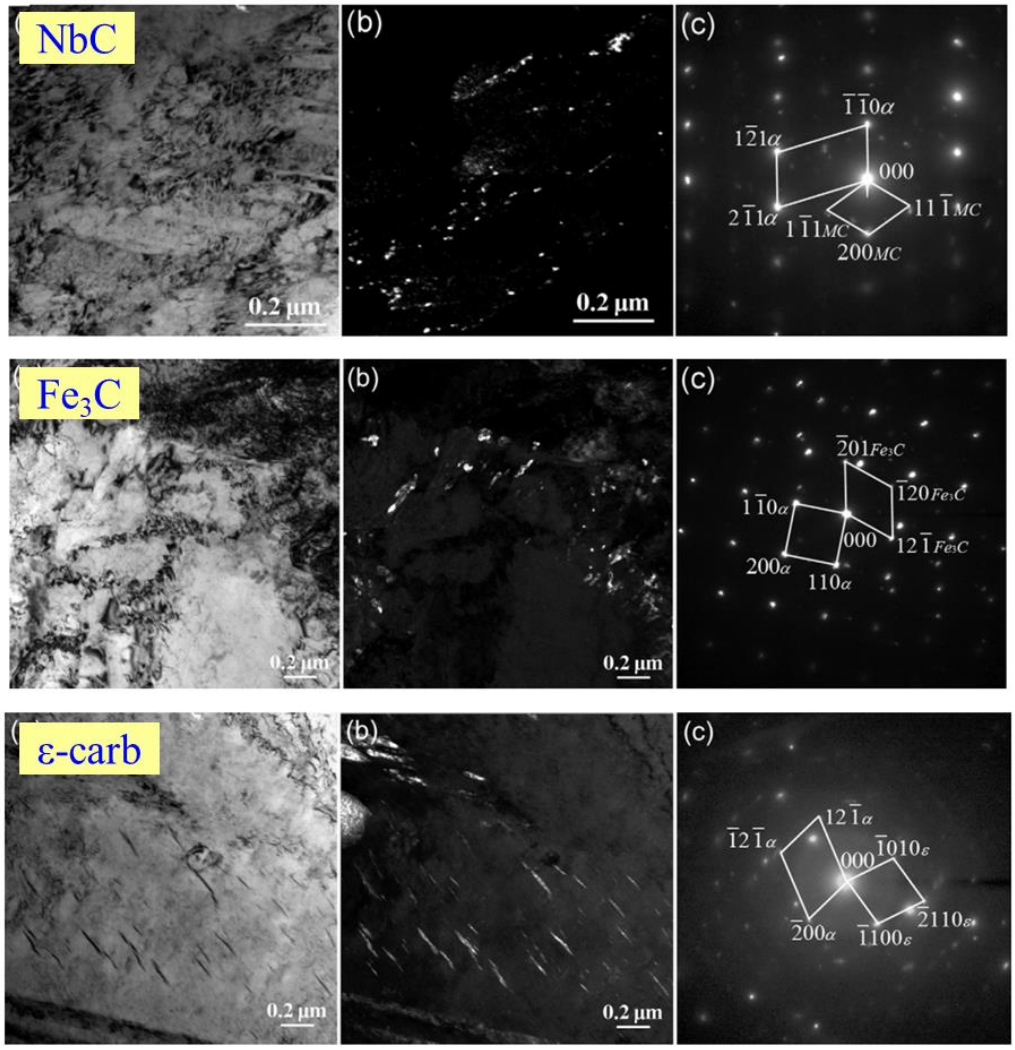

Figure 23: Different types of carbides observed by Zhou et al. [70] through TEM analysis on a Q&P processed Fe-0.25C-1.5Mn-1.2Si-1.5Ni-0.05Nb alloy

1.4.5. Mechanical properties and applications of Q&P alloys

Quench and Partition steels are known for their excellent combination of strength and ductility. The hard martensite matrix provides for the high strength while transformation of the stabilized retained austenite provides the excellent ductility. A comparison of the properties of Q&P steels with other AHSS was noted in the work of Speer et al. [86]. As seen in Figure 24, Q&P steels have higher strength compared to DP or intercritical-annealed TRIP steels while maintaining similar levels of ductility. In comparison to fully martensitic steels, they have improved ductility along with similar strength levels. A similar study comparing DP, TRIP, bainitc and Q&P steels was reported by Matlock et al. [3,87]. Figure 25 shows Q&P steels showing the best property combination. In some cases, bainitic steels have been reported to have high strength and ductility values similar to Q&P steels; however, the heat treatment cycle is considered to be too long for practical applications. The DOE targets for 3rd generation high strength steels as marked correspond to tensile strength and total elongation combination of 1500MPa/20% or 1200MPa/30% [88,89].

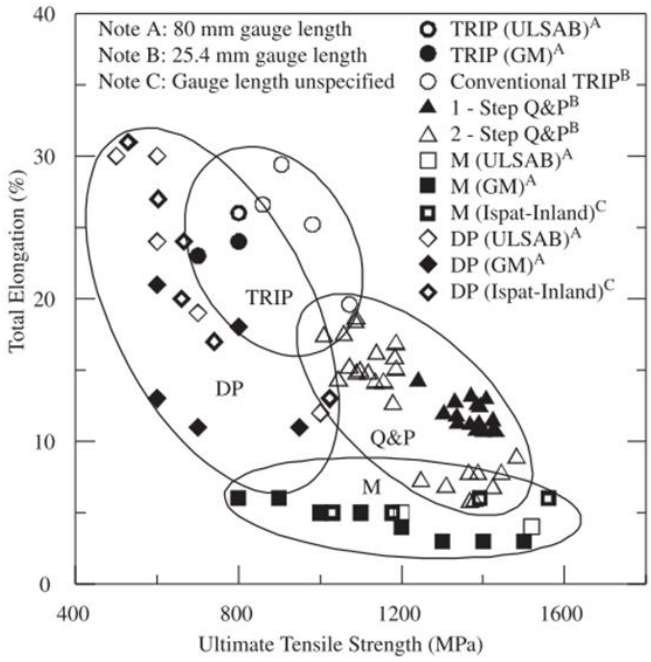

Figure 24: Mechanical property combination (TE vs UTS) for dual phase (DP) steels, Martensitic (M) steels, TRIP and Q&P steels [86]

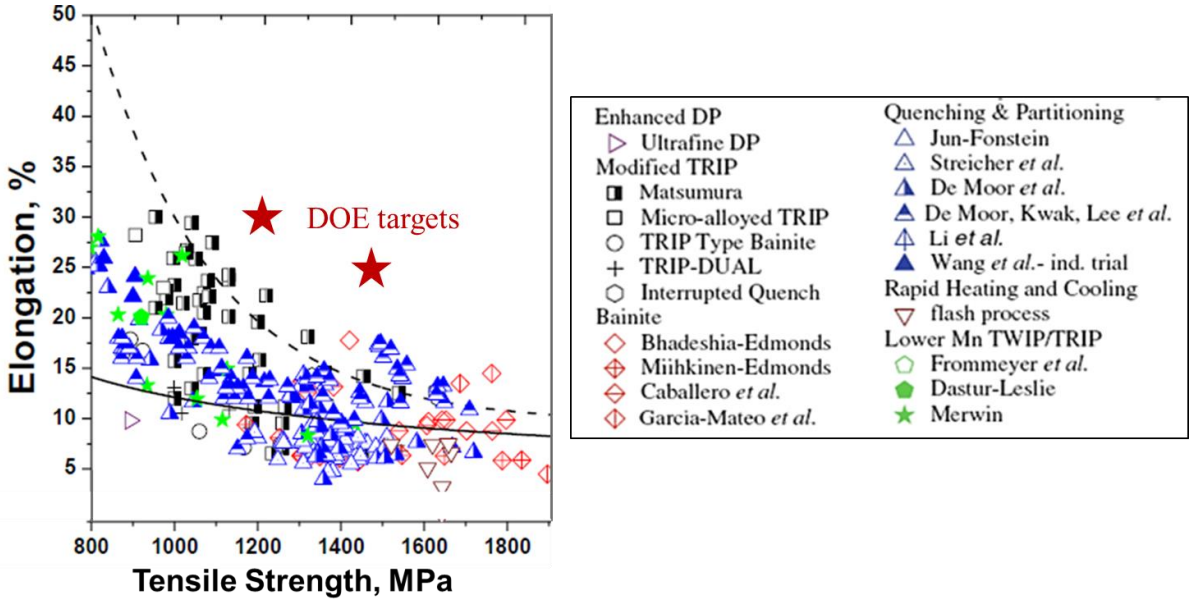

Figure 25: Mechanical properties combination of Q&P alloys from various research efforts [3,87]

1.5. Motivation and goals of present work

As discussed earlier, increasing demand for higher fuel efficiency in the automobile industry has led to the push for development of 3rd generation of AHSS. Steels with higher strength and sufficient ductility make it possible to use thinner gauge sections in automotive applications. This leads to decrease in the overall weight for improved fuel mileage. In the light of this demand, a significant number of research efforts have been undertaken to get the best performance out of the 3rd generation AHSS, especially Q&P steels. Most efforts rely on an empirical design of experiments approach to quantify the effect of individual factors including overall composition and Q&P processing parameters. Although useful correlations have been obtained from these efforts, it is difficult to separate out effect of one parameter as there are many parameters that are highly interdependent. For example: the effect of processing parameters such as partition time vary for different alloy composition or the role of PT would differ for different QT. Hence, the motivation of the current work is to develop ICME based mechanistic models grounded in quantitative phase transformation and transformation plasticity theory to predict the key microstructural characteristics that control the desired properties. The developed thermodynamic and kinetic models fully incorporate the effect of alloy composition and processing parameters. The models which have been calibrated with state of the art characterization measurements can now be used to computationally design an alloy composition and processing cycle to achieve the best combination of mechanical properties.

The goals of the present work can be briefly summarized as follows:

1. Provide accurate experimental data for carbon partitioning using high resolution characterization techniques such as 3DAP and HEXRD.
2. Calibrate thermodynamics-based predictive models for austenite carbon enrichment as a function of alloy composition and processing parameters.
3. Evaluate the variation of austenite stability with Q&P processing parameters and calibrate thermodynamic models to predict austenite stability for any given alloy composition and Q&P cycle.
4. Validation of the calibrated models for austenite carbon content and its stability after Q&P processing.
5. Quantify the variation in competing carbide precipitation with processing conditions and determine possible thermodynamic parameters that could be used to predict its precipitation behavior.
6. Design new alloy compositions and Q&P cycles to achieve the DOE mechanical properties target.

1.6. ICME based genomic design approach for Q&P steels

1.6.1. Materials by design concept

The traditional process of new alloy or process development involves the commonly used ‘trial and error’ method that has the obvious drawbacks of being expensive and overly time consuming. In contrast, a systems-based approach initially advocated by Smith[90], that integrates the process/structure/property/performance relations for predictive design of multilevel-structured high performance materials has now been proven to be more useful and economical [91]. The materials by design methodology uses the goal/means approach to design a material or process with a desired level of performance. The desired performance decides the property objectives that define the microstructure requirements. The established relationship of processing with microstructure aids in the design of an optimal processing route that results in the desired microstructure. In the three-link chain representation of the materials design paradigm shown in Figure 26, the deductive cause and effect logic of science flows to the right, while the inductive goals-means relations of engineering flow to the left [91,92].

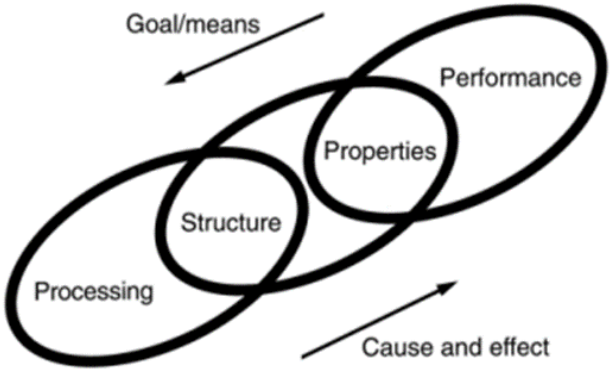

Figure 26: Three link chain showing relation of processing, structure, properties and performance of materials

1.6.2. Systems design chart

The design approach for Q&P steels can be represented by further breaking down the four primary elements: processing, structure, properties and performance, and portray their interactions across a multiscale hierarchy of subsystems by a system flow-block diagram. Figure 27 shows the system chart that was developed in part of this work for quench and partition steels.

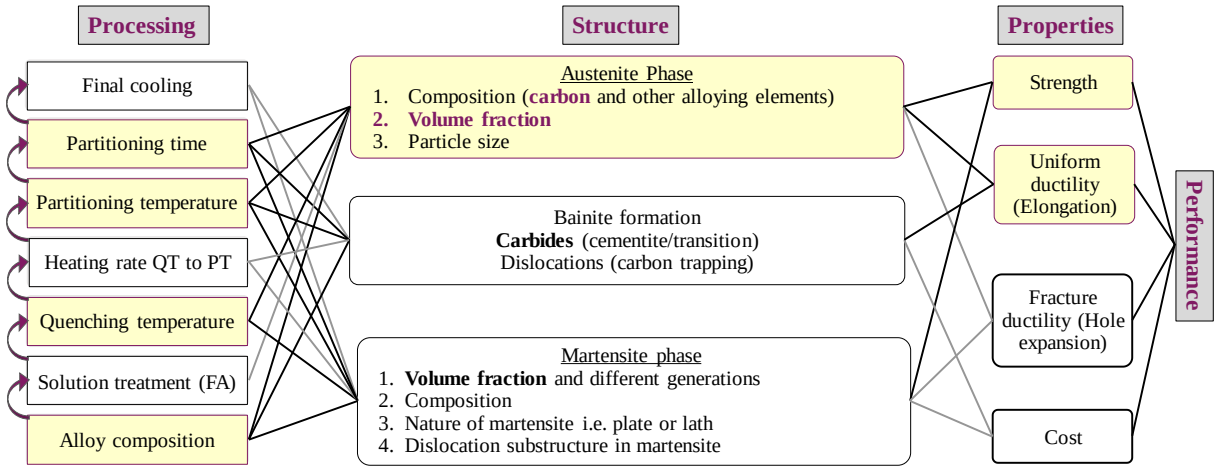

Figure 27: Systems design chart for Q&P processing

The desired performance standards for Q&P alloys were defined in the property objectives of tensile strength, uniform ductility, hole expansion ductility and alloy cost. The current work focussed on maximizing the combination of tensile strength and ductility. The relationship of microstructure to properties for these alloys was established. The key structure parameters influencing the properties are the austenite phase fraction and composition in addition to martensite fraction and carbide preciptiation. The connection of processing to structure of the material was derieved. As discussed previously, the important processing variables affecting the key structure parameters are alloy composition, quench temperature, partition temperature and P-time. Detailed understanding and predictive modeling of the interpalay between the individual

elements of processing, structure and properties would be critical to design a material to achieve desired performance level.

1.6.3. Design flowchart

The objective of the thesis research was primarily to develop non-equilibrium thermodynamic models to predict key microstructural characteristics that control the final mechanical properties. A secondary objective of the project was to simultaneously use these predictive models to iteratively design new prototype materials and QP processing cycles to achieve a set of property goals. The iterative cycle of designing a new alloy or processing cycle is described in the form a 'Design flowchart', as shown in Figure 28(a).

The design process begins with a given alloy composition and set of Q&P processing conditions. The first step involved examining the essential alloy characteristics required for Q&P processing that includes sufficient hardenability, low overall alloying additions and a Ms temperature feasible for practical manufacturing. After that, the material would be experimentally studied using various tools to identify the key microstructural features and mechanical properties. Some of the key measurements include phase fraction estimates using high energy x-ray diffraction and dilatometer, phase composition using atom probe tomography and high energy x-ray diffraction, phase morphology using electron back scattered diffraction analysis. Mechanical property measurements include the standard uniaxial tensile tests to measure the ultimate tensile strength (UTS), yield strength (YS), uniform (UE) and total elongation (TE) of the material. A key parameter to quantify austenite stability known as 'Ms^{σ} temperature' is also experimentally measured using 'Bolling-Richman tensile tests' as described in later sections. After experimental analysis, the design is checked against the set design performance goal of property combinations.

The next step is to develop the mechanistic models to connect the alloy composition and processing conditions to the key microstructural features. The modeling section primarily consists of two models, 1) Carbon partitioning model and 2) Austenite stability model. The carbon partitioning model uses Thermocalc based para-equilibrium simulations with an added temperature-dependent 'effective stored energy' model based on theory of coupled diffusional/displacive transformation [33,34] to predict the carbon enrichment in austenite phase. It also includes DICTRA based para-equilibrium simulations to predict the influence of partition time on homogenization of carbon in the austenite phase. Experimental measurements of austenite composition and phase fractions are used to calibrate and improve these models. The austenite stability model uses the predicted austenite composition to calculate a single quantifiable parameter for austenite stability corresponding to the 'Ms^{σ} temperature'. It uses the martensite nucleation theory developed by Olson-Cohen [14,93] to predict austenite stability. The model uses experimental mechanical property measurements to calibrate key physical parameters to ensure accurate prediction of austenite stability. The developed thermodynamic models along with the understanding of observed alloying effects can now be used to design a new alloy composition or QP processing cycle to achieve improved property combinations. The new designed prototype alloy is further analyzed in the same manner to continue improvement of the models and check against desired property objectives.

Figure 28(b) shows a flowchart that explains the working of the thermodynamic models to determine the austenite stability for any given alloy composition and Q&P processing cycle. The para-equilibrium carbon partitioning model uses the effective stored energy input to determine the austenite carbon content for any given composition and Q&P cycle. The austenite stability

calculations based on the Olson-Cohen model uses the austenite carbon content and outputs of the three free energy models (chemical, mechanical and critical free energy) for martensitic transformation to predict the austenite stability in terms of the Ms^{σ} temperature. The experimentally measured values for austenite carbon content and Ms^{σ} temperature are used to calibrate the stored energy model and critical free energy model respectively.

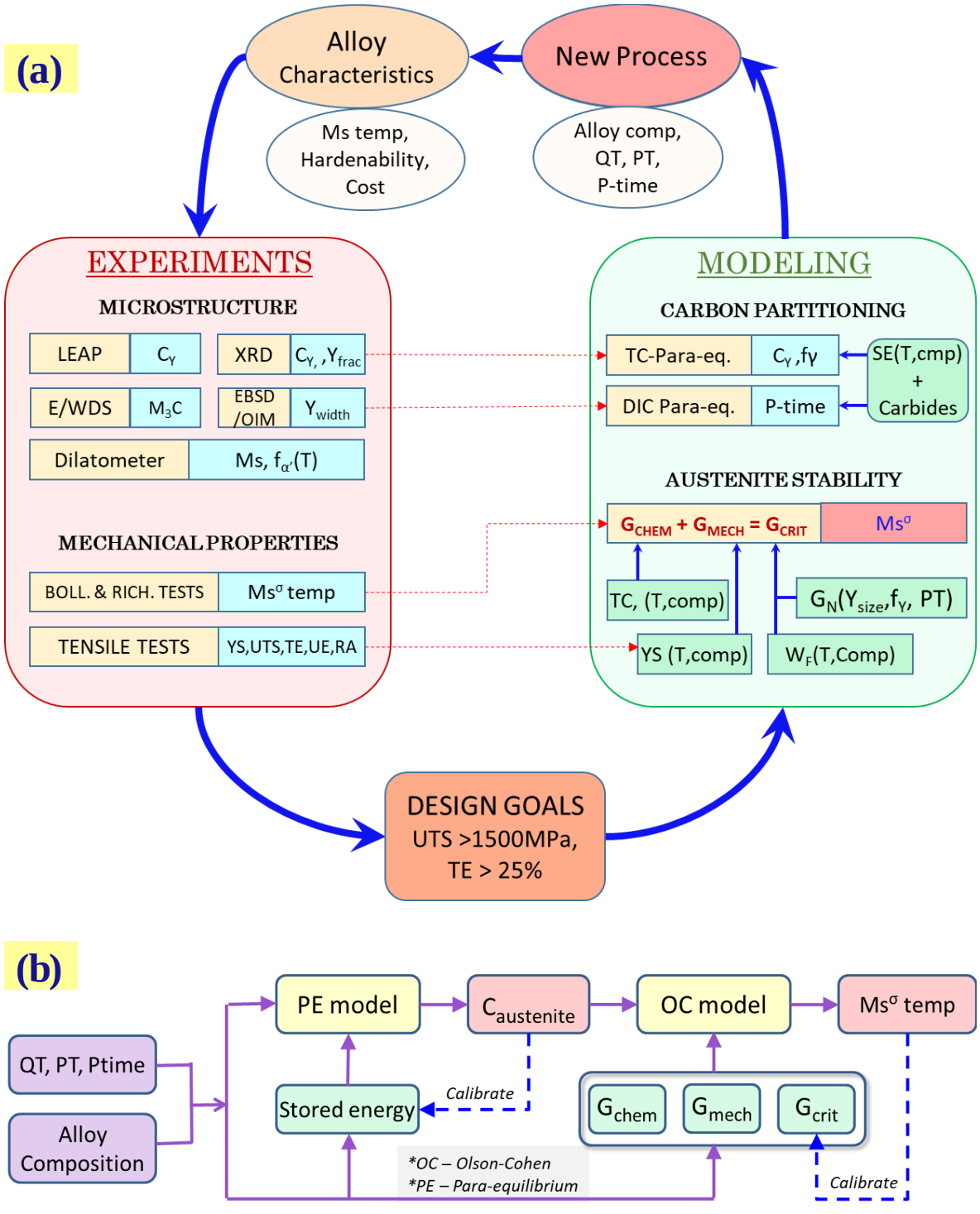

Figure 28: (a) Design flowchart showing the cycle of materials design used in the current work, (b) Flowchart describing the working of the developed thermodynamic models

Chapter 2. Materials, Experimental procedures and Computational methods

The present chapter outlines the different alloy compositions studied in the work and the new designed alloys that were made to calibrate and validate the developed thermodynamic models. The experimental characterization tools used in the project are briefly described and the procedure followed to obtain the information is elaborated. These include the microstructure characterization tools and the mechanical testing methods to quantify the role of alloy composition and processing cycle. The computational methods developed to model different characteristics of the microstructure and their influence on the final mechanical properties are also described.

2.1. Steel compositions

The research work started with a standard low alloy Q&P alloy composition provided by the sponsor industrial partner, ArcelorMittal Global R&D. The exact composition of the steel (named Steel_1) is stated below. The steel was made to undergo a set of different QP cycles to quantify the effect of processing parameters on its microstructure and mechanical behavior. These will be described in the following section. In some cases, the effect of specific parameters was studied in different alloys with slightly different composition due to material availability issues. The observations would however hold for any composition in the studied ranges. Based on these analysis, a series of new prototype alloys were prepared to further calibrate and validate the developed models. The compositions of the alloys with their designated names for easy reference are reported in Table 6.

Table 6: Alloy compositions studied in the current work (all in wt%)

	Name	C	Mn	Si	Mo/Cr	Nb	other
Initial	**Steel_1**	0.2	2.2	1.5	0.2Cr	0.04	-
	Steel_2	0.18	2.02	1.55	0.15Mo	0.04	-
New designed alloys	**Steel_121**	0.2	1.8	1.5	0.2Mo	0.04	20ppm B + 0.025Ti
	Steel_122	0.2	1	1.5	0.2Mo	0.04	20ppm B + 0.025Ti
	Steel_123	0.3	1	1.5	0.2Mo	0.04	20ppm B + 0.025Ti
	Steel_124	0.25	0.75	2	0.2Mo	0.04	0.75Cu + 0.38Ni
	Steel_125	0.3	0.5	1.5	0.2Mo	0.04	1Cu + 0.5Ni
	Steel_126	0.25	0.75	2	0.2Mo	0.04	-
	Steel_130	0.25	1.5	2	0.2Mo	0.04	-

2.2. Experimental procedures

This section describes the different experimental facilities used to prepare and study the QP alloys including the sample preparation procedure followed for each of these tools.

2.2.1. Heat treatments and sample preparation

For the current study, Q&P thermal processing of the steel was carried out in two ways:

A) Quenching dilatometer:

A Bahr DIL 805A/D dilatometer at ArcelorMittal Global R&D was used to process the steel under the designed Q&P processing cycle. The specimen used in the dilatometer were small rectangular shaped sheet samples with dimensions of 4mm x 10mm x thickness of sheet. These specimens were induction heated to the austenitizing temperature in an inert atmosphere and then fast cooled using Ar/N2 cooling. The exact temperature of the specimen was measured by means of a thermocouple spot welded onto its surface.

B) Continuous Annealing system (CAS):

Mechanical testing of QP processed material requires sheet samples larger than dilatometer specimens which were heat treated using a continuous annealing system (CAS) for sheet steel samples at ArcelorMittal Global R&D. The CAS series can achieve high-speed heating/cooling rates, direct temperature control, and inert atmosphere conditions. The heat-treated samples were then machined using electrical discharge machining (EDM) to prepare ASTM sub-size samples for mechanical testing.

The current work involved processing of the alloys according to different sets of Q&P cycles. The investigated Q&P cycles are all listed in Table 7. They are referred in the text by their QT followed by PT and Ptime, for example QP270_PT430_75s. Temperatures are always given in degree Celsius.

Table 7: List of Q&P processing parameters studied for the different alloys

	Name	**QT(ºC)**	**PT(ºC)**	**Ptime (sec)**
Initial	**Steel_1**	270	430, 410, 390	75, 100, 150
Designed Q&P cycles	Steel_2	290	420	75
		190, 210…350	440	60
		290	440	10,30,60,100,200
	Steel_121	310	420	75
	Steel_122	325	450	60
	Steel_123	300	430	75
	Steel_124	275	410	250
	Steel_125	250	420	250
	Steel_126	295	435	75
	Steel_130	275	410	100
		175,200…325	430	60

2.2.2. Microstructural characterization

A wide variety of characterization techniques was used to identify key aspects of the complex microstructure in these Q&P processed materials. These include electron microscopy techniques, diffraction-based methods and others.

a) Dilatometer

Dilatometry is a powerful technique utilized for the investigation of solid-solid phase transformations in steels as it permits real time monitoring of dimensional changes occurring on application of a thermal cycle. The dimensional changes can be interpreted in terms of phase transformations occurring in the specimen during the heat treatment cycle. A Bahr DIL 805A/D dilatometer was used to Q&P process the steel samples while measuring the change in length, plotting it as a function of applied temperature and time. Rectangular sheet samples (4mm x 10mm x sheet thickness) were held in between quartz push rods that can accurately measure any small dimensional changes. Fast heating rates were achieved with help of an induction heating coil surrounding the sample, while fast cooling was realized with injection of cold Ar/N_2 gas. The technique is very useful to accurately measure the various transformation temperatures (Ac1, Ac3, Ms etc) and to estimate the degree of transformation completion comparing different sets of samples.

b) Electron microscopy

Electron microscopy techniques use electrons instead of light to form an image of the sample. The sample is hit by a continuous beam of electrons to produce various signals: secondary electrons, back scattered electrons, characteristic x-rays, which are collected and used to generate

the final image. Several electron microscopy techniques were used at Northwestern to study the steel microstructure in the current work.

Scanning electron microscopy (SEM) is a versatile and powerful imaging technique widely used to study the microstructure of a wide range of materials. Samples for SEM were ground and polished to mirror-like finish using standard metallographic techniques. Thereafter the samples were thoroughly cleaned and etched with 5% Nital solution (5 vol% HNO_3 in ethanol). Nital etching helps to identify key microstructural features such as grain boundaries and phase boundaries. Etched samples were studied using a FEI Quanta ESEM operated under voltage conditions of 20-30kV.

Transmission electron microscopy (TEM) was used in some cases to identify microstructural features that would be too fine to be captured using SEM. The sample preparation employed electro-polishing using a solution of perchloric acid and methanol. The current due to the applied voltage helps dissolve the sample to make a tiny hole at the center. Microstructural studies are then performed in the thinned region of the sample around the hole. TEM studies were performed using a Hitachi H-8100 TEM operating at 200kV.

The Electron backscattered diffraction (EBSD) technique is useful to identify the different phases present in the microstructure and determine their crystallographic orientation. In the present work, EBSD was used to identify the retained austenite phase in the martensite matrix. The orientation mapping of the phases (Orientation-Imaging microscopy, OIM) was used to identify the prior austenite grain size, martensite block and packet sizes. Samples for EBSD and OIM analysis were prepared using mechanical polishing methods as well as electropolishing techniques. For mechanical polishing, the samples were prepared using a vibratory polisher after

conventional polishing to remove the top strain-affected zone and eliminate any retained austenite that would have transformed to martensite during polishing. Electropolishing techniques were in some cases used with help of a Struers LectroPol instrument using a solution of 78ml perchloric acid + 100ml 2-butoxyethanol + 90ml distilled water + 730ml ethanol. The samples were polished at a voltage of 40V for 10 seconds. The EBSD and OIM experiments were carried out on a FEI Quanta ESEM fitted with an Oxford HKL EBSD detector. The analysis was performed under the conditions: accelerating voltage 30kV, working distance 15mm, tilt angle 70^{o}, step size 70nm.

c) X-Ray diffraction

X-Ray diffraction is one of the most commonly used techniques to measure austenite phase fraction and retained austenite carbon content in steel research. Samples studied using XRD were fine polished incrementally to a final polishing step using 1μm suspended alumina solution. Thereafter they were chemically polished by immersing in a solution of $HF+H_2O_2$+distilled water (1:10:10 ratio) for 5 minutes. This was done to remove any stress-affected region close to the surface due to mechanical polishing.

High energy X-Ray diffraction (HEXRD) experiments were carried out using high energy radiation from the Advanced Photon Source at Argonne National Lab (ANL). The wavelength of the radiation was measured before each set of experiments and was approximately 0.71116Å. HEXRD experiments were preferred over the lab XRD setup mostly due to the advantage of higher flux with the synchrotron source. Higher flux enabled larger peak to noise ratio even for the small intensity peaks coming from small fractions of retained austenite. This resulted in precise measurement of austenite lattice parameter. Austenite phase fraction was measured using

two austenite [{200}, {211}] and two martensite peaks [{200}, {220}], comparing them with their theoretical intensities. The carbon content of austenite phase was estimated by measuring austenite lattice parameter from the (111), (200), (220) & (311) austenite FCC peaks. The empirical equation used to relate austenite lattice parameter with its composition is given below [83], corresponding to a combination of equations from Ruhl and Cohen[94] for Mn, Si, C and Dyson and Holmes[95] for Al.

$$a_\gamma = 3.572 + 0.033*X_C + 0.0012*X_{Mn} + 0.00157*X_{Si} + 0.0056*X_{Al} \ldots \text{(in wt\%)}$$

d) Atom probe tomography

Atom Probe Tomography (APT) is a materials analysis technique that allows for both 3D imaging and chemical composition measurement at the atomic scale [96]. The recently developed three-dimensional local electrode atom probe (3D-LEAP) provides nano-scale surface, bulk and interfacial materials analysis of structures with atom-by-atom identification and spatial positioning. The instrument is based upon principle of field evaporation of the material in the form of ions upon application of a strong electric field, laser pulse or both. The specimen is prepared as a sharp needle tip and the application of a repeated voltage pulse or laser pulse removes atoms from the tip one-by-one. These atoms (as ions) are detected by a position sensitive imaging mass spectrometer and are identified based on their mass to charge ratio determined by their time of flight from specimen to detector. A schematic for 3DAP operation is shown in Figure 29(a) [97]. It shows the position of local electrode in relation to the needle-like specimen and the position of the detector of incoming ions based on their time of flight information. A representative mass spectrum plot with peak labels for individual ions is shown in

Figure 29(b). The peaks, especially for carbon which also comes out in the form of molecular ions, were identified based on previous research [54,98,99].

Needle-shaped specimens for local electrode atom probe (LEAP) studies were prepared via electropolishing using a solution of 2-Butoxyethanol and perchloric acid in methanol. Further detailed information about the sample preparation can be found elsewhere [100,101]. LEAP experiments were carried out on a LEAP 4000X Si instrument at Northwestern NUCAPT, operating in laser mode with laser energy of 25pJ and specimen at a temperature of 40K. The laser frequency was set at 500kHz and evaporation rate was generally set at 0.5%.

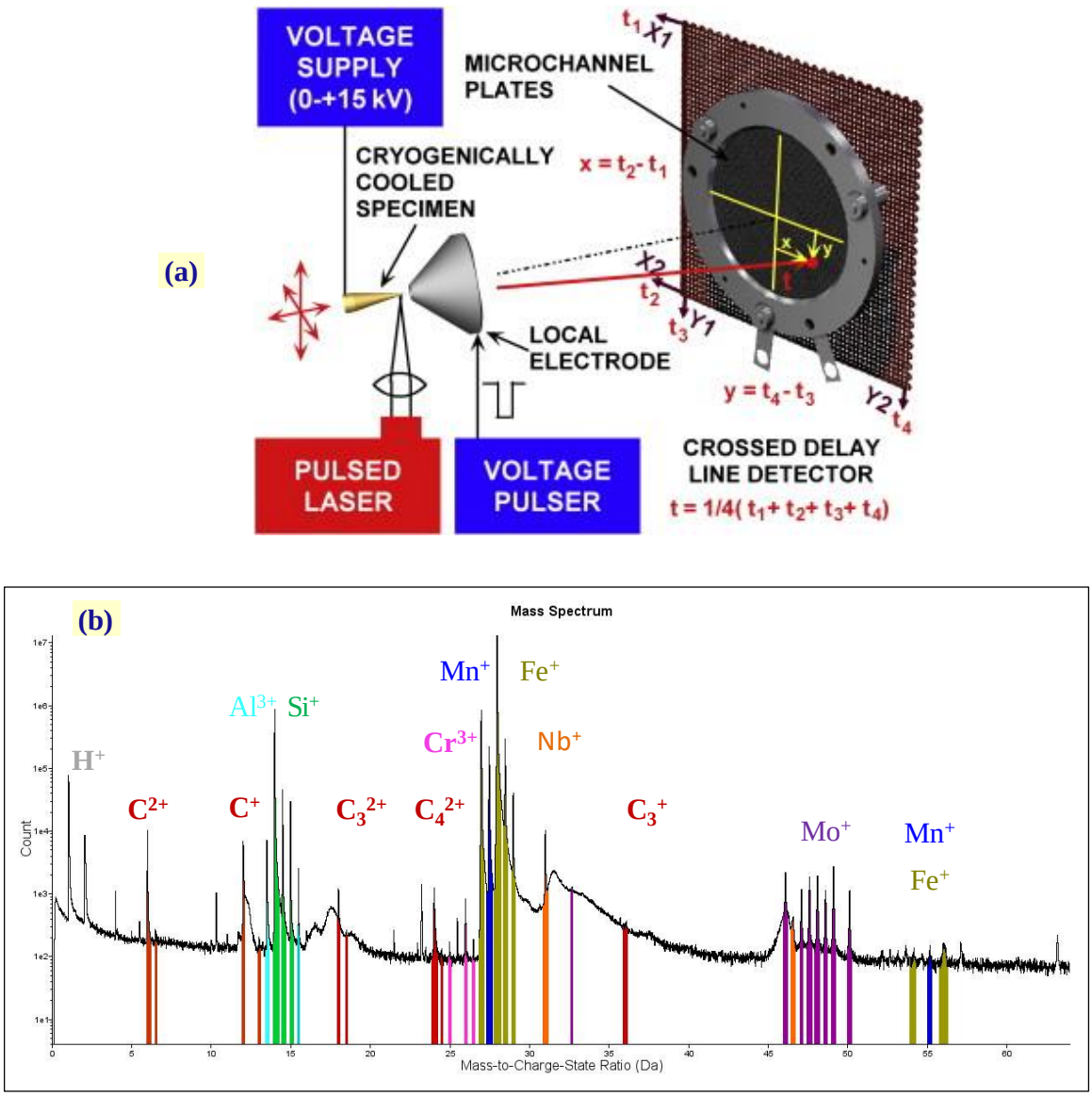

Figure 29: (a) Schematic of 3DAP showing the needle like specimen, the position of local electrode and the detector [97], (b)Mass spectrum of the ions observed in a 3DAP experiment with labels identifying the individual ions

2.2.3. Mechanical tests

The mechanical properties of the different samples were measured using a Sintech 20G tensile testing machine at Northwestern CLaMMP facility equipped with a heating/cooling furnace to run tests in the range of -50^{o}C to 160^{o}C. Standard ASTM subsize specimens (gauge length 25mm) were used for almost all the tests. A strain rate of 0.05mm/min was used for all the tests. Single-specimen Bolling-Richman tests [102] were carried out to measure the characteristic Ms^{σ} temperature for the individual samples. The test is designed to measure the variation of yield stress in a single specimen upon repeated testing at different temperatures going from high to low temperature. The sample is first heated to the maximum test temperature and loaded to slightly past its yield point. Then it is completely unloaded and the sample temperature lowered to the next set temperature step. Thereafter the sample is again loaded just past its yield stress and unloaded. The steps are similarly repeated until the lowest test temperature. The peak in the yield stress variation corresponds to the Ms^{σ} temperature and is further discussed in later sections.

In addition to single specimen tests, multiple specimen tests were also performed to measure the variation in properties with test temperature. These tests accurately determine the Ms^{σ} temperature without the complexity of strain accumulation from repeated testing on the same specimen in the Bolling-Richman technique.

2.3. Computational models developed

2.3.1. Martensite transformation models

Martensite start temperature: One of the most important phase transformations that enabled development of ultra-high strength modern steels is the austenite to martensite transformation. The diffusionless transformation has been utilized over the years in different generations of AHSS including the new 3rd generation Q&P AHSS. This has led to numerous research efforts towards modeling its transformation temperatures and kinetics of transformation.

Numerous empirical linear-regression relationships to predict the Ms temperature for a given alloy composition have been proposed as early as 1944 by Payson and Savage as listed in Table 8. Since then several different empirical equations have been suggested and been thoroughly reviewed in the works of Wang et al.[103] and Sourmail et al. [104]. These expressions are usually the result of regression analysis on a large set of experimentally determined Ms temperatures employing a set of linear or non-linear dependencies and ignoring interaction effects. The effect of binary interactions was also attempted to be incorporated into Ms predictions in a new empirical model proposed by Wang et. al. [103].

Table 8: List of empirical relationships for Ms temperature
(adapted from Sourmail et al. [104])

P. Payson, C.H. Savage, Trans. ASM 33 (1944) 261–281	772–316.7C–33.3Mn–11.1Si–27.8Cr–16.7Ni–11.1Mo–11.1W
R.A. Grange, H.M. Stewart, Trans. AIME 167 (1945) 467–494.	811–361C–38.9Mn–38.9Cr–19.4Ni–27.8Mo
A.E. Nehrenberg, Trans. AIME 167 (1945) 494–501.	772–300C–33.3Mn–11.1Si–22.2Cr–16.7Ni–11.1Mo
W. Steven, A.G. Haynes, JISI 183 (1956) 349–359	834.2–473.9C–33Mn–16.7Cr–16.7Ni–21.2Mo
K.W. Andrews, JISI 203 (1965) 721–727	812–423C–30.4Mn–12.1Cr–17.7Ni–7.5Mo
	785–453C–16.9Ni–15Cr–9.5Mo+217(C)2–71.5(C)(Mn)–67.6(C)(Cr)

The development of martensite nucleation theory led to the development of mechanistic thermodynamic based models to predict martensite transformation temperatures. These models were based on predicting the critical driving force for transformation as a function of temperature and alloy composition. Some of the first analysis of thermodynamic properties in the Fe-C system by Johansson[105] and the Fe-Ni system by Kaufman and Cohen[106] were used to calculate the critical driving forces at experimentally measured Ms temperatures. Hsu and Hongbing [107] worked to evaluate the diffusionless critical driving force for fcc-bcc transformation at Ms temperature and study its compositional variation. In the years since then, extensive work in the field has led to the modern CALPHAD methodology of determining transformation characteristics based on thermodynamic properties. Some of the more recent reliable mechanistic expressions for critical driving force are results of the work of Ghosh and Olson [108] and Wang et al. [109].

Ghosh and Olson performed an extensive study in 1994 by determining the driving force at experimentally measured Ms temperatures for a large set of alloy compositions. They fitted the critical driving force ($\Delta G_m^{\gamma-\alpha}$) data to alloying content (x_i) establishing the effect to be similar to the effect of alloying addition on solution hardening from the theory of slip deformation [110,111].

$$\Delta G_{crit} \text{ or } \Delta G_m^{\gamma-\alpha} = K_1 + W_\mu (K_\mu^i, X_i) + W_{th} (K_o^i, X_i, T, T_\mu)$$

where K_1 is a constant temperature independent parameter that included an elastic energy (g^{el}), interfacial energy and defect size. W_μ & W_{th} are the athermal (only composition dependent) and thermal (both composition and temperature dependent) components of interfacial frictional work,

respectively. The parameter K_μ^i & K_o^i were evaluated for a large set of alloying elements and reported by Ghosh and Olson [Part I[108] and II[112]]. In the early model, it was approximated that the shear modulus would have a weak composition and temperature dependence which was later quantified and included in the improved description of the athermal frictional work [113]. The final forms of critical driving force and frictional work including the shear modulus dependencies are reported here:

$$\Delta G_{crit} = -\left[g^{el} + \frac{2\sigma}{nd} + w_\mu + w_{th} \right]$$

where n is the thickness of the critical nucleus stabilized by the defect interaction and it is measured in units of interplanar spacing d of closest packed planes in the parent phase; g^{el} was initially interpreted as a shape insensitive component of the strain energy (per unit volume) associated with distortions in a rational nucleus habit plane; σ is the semicoherent interfacial energy; and w_μ and w_{th} are the athermal and thermal components of the interfacial solid-solution frictional work, respectively.

$$g^{el} = K^{el}\,\mu(X_i,T) \;;\; \sigma = K^{\sigma}\,\mu(X_i,T) \;;\; W_\mu = A_\mu\,\mu(X_i,T)$$

$$A_\mu = \sqrt{\sum_i \left(K_\mu^i\, X_i^{0.5}\right)^2} + \sqrt{\sum_j \left(K_\mu^j\, X_j^{0.5}\right)^2} + K_\mu^{Co}\, X_{Co}^{0.5}$$

where $\mu(X_i, T)$ denotes the composition (X_i) and temperature dependence of the shear modulus (μ) of austenite. The proportionality constants K^{el} and K^{σ} are evaluated as 9.4×10^{-4} and 1.8026×10^{-12} m, respectively. $K\mu$ – athermal friction coefficients noted for individual elements in Figure 30, X- atomic percent of alloying addition and i =Al, C, N, Cr, Mn, Mo, Nb, Si, Ti, V, W and j = Cu, Ni.

$$W_{th}(T) = W_o\left[\, 1 - \left(\frac{T}{T_\mu}\right)^{\frac{1}{q}} \right]^{\frac{1}{p}}$$

$$W_o = W_o^{Fe} + \sqrt{\sum_i \left(K_o^i \, X_i^{0.5}\right)^2} + \sqrt{\sum_j \left(K_o^j \, X_j^{0.5}\right)^2} + \sqrt{\sum_k \left(K_o^k \, X_k^{0.5}\right)^2} + K_{\mu}^{Co} \, X_{Co}^{0.5}$$

where *X*- atomic percent of alloying addition and *i* = C, N; j = Cr, Mn, Mo, Nb, Si, Ti, V and *k* = AI, Cu, Ni, W. T_{μ} = 500 K and, K_o – thermal friction coefficients noted for individual elements in Figure 30. The value of p=0.5 and q=1.5.

For multicomponent alloys, a Pythagorean gemetric addition rule was adopted inside each category of similar strengthening solutes and a linear superposition rule between the different categories representing solute of very different strengths. The calculated values of critical driving force when equated to the chemical driving force for martensitic transformation calculated using commercial thermodynamic databases provides accurate predictions for Ms temperatures with reported uncertainty of ±40K. This approach of calculating Ms temperature has been used in the current research work.

Some of the more recent work on thermodynamic modeling for Ms temperature are by Stormvinter et al.[114] using a semi-empirical method to estimate the critical driving force in order to compensate low temperature errors in commercial thermodynamic databases. Bohemen and Morsdorf [115] have also recently suggested extensions to the Ghosh and Olson model by including the effect of prior austenite grain size on Ms temperature, as quantified by Olson-Tsuzaki-Cohen [116].

(a) The modulus-normalized coefficients (K_μ representing the athermal friction of different solutes for the fcc/bcc martensitic interface in Eq 7(c)

Element	K_μ
C	0.01012
N	0.00859
Mn	0.00442
Cr	0.00425
Si	0.00375
V	0.00321
Mo	0.00311
Nb	0.00307
W	0.00284
Ti	0.00267
Al	0.00259
Cu	0.00119
Ni	0.00035
Co	−0.00057

(b) The athermal and thermal strengths of different solutes for f.c.c./b.c.c. martensitic interface in Fe-base system

Element	K_μ (J/mol)	K_0 (J/mol)
C	3807 ± 68	21,216
N	3048 ± 185	16,986[a]
Mn	1980 ± 79	4107
Si	1879 ± 215	3867[b]
Cr	1868 ± 72	3923
Nb	1653 ± 90	3402[b]
V	1618 ± 122	3330[b]
Ti	1473 ± 204	3031[b]
Mo	1418 ± 55	2918[b]
Cu	752 ± 12	1548[b]
W	714 ± 93	1469[b]
Al	280 ± 41	576[b]
Ni	172 ± 35	345
Co	−352 ± 110	−724[b]

[a] Based on a scaling parameter $K_0/K_\mu = 5.573$.
[b] Based on a scaling parameter $K_0/K_\mu = 2.058$.

(c) Table 4
Effect of alloying elements on the electronic and volumetric contributions of the isotropic shear modulus of γ-Fe (B=20.4×10[10] N/m², $\partial\mu/\partial P$=3.4)

Element	$1/a(\partial a/\partial x)$ in γ-Fe	$(\partial\mu/\partial x)_{electronic}$ in γ-Fe, ×10[10] N/m²	$(\partial\mu/\partial x)_{volumetric}$ in γ-Fe, ×10[10] N/m²	$(d\mu/dx)_{total}$ in γ-Fe, ×10[10] N/m²
Al	0.13089	−0.505[a]	−27.236	−27.741
Be	−0.10033	−30.421[a]	20.877	−9.544
C	0.21408	33.657	−44.546	−10.889
Co	−0.01014	−4.134	2.110	−2.024
Cr	−0.00577	−1.939	1.201	−0.738
Cu	0.00949	12.407[a]	−1.975	10.423
Ge	0.05767	−5.788[a]	−11.999	−17.787
Ir	0.07210	20.252[a]	−15.003	5.249
Mn	0.02673	2.887	−5.562	−2.675
Mo	0.08465	20.554	−17.614	2.940
N	0.18680	26.556	−38.869	−12.313
Nb	0.13762	19.395[a]	−28.636	−9.241
Ni	−0.01586	−9.349	3.300	−6.049
Pd	0.08635	9.260[b]	−17.968	−8.708
Pt	−0.18360	−46.909[c]	38.203	−8.706
Re	0.08939	24.793[a]	−18.600	6.193
Rh	−0.21718	14.731[a]	45.191	59.922
Ru	0.06567	15.897[a]	−13.665	2.232
Si	0.01525	−11.741	−3.173	−14.914
Ti	0.12639	15.130[d]	−26.299	−11.169
V	0.04220	11.131[d]	−8.781	2.350
W	0.09067	27.063[a]	−18.867	8.196

[a] Assuming $(\partial\mu/\partial x)^{\gamma\text{-Fe}}_{electronic} = (\partial\mu/\partial x)^{\alpha\text{-Fe}}_{electronic}$.
[b] Assuming $(d\mu/dx)_{total}$ is the same as Pt.
[c] Based on the single crystal data of *paramagnetic* $Fe_{72}Pt_{28}$ alloy [61].
[d] Our prediction in Fig. 10.

Figure 30: The coefficients for (a) athermal and (b) thermal frictional work model along with those for (c) isotropic shear modulus as developed by Ghosh and Olson [108] [112] [113].

Martensite fraction model:

In the Q&P processing, the quench temperature plays an important role in determining the final microstructural constituents and their phase fractions. As reported in several previous studies to be discussed in later sections, an optimum quench temperature helps maximize the retained austenite fraction. Therefore, accurate prediction of the final Q&P microstructure needs an accurate model for martensite fraction formed upon quenching of the austenite phase.

A comprehensive overview of the theoretical, empirical and semi-empirical models proposed over the years has been reported recently by Fei et al. [117]. Some of the most prominently used simple models to estimate martensite phase fraction upon quenching are listed below.

1. Koistinen and Marburger (KM) [118]:

$$f_{mar} = 1 - \exp[\alpha(Ms-T)] \;\; ; \alpha = -0.011$$

   where α is a material dependent constant obtained using measurements from four Fe-C alloys with 0.37 to 1.1 wt% carbon content. The Ms value used in the equation is slightly different from experimentally measured value due to the shape of the function.

2. Van Boheman and Sietsma [119]: The work involved experimental study on 19 different plain carbon and low alloy steels to determine a function for the parameter α in the KM equation mentioned above. The following expression was proposed

$$\alpha_{BS} = -0.0224 + 0.0107C + 0.0007Mn + 0.00005Ni + 0.00012Cr + 0.0001Mo$$

3. Lee and van Tyne[120]: The authors added an exponent, n, to the KM equation and described martensite fraction as:

$$f_{mar} = 1 - \exp\left[K_{LV}(Ms-T)^{n} \right]$$

where Ms is the actual martensite start temperature of the material and the two parameters are:

$$K_{LV}\ (K^{-1}) = -0.0231 + 0.0105C + 0.0017Ni - 0.0074Cr + 0.0193Mo$$

$$n = 1.4304 - 1.1836C + 0.7527C^2 - 0.0258Ni - 0.0739Cr + 0.3108Mo \text{ (in wt\%)}$$

4. Magee [121]: A more physical model for martensite fraction was derived theoretically for plate martensite, using the chemical driving force for transformation with the assumption of a uniform nucleation potency distribution.

$$f_{mar} = 1 - \exp[\ -\alpha * \Delta G\ ]$$

where ΔG is the excess driving force at any given quench temperature and is defined as the difference between the available chemical DF and critical DF at Ms.

5. Seo, Cho and Kooman [122]: These authors used the same equation as the original KM model with improved empirical composition dependent equations for the parameter α and Ms temperature.

$$f_{mar} = 1 - \exp[\ -\alpha * (Ms - T)]$$

$$\alpha = 0.0201 + 0.0844*C + 0.0013*Mn - 0.00057*Si - 0.0046*Cr - 4.7965*B$$

$$Ms(^oC) = 581 - 721*C - 36.5*Mn - 6.11*Si - 0.671*Cr + 0.006*B$$

with all compositions in weight percent.

6. Fei Huyan et al. [117]: Based on the derivations of Ms temperature using an empirical relationship of transformation critical driving force and alloying content[114] the authors fit an equation to martensite fraction as a function of the excess driving force for transformation below Ms temperature. The final form of the empirical relationship is:

$$f_{mar} = \frac{1}{1+A^{-1}(\Delta G)^{-B}}$$

where A is a constant equal to 0.05, ΔG is the excess driving force which is the difference of driving force at temperature T and Ms, and

$$B = 0.006*Ms - 0.1369 \quad ; \text{ Ms in kelvin}$$

The model is suggested to be applicable only when the steel is quenched to a certain temperature using water, brine or oil. Continuous fast cooling reportedly seemed to show less fraction of martensite compared to direct quenching.

In the current thesis work, the amount of martensite formed at different temperatures is predicted using the mechanisitic *Fe-martbain* model as implemented in the proprietary CMD (Computational Materials Dynamics) software platform developed by the SRG (Steel research Group) at Northwestern University and Questek Innovations LLC. The model is based on the heterogeneous martensite nucleation theory proposed by Olson and Cohen [13]. The nucleation of martensite occurs on the defects (stacks of dislocations) present in the material. The theory was extended with descriptions of the measured defect potency distributions in the austenite phase. The potency distribution of both pre-existing defects and autocatalytic defects are incorporated in the theory. Integrating over the activated defects, it is possible to calculate the athermal martensite fraction versus quench temperature. The athermal volume fraction of martensite is given by the equation:

$$f = (N_i + Pf - N_v)*(1-f)*V$$

where N_i: number of pre-existing nucleation sites in parent phase, P: autocatalytic nucleation sites per unit of martensite formed, N_v: number of particles formed per unit volume of alloy, V: average volume of martensite subunit. The individual potency distribution terms are described in the works of Lin, Olson and Cohen[123] and Ghosh and Olson[124].

2.3.2. Hardenability model

Hardenability is an important criterion for Q&P alloys to ensure that martensitic transformation is feasible for the given composition and other competing transformations are avoided for practically achievable industrial cooling rates. It is usually measured in terms of the critical cooling rate required to avoid any intermediary phases during quenching to undergo martensite transformation. Time-temperature-transformation (TTT) curves for any given alloy composition can help predict the critical cooling rate required to avoid ferrite or bainite transformation during quenching. In the current work, TTT curves are generated using the mechanistic *Fe-martbain* model based on the coupled diffusional/displacive theory of bainite transformation [33,34] as implemented in the proprietary CMD software developed by the SRG (Steel research Group) at Northwestern University and Questek Innovations LLC. The diffusion correction factor in the model was the only parameter calibrated to match experimentally determined TTT curves from Caballero et al. [125] and Behera et al. [126]. The value of D_corr=75 in the model was found to result in reasonable agreement of experimental values and predicted results as shown in Figure 31 and Figure 32. The effect of B and Ti addition to the alloy on hardenability has been recently quantified by the work of Song and De-Cooman [127] on bainitic transformation in low C steels. Figure 33 shows how B addition helps suppress the formation of polygonal ferrite at temperatures above 600^{o}C and delays bainitic transformation at temperatures below 600^{o}C. The effectiveness of B is enhanced by addition to titanium as it getters the Nitrogen dissolved, thus avoiding formation of BN.

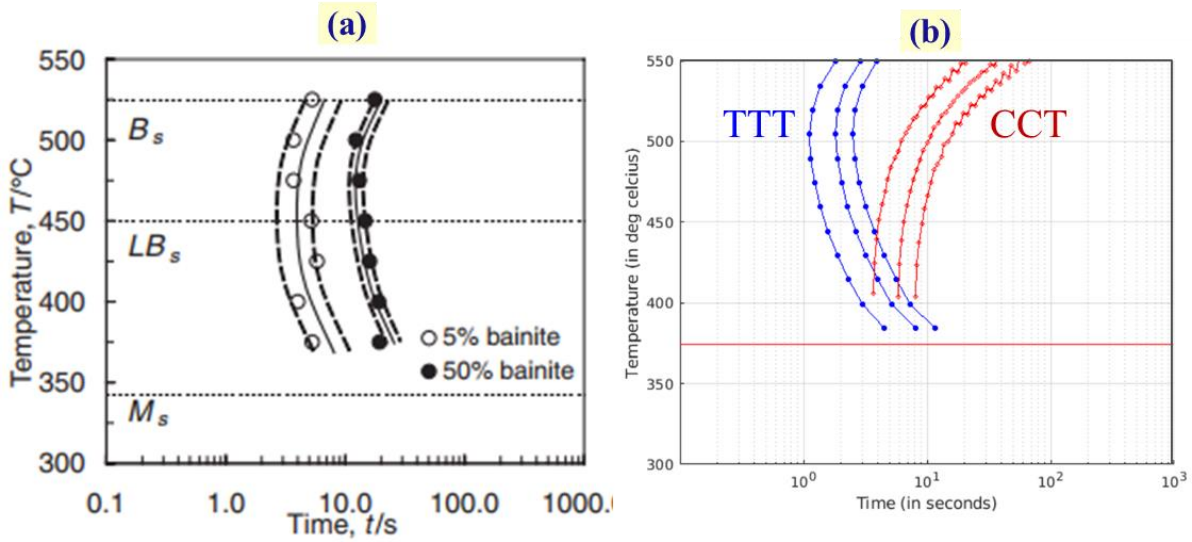

Figure 31: (a) Experimentally determined TTT curves [125] for alloy with composition 0.3C-1.22Mn-0.25Si-0.14Cr-0.1Ni-0.03Mo, (b) Fe-martbain predicted TTT & CCT curve (5pct, 50pct and 95pct transformation)

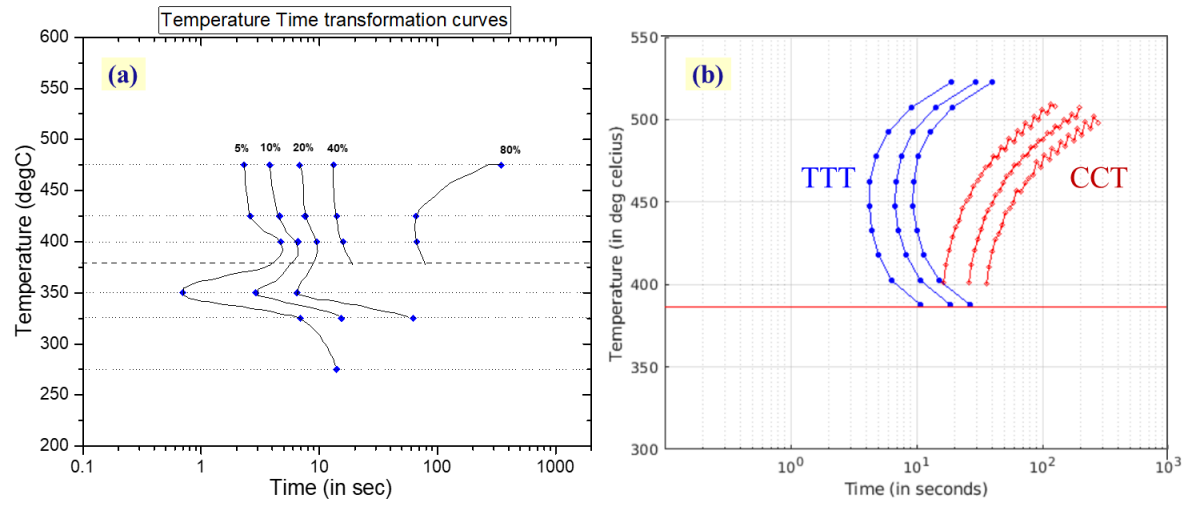

Figure 32: (a) Experimentally determined TTT curves [126] for alloy with composition 0.18C-1.95Mn-1.57Si-0.11Mo, (b) Fe-martbain predicted TTT & CCT curve (5pct, 50pct and 95pct transformation)

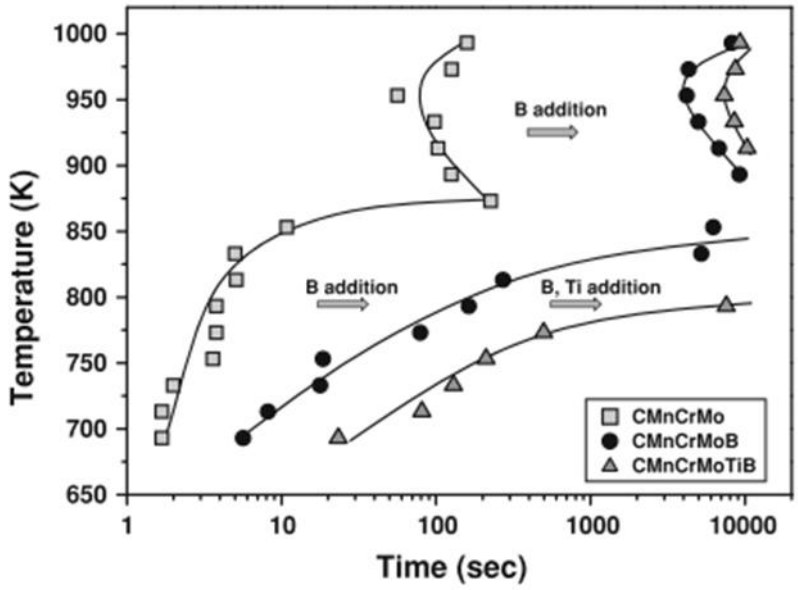

Figure 33: TTT diagram for 5 percent bainite transformation in CMnCrMo, CMNCrMoB and CMnCrMoTiB alloys (adapted from [127])

2.3.3. Carbon partitioning model

Numerous recent studies have provided experimental measurements of carbon partitioning from martensite to austenite [66,128,129] along with some modeling efforts to predict the carbon enrichment in austenite. One model for carbon partitioning is based on the concept of 'Constrained carbon equilibrium' suggested by Speer et. al [39,66]. The modeling criterion predicts austenite carbon content under the following assumed conditions: (i) equal carbon potential in austenite and martensite after complete partitioning, (ii) absence of other competing phase transformations i.e. carbide precipitation or bainite transformation, (iii) no movement of austenite/martensite interface during partitioning. However, recent studies with help of in-situ experiments have shown austenite martensite interfaces to be mobile in low and high carbon steels [59,130]. Interface migration in high manganese alloys has also been reported by measuring changes in austenite phase fraction with partitioning time [131]. These experimental observations necessitate the need of an improved modeling approach that allows for interface movement and considers competing phase transformations.

In the current proposed model, we use para-equilibrium simulations with an added temperature-dependent "effective stored energy" term to the BCC phase for predicting austenite carbon content. The para-equilibrium simulations performed using the ThermoCalc© software (with TCFE9 database) allow for movement of the FCC/BCC interface. The concept of stored energy has been previously applied in the case of bainitic transformation based on the theory of coupled displacive/diffusional transformations [33,34,132] and is added to the ferrite phase to better represent the net driving force available to form the product phase. The modeling approach has been previously successfully used to predict carbon enrichment in low alloy TRIP steels [29,30].

The present authors introduced the idea of an "effective stored energy" in the case of martensitic transformations for the first time in an earlier publication [133]. Based on the derivation of net critical driving force required for interface motion in the martensite nucleation theory[108,112], the effective stored energy term is realized to include stored elastic strain energy (G_{el}) along with the frictional work dissipated for interface movement against solid solution hardening (W_F^{SS}) and forest dislocations (W_F^D) as described in the equation below.

$$\text{'effective Stored Energy' or } G_R(\text{comp, T}) = G_{el} + W_F^D + W_F^{SS}$$

where G_{el} – elastic strain energy, W_F^{SS}- solid solution frictional work,

W_F^D -frictional work dissipated due to interface movement across forest dislocations

The work of Ghosh-Olson[108] on analyzing solid solution friction in steels concluded that solid solution hardening (W_F^{SS}) is athermal in nature for displacive interfacial motion above room temperature and can be predicted from elemental contributions. They evaluated the athermal strength of 14 alloying elements Al, C, Co, Cr, Cu, Mn, Mo, N, Nb, Ni, Si, Ti, V and W and derived the athermal strength coefficient (K_μ) for each solute. The interstitial solutes were determined to have stronger influence compared to substitutional solutes. In their later work, Ghosh-Olson derived the composition and temperature dependence of the isotropic shear modulus in multicomponent systems[134] and re-evaluated the athermal frictional work by considering scaling with the modulus[113]. The new equations for solid solution frictional work in terms of shear modulus are shown below:

$$W_F^{SS} = A_\mu * \mu(X_i) \qquad \ldots[113]$$

where μ is the shear modulus of austenite obtained from Ghosh et.al. [134]

$$\text{and, } A_\mu = \sqrt{\sum_i \left(K_\mu^i \, X_i^{0.5}\right)^2} + \sqrt{\sum_j \left(K_\mu^i \, X_j^{0.5}\right)^2} + K_\mu^{Co} \, X_{Co}^{0.5}$$

where i=Al, C, N, Cr, Mn, Mo, Nb, Si, Ti, V, W and j= Cu, Ni

Research work on nonthermoelastic-thermoelastic transition of martensitic transformation with ordering in the Fe_3Pt system[135,136] showed the important contribution of frictional work due to forest dislocation hardening to the net driving force for interface motion. The drastic reduction of critical driving force for transformation with elimination of accommodation slip by order strengthening indicated a negligible contribution of G_{el} compared to W_F^D. The dependence of W_F^D on dislocation density has been quantified in the work of Ghosh-Olson[112] by studying the effect of pre-strain on the rate of isothermal martensitic transformation at cryogenic temperatures. The effect of pre-straining was shown to be consistent with dislocation forest hardening acting as an athermal back stress inhibiting interfacial motion. This dependence of critical driving force for displacive transformations on dislocation density was reported to explain the reason for the observed temperature dependence of critical driving force in the case of bainitic transformations[137,138]. The temperature dependence of dislocation density due to dynamic recovery at high enough annealing temperatures accounts for this temperature dependence of critical driving force. Linear temperature dependence of bainite critical driving force was first reported by Bhadeshia et. al.[139–141] and a mechanistic explanation for it could then be provided with the understanding of dynamic recovery of generated forest dislocations. In the current work on understanding interfacial motion during the partition step in terms of coupled diffusional/displacive transformations, we focus on the form of W_F^D as a function of transformation temperature that accounts for the measured austenite phase composition under para-equilibrium constraint.

Figure 34(a) shows the effect of stored energy addition to the BCC phase on the para-equilibrium carbon content of austenite. Addition of stored energy moves the free energy curve for BCC phase upwards and thus lowers the equilibrium carbon content of the austenite phase as determined by tangent construction. These values are now much closer to the experimental measurements of austenite carbon content. The addition of effective stored energy is also dependent on the direction of interface motion. The dissipation contribution to this stored energy is always added to the product phase. In the case of QTs where the starting austenite fraction after quenching is higher than final austenite fraction, the interface moves towards FCC, thus creating the product BCC phase. Thus, effective stored energy is added to BCC. On the other hand, for QT far below Ms temperature, the starting austenite fraction could be smaller than the final RA fraction. In such cases, the interface moves towards BCC phase creating new FCC product phases. The dissipated energy in such cases would be added to the FCC phase as shown in Figure 34(b). The addition of SE in this case increases the para-equilibrium austenite carbon content.

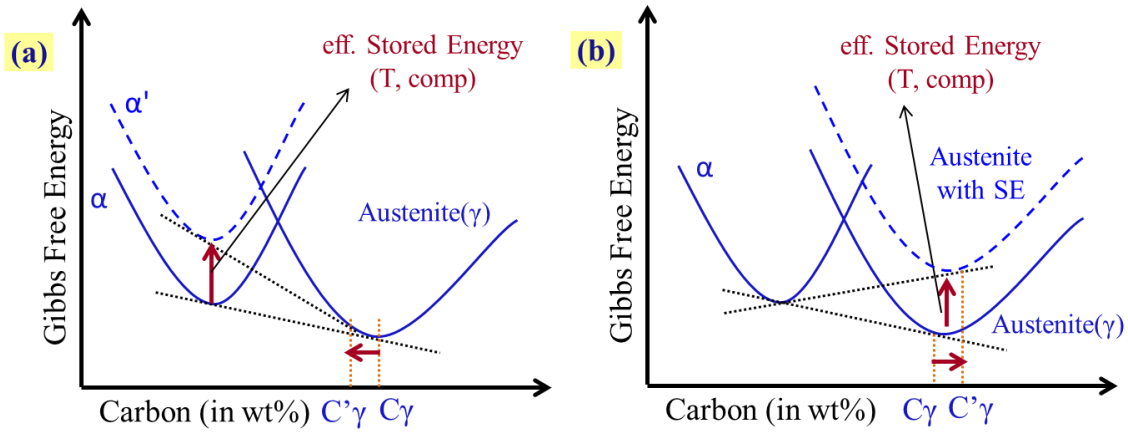

Figure 34: (a) Schematic showing effect of stored and dissipated energy on para-equilibrium carbon content of austenite when added to (a) BCC phase, (b) FCC phase

ThermoCalc macro codes were coded in the MATLAB software with inputs from the effective stored energy model also created in MATLAB. The inputs to the macro code included the alloy composition, partitioning temperature and effective stored energy value. The output from the simulations were the austenite carbon content and the para-equilibrium austenite phase fraction assuming no carbide precipitation.

Para-equilibrium simulations were carried out in DICTRA [142] to model the composition profile as a function of partition time. The macro codes written for the PE calculations used older unencrypted TC databases (SSOL2) as the current software version doesn't allow energy addition to individual phases in the latest databases while performing PE calculations. The stored energy values were adjusted for the different database with a fixed temperature independent addition (~20 J/mol). Figure 35 shows the carbon profile at different P-times for Steel 1 (0.2C-2.2Mn-1.5Si) at PT of 400^{o}C. The calculation started with an 0.4μm austenite region next to a 0.2μm ferrite region. The composition in both regions was the same as alloy composition except carbon which was reduced to 0.1 wt%. Mass balance calculations using measured austenite fraction and carbon content estimated about 50% of the alloy carbon lost in the form of carbides. Therefore, the alloy carbon content used in the simulations was modified to match experimental phase fraction measurements. The simulations would fail to find equilibrium at these temperature ranges without the addition of effective stored energy to the ferrite phase.

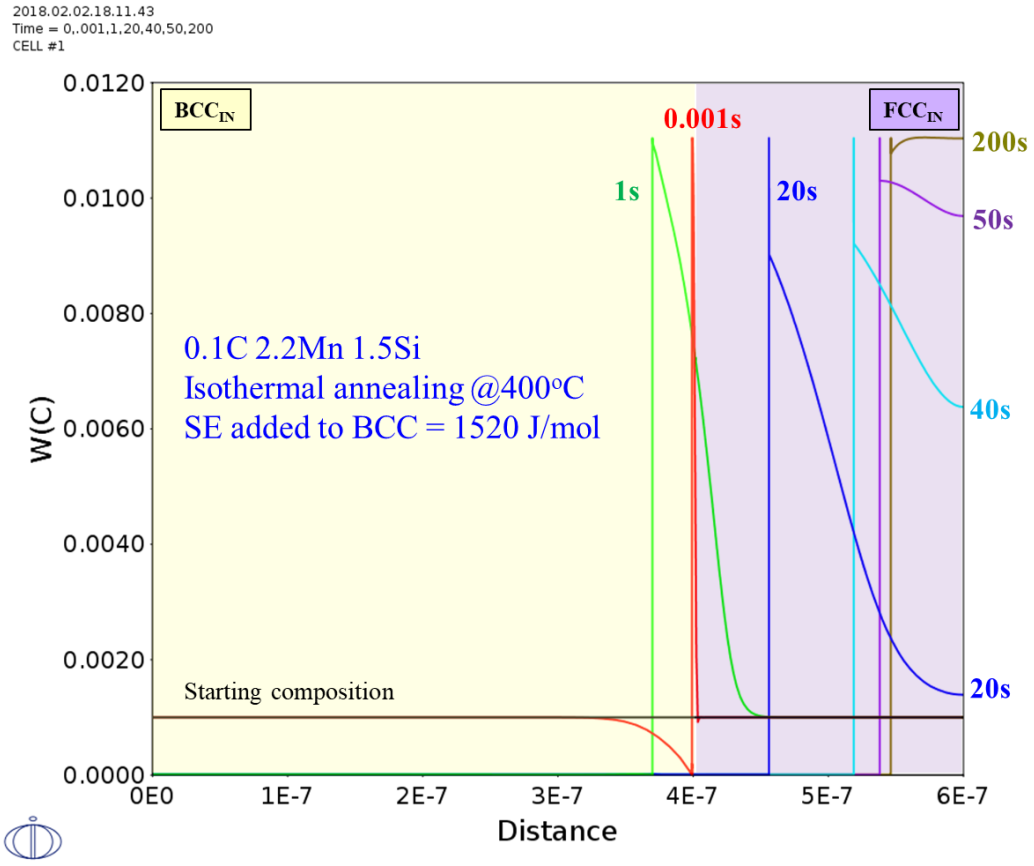

Figure 35: DICTRA simulation (with added effective stored energy) results showing carbon profile at different times upon isothermal annealing at 400°C

2.3.4. Austenite stability model

The carbon partitioning model outputs the austenite carbon content which is the most crucial parameter impacting retained austenite stability. The austenite carbon content influences martensitic transformation and thus final properties via the transformation induced plasticity effect. A complete understanding of the processing/property relationship requires understanding of the influence of process parameters on austenite stability and the effect of change in stability on the final mechanical properties. Accurate prediction of mechanical properties needs a reliable model to predict austenite stability. Previous research efforts have confirmed austenite stability

to be dependent on various microstructural features such as (i) chemical composition, especially its carbon content[20], (ii) size of austenite blocks/films[21,25,75], (iii) austenite morphology[22,75], (iv) crystallographic orientation[20,75,143] (v) constraining effect of neighboring phases[25,144,145] and others. Higher carbon in austenite improves its thermal and mechanical stability against martensite transformation by lowering its transformation temperatures. Thin films of inter-lath austenite are reported to be more stable compared to the blocky type. Thus, lamellar morphology of austenite is preferred over equiaxed morphology. The presence of harder phases such as fresh martensite surrounding austenite is reported to have a detrimental effect on its stability. The current work evaluates the influence of austenite composition and size on its stability supporting a predictive and quantitative model for austenite stability.

Accurate prediction of austenite stability is crucial as an optimal stability is required for maximizing the benefits from TRIP effects to the final ductility of the alloy. The transformation of stable retained austenite to martensite at the appropriate time during mechanical loading will delay necking the most and thus improve uniform elongation. This corresponds to the so-called transformation induced plasticity (TRIP) effect. Constitutive mechanical behavior models for transformation plasticity have been earlier developed taking into account the kinetics of deformation induced martensitic transformations[7,17]. Mechanical deformation can contribute to the kinetics of martensitic transformation by adding to the thermodynamic driving force due to applied stress or by the formation of additional nucleation sites due to plastic strain. These represent the two modes of deformation induced martensitic transformations i.e. stress-induced and strain-induced transformation. Figure 5(b) plots the observed yield stress of a material at

different testing temperatures operating under the two deformation modes. The temperature at point of intersection for the two modes is termed the Ms^{σ} temperature. It is the temperature at which the material can withstand the maximum applied stress before yielding occurs. At temperatures below Ms^{σ}, the material yields due to martensitic transformation of retained austenite while at temperatures above Ms^{σ}, yielding occurs due to slip deformation. M_d is the temperature beyond which martensitic transformation cannot be triggered with help of mechanical deformation. The influence of temperature on the TRIP effect and its effect on delaying necking in case of high strength TRIP steels has been earlier explained by Olson et. al [7,11]. Recent work by Wang et. al. [146] measured the peak ductility temperature and Ms-sigma temperature for an intercritical annealed QP980 steel. Thermodynamic modeling for the Ms^{σ} temperature can be utilized to predict the peak ductility temperature, enabling design to place it at the material application temperature. Thermodynamic models for Ms^{σ} temperature have been previously developed for high strength TRIP steels[27,147] and been used to improve fracture ductility in the case of bainitic steels[29,30].

Ms^{σ} temperature has been established as a quantitative measure of the retained austenite stability. It is especially useful as it can be theoretically calculated using thermodynamic models and experimentally measured with tensile test experiments. According to the Olson-Cohen model [13], when the temperature is at Ms^{σ} temperature and stress applied is at the yield stress for slip, the sum of chemical driving force and mechanical driving force for transformation equals the critical driving force required for martensitic transformation. This is described in the equation stated below. Using established descriptions and those developed in current work for the free

energy terms as a function of temperature and composition, the Ms^{σ} temperature for any austenite composition and size can be calculated.

$$\Delta G_{Chem} + \Delta G_{Mech} = \Delta G_{Crit} \qquad \text{at } T=Ms^{\sigma} \text{ and } \sigma=YS_{slip}$$

The chemical driving force (G_{Chem}) for transformation is calculated using the ThermoCalc© software with a proprietary database (developed from the kMART database[113]) suited specifically for low-temperature martensite transformation calculations. G_{Chem} is defined as a function of the chemical composition and temperature i.e. $\Delta G_{Chem} = F(X_i, T)$, *where i=C, Mn, Si and other alloying elements.* The chemical driving force for martensitic transformation is the difference between the free energy of the BCC and FCC phases.

$$\Delta G_{Chem} = G_{BCC} - G_{FCC}$$

The mechanical driving force considers the effect of applied stress on the orientation distribution of the existing nucleation sites. It is stress state dependent due to the interaction of applied stress with the transformation volume change. The relation of ΔG_{Mech} to the applied stress is given by the equation below [29,30] which was developed from the work of Patel and Cohen [148] followed by the work of Olson-Tsuzaki-Cohen [149]. The parameter $(\frac{\partial \Delta G_{Mech}}{\partial \sigma})$ in the equation is a function of the stress state as stated by Patel and Cohen[148].

$$\Delta G_{Mech} = \sigma(\frac{\partial \Delta G_{Mech}}{\partial \sigma}) = -0.718\sigma - 6.85(\frac{\Delta V}{V})\sigma_H + 185.3(1-\exp(-0.003043*\sigma)) \text{ in J/mol}$$

where σ_H, hydrostatic stress state = $\sigma/3$, for uniaxial tension; σ = von Misses equivalent stress,

fractional volume change upon transformation, $\frac{\Delta V}{V} = 0.04$

The critical driving force is accounted as the sum of the nucleation defect potency (G_n) and the frictional work of interfacial motion due to solid solution hardening (W_F^{SS}) and forest

dislocations (W_F^D) as described below. The nucleation defect potency has contributions from the transformation elastic strain energy (G_{el}) and interfacial energy due to newly formed interfaces described by the (***2γ/nd***) term, where γ is the specific fault/matrix interfacial energy, *n* is the defect potency (size) and *d* is the close-packed interplanar spacing. The solid solution frictional work of interfacial motion during martensite nucleation (W_F^{SS}) described by the equation below is a function of the chemical composition of retained austenite and has an athermal and thermal component as quantified in the work of Ghosh and Olson [108,112,113]. The frictional work due to forest dislocations (W_F^D) is derived as a function of partitioning temperature by calibrating the model with experimentally measured values of Ms^{σ} temperature.

$$\Delta G_{Crit} = -G_n - W_F^D - W_F^{SS}$$

where $G_n = G_{el} + \frac{2\gamma}{nd}$, and $W_F^{SS} = W_F^{SS}{}_{athermal} + W_F^{SS}{}_{thermal}$, as described section 3.1

In the stress assisted regime, yield stress at different testing temperatures can be calculated upon equating the sum of chemical and mechanical driving force to the critical driving force for martensitic transformation. The final form of transformation yield stress in the stress-assisted regime is described below. The slip yield stress variation with temperature in the strain-induced regime is measured experimentally via multiple specimen tensile test experiments. The intersection of the yield stress plots in the two regimes gives the Ms^{σ} temperature as shown in Figure 5(b).

$$\text{Transformation stress } (\sigma_t) = \left(1 \Big/ \frac{d\Delta G}{d\sigma} \right) \left(-\frac{2\gamma}{nd} - \Delta G_{Chem} - G_{el} - W_F \right);$$

$$\text{where } n = -\frac{1}{\alpha} \ln\left[-\frac{\ln(1-f)}{N_v^o V_p} \right] \text{ ; for annealed austenite}$$

f – detectable fraction transformed; N_V^o - total number of nucleation sites of all potencies,

V_p - austenite particle volume, α is a constant and, $W_F = W_F^D + W_F^{SS}$

The austenite particle size (or thickness) influences the defect potency as shown in the equation above and thus affects the austenite stability. For a fixed quench temperature, the value of defect potency, *n*, is constant.

Chapter 3. Influence of Q&P processing on microstructure and properties

The key to achieve the best performance out of Q&P alloys is to understand and control the influence of processing parameters on the microstructure which directly affects the mechanical properties of the material. The key processing parameters i.e. the quench temperature (QT), partition temperature (PT) and partition time (P-time) are known to have significant effect on the final alloy performance. New results on the role of these parameters on the final Q&P microstructure, individual phase stability and mechanical properties is discussed in the following sections. The variation in observations due to other parameters such as starting microstructure, heating/cooling rate, austenitization temperature etc. have been kept to minimum by ensuring similar conditions for them throughout the current work.

3.1. Partition temperature (PT)

The role of partition temperature on the different microstructural characteristics of Q&P alloys was analyzed by studying samples of Steel 1 (0.2C-2.2Mn-1.5Si-0.2Cr, Ms=354^{o}C) processed to Q&P cycles with different PT. The samples were initially fully austenitized at 900^{o}C (above the Ac3 temperature) for 100secs and quenched to 270^{o}C (quench temperature, QT) before being reheated to three different partitioning temperatures, PT (390^{o}C, 410^{o}C, 430^{o}C) for partitioning times of 75, 100 and 150sec respectively. The heat cycles are shown in Figure 36. The samples are designated as PT430, PT_410, PT_390 based on their partition temperatures. The isothermal partition times were chosen based on DICTRA simulations to ensure homogenization of carbon in austenite of typical 0.2μm thickness (as observed in electron microscopy) and to avoid unnecessary carbide precipitation upon continued isothermal annealing. The results from some of these simulations are shown in Section 3.2.2.

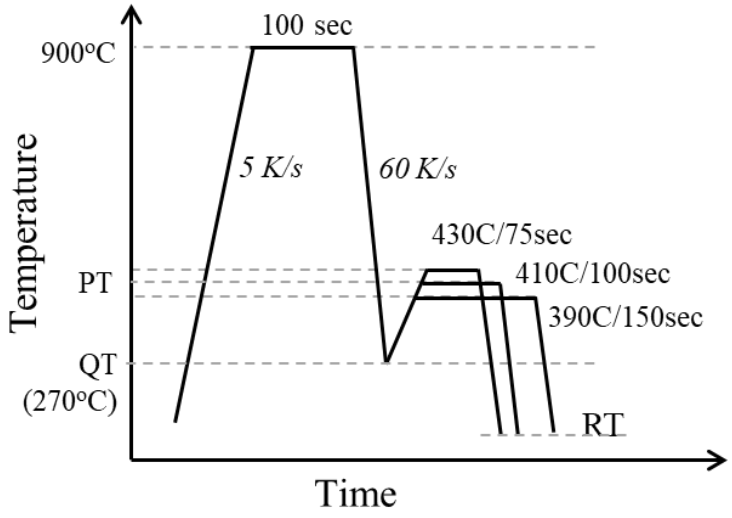

Figure 36: Schematic of the Q&P processing cycles with varying PT/Ptime for Steel 1

3.1.1. Effect on microstructure and mechanical properties

The microstructure post heat treatment was studied using electron microscopy for the three different QP cycles. In all three cases, the microstructure consisted of primarily lath martensite with some fraction of retained austenite. Figure 37(a-c) shows the nital etched SEM micrographs for all three conditions consisting of the martensite matrix with fine films/blocks of retained austenite. No intercritical ferrite phase was seen confirming full austenitization at the start in all cases. The bright field mode TEM micrographs shown in Figure 38(a-c) show the presence of fine films of interlath austenite along with some blocky units. Further investigations into the distribution of phases and their crystallographic orientation was carried out using EBSD analysis for one processing condition, PT_410. Figure 39(a) shows the secondary electron image of the region investigated using EBSD. Figure 39(b) is the orientation-imaging microscopy (OIM) color map for the martensite phase superimposed on the band contrast image. The martensite laths are arranged in the form of blocks and packets inside the prior austenite grains. Figure 39(c)

shows the OIM color map for the austenite phase superimposed on the band contrast image. The retained austenite is found to be in the form of fine interlath films inside the grains and in form of blocks close to the grain boundaries. A majority of the interlath films are not easily identifiable with EBSD due to resolution limits and boundary effects. The retained austenite inside the same large prior austenite grain have similar crystallographic orientation. The blocky austenite has an average thickness of 0.5–0.8μm. The fine interlath films have thickness about 50-100nm as seen in the OIM maps and the TEM micrographs. Similar size scale and distribution of austenite phase have been earlier reported for QP steels using EBSD [75,150] and TEM studies[72,151].

The room temperature mechanical properties of the three samples were measured using tensile tests and are listed in Table 9. The engineering stress strain plots are shown in Figure 40(a). The true stress σ and work hardening (WH) rate dσ/dε are plotted against true strain in Figure 40(b). Higher tensile strength and elongation values are observed for the highest partition temperature sample (PT_430). At low strain levels, the work hardening behavior for all the samples seems similar while after about 2% true strain the WH rate for the PT_430 sample curves upwards and remain stable until much higher strain levels compared to other samples. Similar behavior is seen for the PT_410 sample but the higher strain hardening is maintained to a smaller overall strain value. This curvature is expected from the TRIP effect of the retained austenite that eventually results in the different values for uniform elongation. The austenite in the PT_430 sample appears to have the least stability among the three PTs but is likely to be the closest to optimal stability for maximizing ductility. Similar values of YS, UTS and dependence on PT have been reported for the same alloy composition by Arlazarov et.al.[152]

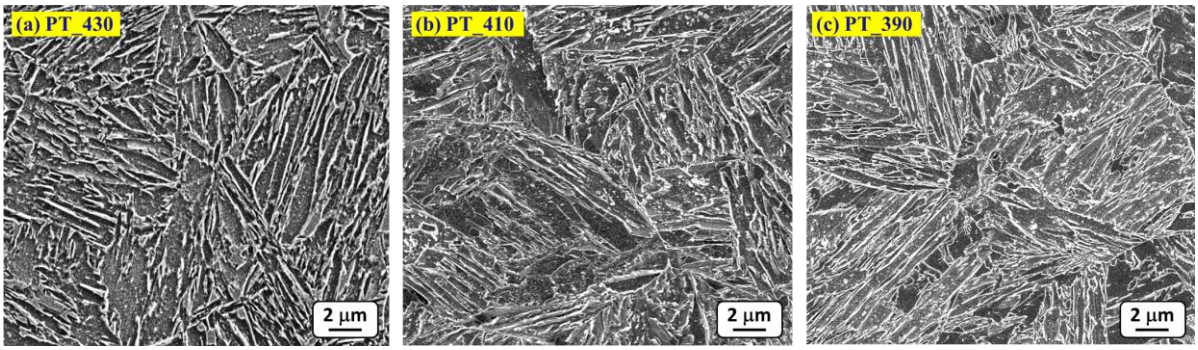

Figure 37: SEM micrographs after nital etching showing the martensite/austenite microstructure in the case of Steel 1 with QT of 270ºC and PT/Ptime of (a) 430ºC for 75s (b) 410ºC for 100s and (c) 390ºC for 150s

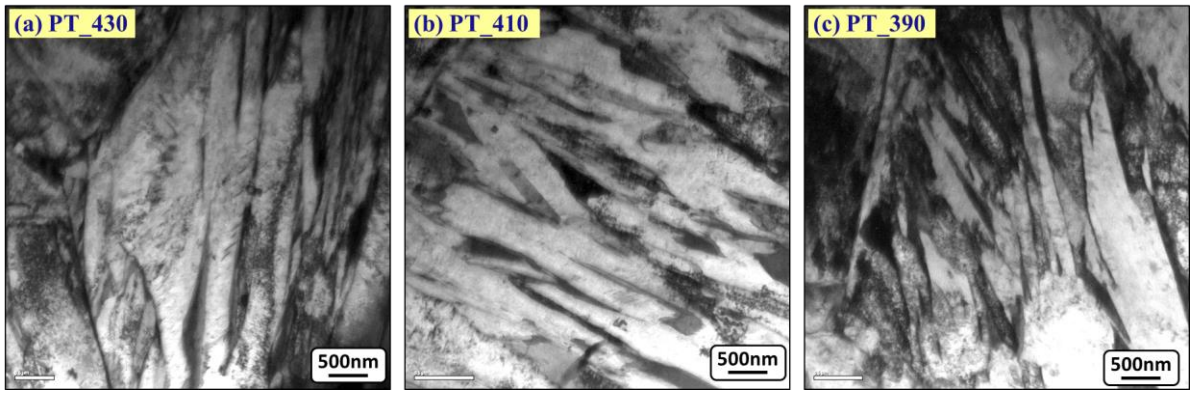

Figure 38: TEM micrographs showing the retained austenite in form of films and blocks in the case of Steel 1 with QT of 270ºC and PT/Ptime of
(a) 430ºC for 75s (b) 410ºC for 100s and (c) 390ºC for 150s

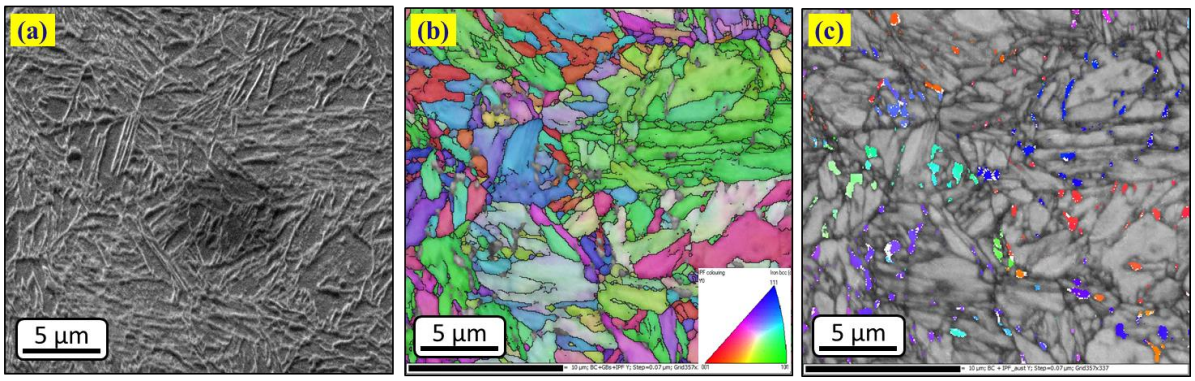

Figure 39: EBSD analysis for a Steel 1 sample with QT270_PT410_100s.
(a) SEM image of the investigated region. Orientation-imaging microscopy (OIM) color maps for the (b) martensite phase and (c) austenite phase superimposed on band contrast image

Table 9: Room temperature mechanical properties of the Q&P processed Steel 1 samples. (*n* – defect potency size)

QT	PT	RA fraction	YS	UTS	UE	TE	Ms^{σ}	***n***
°C	°C	(%)	MPa	MPa	%	%	°C	
270	430	8.2	1237	1380	9.3	14	100	8.04
270	410	6.9	1168	1358	7.7	13	40	7.64
270	390	7.2	1190	1336	4.4	9	-30	7.38

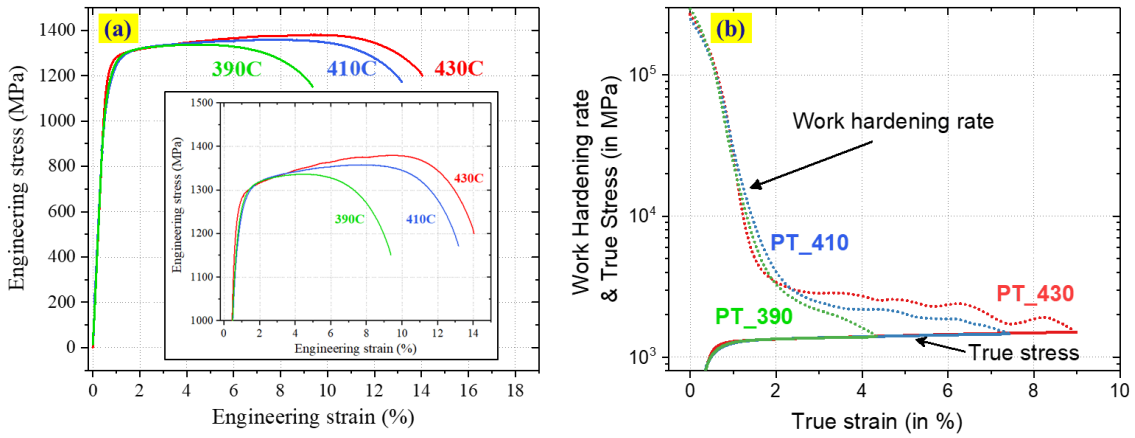

Figure 40 (a)Engineering stress-strain plots with higher magnification inset, (b) True stress and work hardening rate plotted against true strain for the three different Q&P processed samples of Steel 1

3.1.2. Effect on carbon partitioning

The individual phase fraction and austenite carbon content for the different Q&P processed samples are listed in Table 10. The retained austenite fraction was measured using high energy x-ray diffraction (HEXRD). The intensity versus two-theta angle plot shown in Figure 41(a) contains 4 peaks each for the austenite and martensite phases. The carbon in austenite was estimated by averaging lattice parameter measurement from the four different peaks and using the empirical equation described earlier. The signal to noise ratio for the observed austenite peaks was quite large ensuring accurate measurements of lattice parameter and phase fraction.

HEXRD scans with longer dwell time were also performed around cementite intensity peaks to identify carbide precipitation as shown in Figure 41(b). Lower partition temperature, PT_390 samples showed a faint broad peak for cementite. The small size of carbides in these alloys and their low phase fraction makes it quite difficult to detect them with bulk diffraction experiments. 3D-LEAP experiments were also carried out to accurately determine the austenite carbon content in these alloys. The complete tip reconstructions and composition proximity histograms across the martensite/austenite interface are shown in Figure 42. The tip reconstructions shown contain only carbon atoms (red dots) and manganese atoms (blue dots). Austenite can be seen to be clearly enriched in carbon with some carbides forming in the martensite phase. Proximity histograms shown alongside in Figure 41 provide evidence for clear enrichment of carbon in the austenite phase with no long-range diffusion of substitutional alloying elements. The measured values from both 3DAP and HEXRD experiments noted in Table 10 confirm higher carbon partitioning at lower partition temperatures. Austenite phase fraction was identified to be critically dependent on the amount of carbide precipitation. Higher amount of carbides reduced the austenite phase fraction as seen in Table 10.

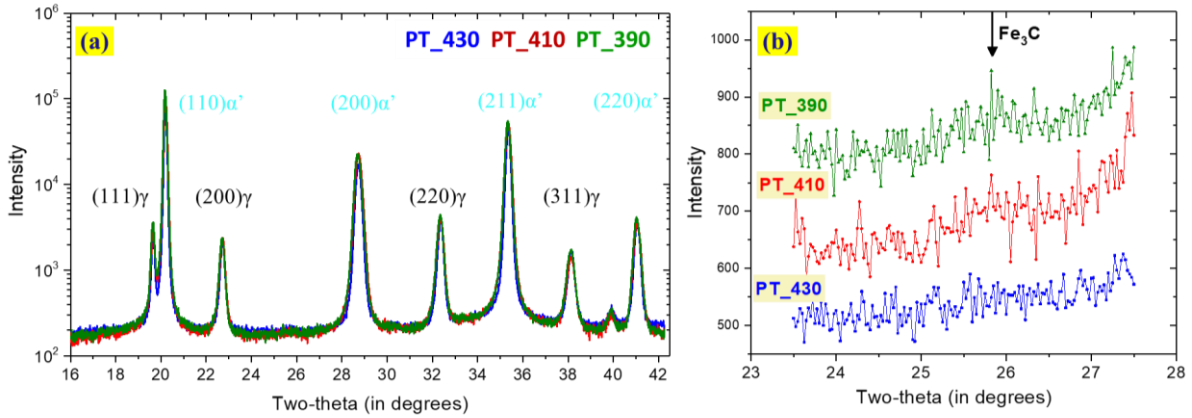

Figure 41: (a) Intensity vs two-theta angle from HEXRD experiments for Q&P samples with three different PTs, (b) longer dwell time scans around expected cementite peaks

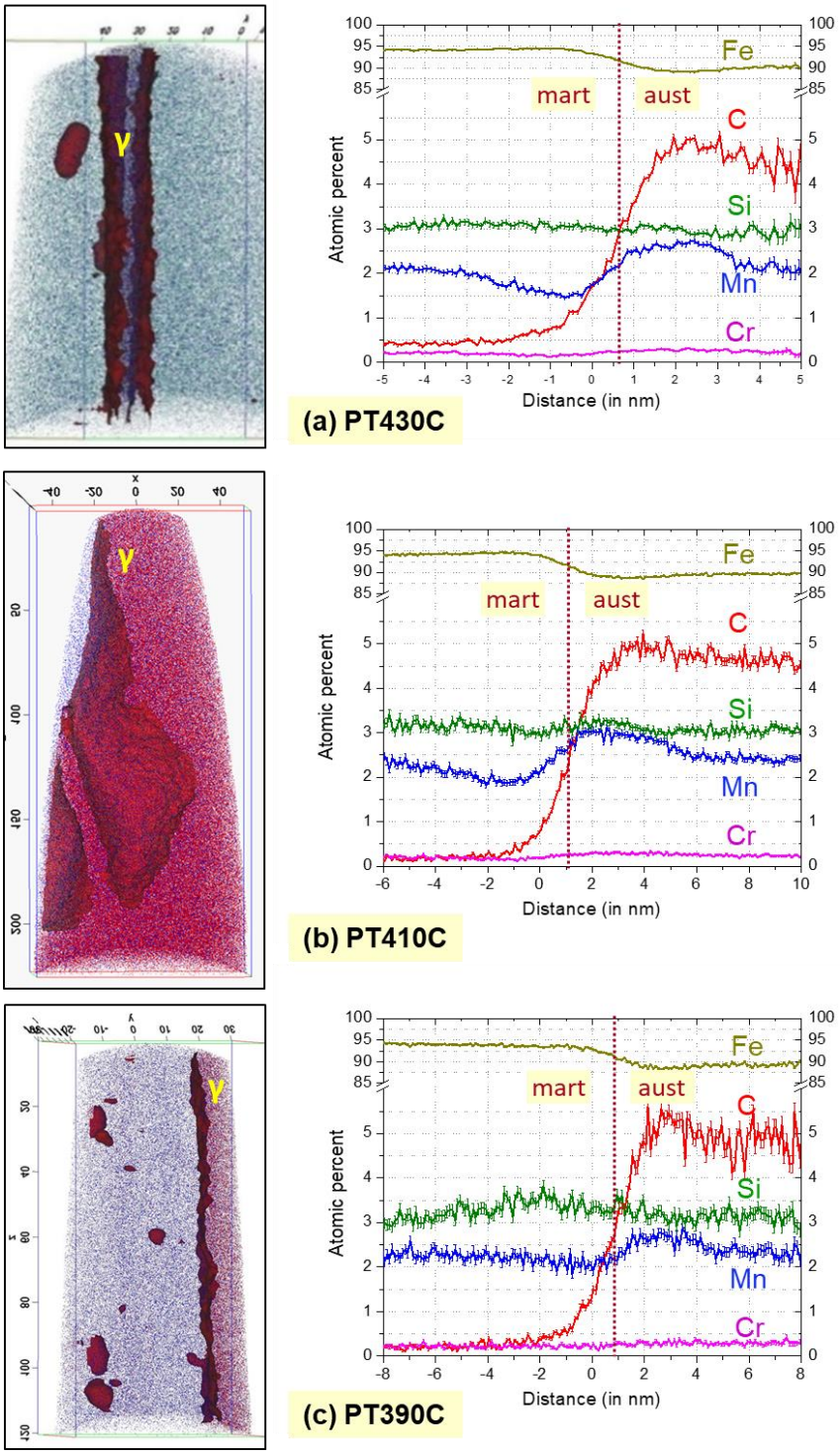

Figure 42: 3DAP tip reconstructions showing austenite/martensite interfaces along with composition proximity histograms across those interfaces in case of Steel 1 with QT of 270^{o}C and PT/Ptime of (a) 430^{o}C for 75s (b) 410^{o}C for 100s and (c) 390^{o}C for 150s

The phase transformations occurring during the Q&P cycle were analyzed using dilatometer experiments that accurately measure change in length of the sample as a function of temperature and time as shown in Figure 43. The overall variation of temperature and change in length versus time is plotted in Figure 43(a). A decrease in sample length is observed upon reaching close to Ac3 temperature during initial heating associated with BCC to FCC transformation. The transformation in some cases continues during the isothermal hold above Ac3 temperature with the curve eventually flattening upon complete austenitization. Figure 43(b) shows the quenching section followed by the reheating step from QT to PT. The sharp increase in length just before reaching QT is due to onset of martensite transformation. The change in length during reheating is due to thermal expansion and FCC to BCC transformation in the remaining austenite. Figure 43(c) zooms in on the partitioning step where the change in length is associated with the continued FCC-BCC transformation, carbon partitioning to austenite and possible carbide precipitation. Formation of BCC phases and carbon partitioning to austenite are expected to cause an increase in length while carbide precipitation should result in a decrease of sample length [153]. The curve can be seen to flatten faster for higher partition temperatures as carbon partitioning and any transformation of austenite is faster at higher temperatures. The observation also validates the choice of different partition time for each partition temperature to complete partitioning but prevent unnecessary excess carbide precipitation. A section of the change in length versus temperature focusing on the quenching and partitioning step is plotted in Figure 43(d). The abrupt increase in length close to alloy Ms temperature (~355^{o}C) is due to onset of martensitic transformation. The increase in length during isothermal holding at the different PT is associated with carbon partitioning during partial transformation of the retained austenite. The

increase in length during isothermal holding can be seen to be systematically higher for lower partitioning temperatures. This is consistent with higher carbon partitioning at lower partitioning temperature for their respective partition times.

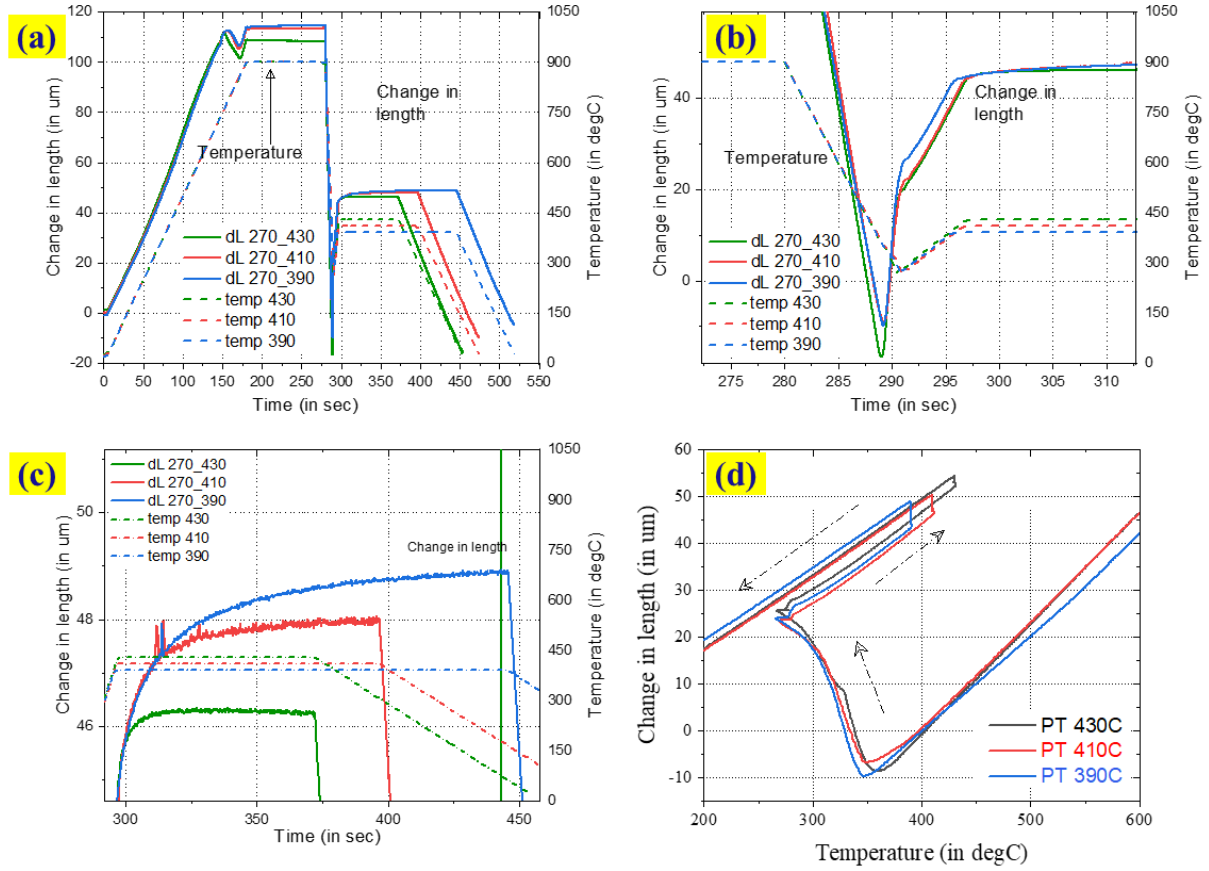

Figure 43: (a) Plot of temperature and change in length versus time for the three different Q&P cycles applied to Steel 1 using a dilatometer. Magnified section of the plot is shown in figure (b) and (c) focusing on the quenching and partitioning step respectively. (d) Change in length vs temperature during the Q&P cycles

As discussed earlier, para-equilibrium simulations with an added temperature-dependent effective stored energy term are used in the current work to model the austenite carbon content. The effective stored energy values at each PT have been calculated using the measured austenite carbon content and are tabulated in Table 10. After subtracting the composition-dependent solid

solution frictional work (W_F^{SS}) contribution to stored energy, the value of frictional work due to forest dislocations, W_F^D can be calculated for each partition temperature. The dependence of W_F^D on PT attributed to dislocation recovery is then fitted to a linear function i.e. W_F^D = -6.25*PT + 3403 J/mol, where PT is in degree Celsius. W_F^D is assumed to be just dependent on the partition temperature and not on the alloy composition. The measured carbon in austenite using 3DAPT and HEXRD experiments are plotted in Figure 44. The plot includes an additional data point from a previous study on the same alloy at a PT of 450ºC [154]. Consistent with the underlying chemical thermodynamics, at lower partitioning temperatures there is more partitioning of carbon into the austenite phase, despite the higher stored energy The measured values from HEXRD and 3DAPT agree well with each other. The predicted values using the PE model with and without the added stored energy model are plotted as dashed lines. The predicted values without stored energy addition are significantly higher than experimental measurements as has been commonly reported by others [128]. The stored energy addition results in a quite accurate prediction of austenite carbon content as a function of partitioning temperature. The austenite carbon content and measurements for average carbon trapped in the martensite (~0.04wt%) from the 3DAP analysis can then be used to back-calculate the amount of alloy carbon lost to carbides. The values noted in Table 10 show that a significant fraction (40-50%) of alloy carbon is lost in the form of carbides despite significant Si alloying additions. Elimination of carbides could result in almost double the amount of austenite (~16%) in the microstructure.

Table 10: Phase characteristics after respective QP cycles

QT °C	PT °C	Ret. Aust (HEXRD) %	Cγ in wt%		eff. SE J/mol	W_F^D(PT) J/mol	wt% C lost to carbides
			(HEXRD)	(3DAP)			
270	430	8.2	1.00 ± 0.03	1.03 ± 0.05	1305	719	0.081
270	410	6.9	1.05 ± 0.03	1.05 ± 0.03	1440	834	0.090
270	390	7.2	1.10 ± 0.03	1.09 ± 0.05	1575	969	0.084

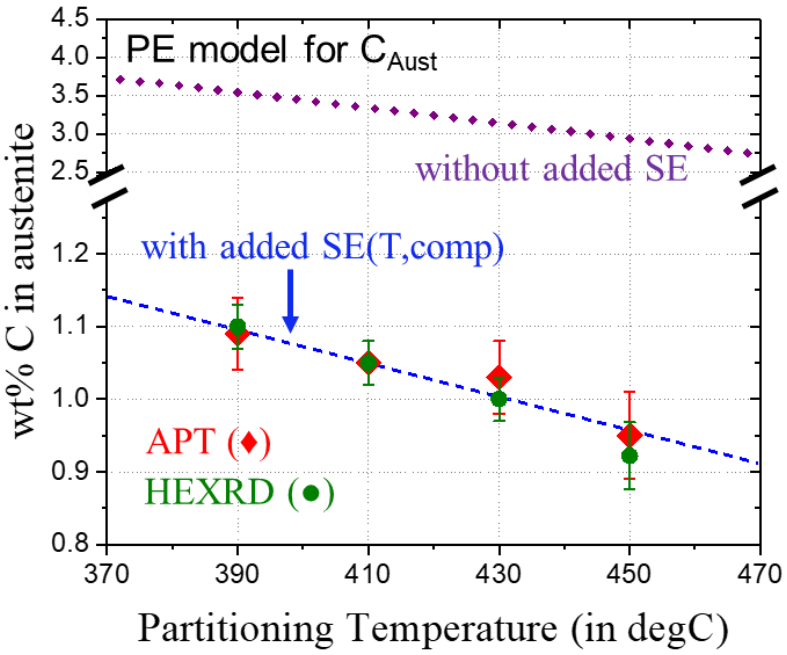

Figure 44: Austenite carbon content vs partitioning temperature. Dotted lines are for predicted values using PE model with and without addition of effective Stored energy

3.1.3. Effect on Retained Austenite stability

Experimental measurements of Ms^{σ} temperature via single-specimen Bolling-Richman tests were carried out as described earlier in Section 2.2.3. The upper yield stress values measured for the interrupted tensile tests at different testing temperatures are plotted in Figure 45 for the three different partitioning temperature samples. The individual interrupted engineering stress-strain plots with increasing testing temperature from left to right are shown as insets. The maxima in the yield stress plots correspond to the Ms^{σ} temperature and are determined by the intersection point of best fit lines on either side of the maxima. The results confirm that Ms^{σ} temperature decreases with decrease in partitioning temperature consistent with higher carbon partitioning. Using the W_F^D values defined by Figure 44, the experimental measurements can be used to calculate the defect potency term in the critical driving force description of the austenite stability model. The Ms^{σ} temperature along with the corresponding defect potency (n) values are tabulated in Table 9. As expected, the calculated defect potency values are much smaller than that typical value (n=13) found for martensite transformation from single phase austenite. The more potent nucleation sites are used up in the transformation during initial quenching step thereby decreasing the defect potency value. The variation of defect potency with partition temperature is small and results in small variation of the austenite stability.

In addition to single specimen Bolling-Richman tests, individual tensile specimens of PT_410 material were tested at different temperatures. The measured values of YS, TS, UE and TE versus testing temperature are plotted together in Figure 46(a). The actual engineering stress-strain plots at different temperatures are shown alongside in Figure 46(b). The evident Ms^{σ} temperature is quite similar to that estimated from the single-specimen tests. The uniform

ductility is also seen to vary with test temperature with a broad maximum below the Ms^{σ} temperature. This is unlike the behavior seen in the case of low carbon TRIP steels[30] or inter-critically annealed QP steels [146] where the ductility is typically maximum about 20^{o}C above the Ms^{σ} temperature. One explanation for such behavior could be a bimodal austenite stability in these fully austenitized Q&P alloys associated with the two morphologies (blocky and film-type) of retained austenite. Yielding behavior will be controlled by the lowest stability austenite, while uniform ductility could reflect the higher stability component. Similar observations were made in other tested alloys and are elaborated further in section 4.2. The strain hardening rate $d\sigma/d\varepsilon$ and true stress values at different temperatures are plotted against true strain for the same PT_410 sample in Figure 46(c). Decrease in test temperature clearly improves the strain hardening behavior at higher plastic strain levels consistent with an optimal rate of transformation.

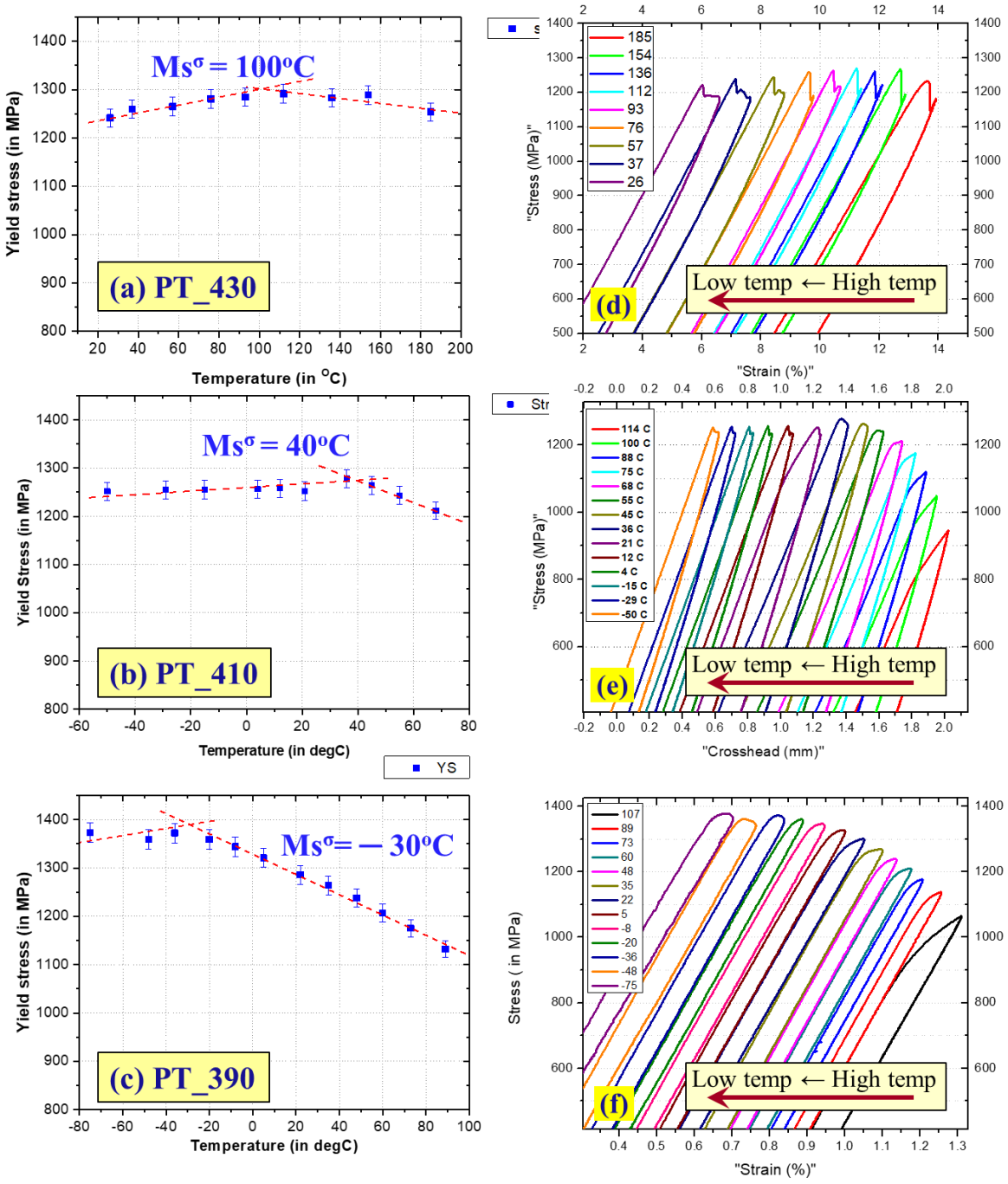

Figure 45: Yield stress versus testing temperature from single specimen Bolling-Richman tests for (a) PT_430, (b) PT_410, (c)PT_390 sample. The actual interrupted stress-strain plots for (d) PT_430, (e) PT_410, (f) PT_390 sample

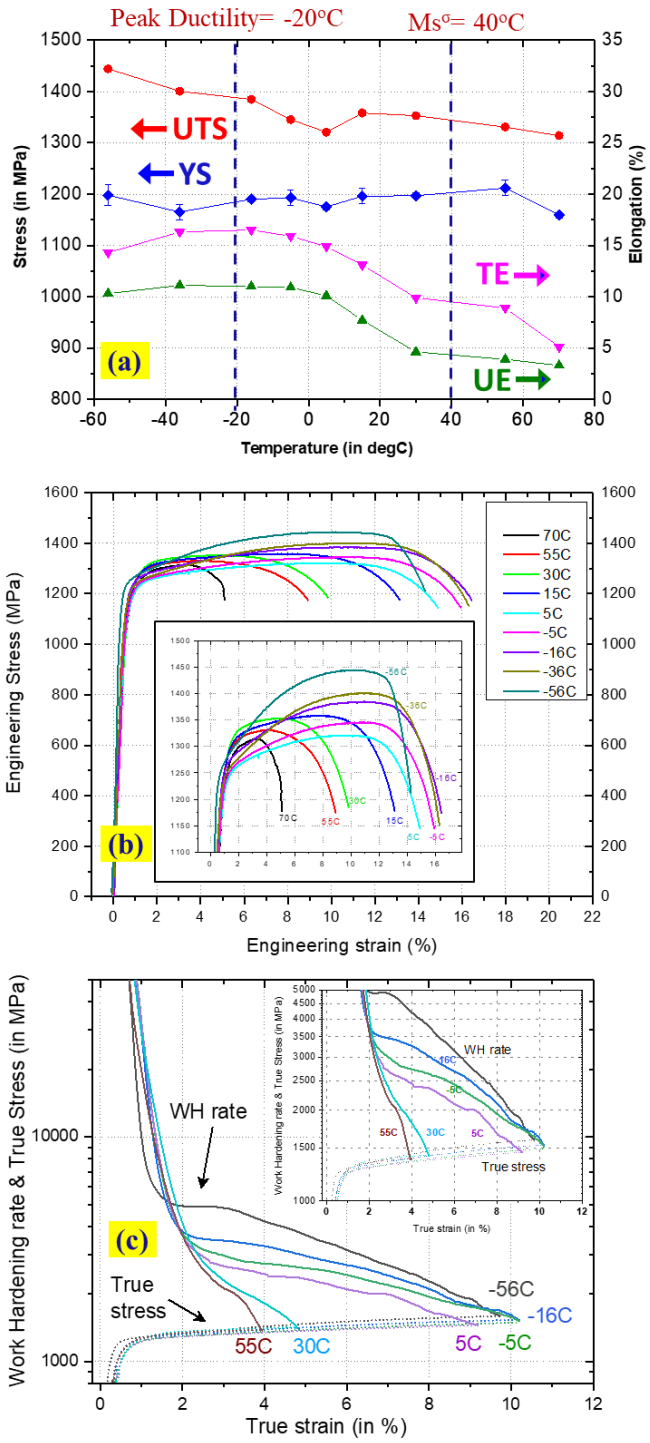

Figure 46: (a) Mechanical properties variation with testing temperature, (b) Engineering stress-strain plots from multiple specimen tests at different test temperatures, (c) True stress and Work hardening rate as functions of true strain at different test temperatures for QT270_PT410_100s sample

The measured Ms^{σ} temperatures are plotted as solid dots versus partitioning temperature in Figure 47. Solid line represents the predicted values using the austenite stability model with the derived critical driving force as function of PT. Ms^{σ} temperature seems to vary almost linearly with partition temperature in the evaluated range. The variation in austenite stability or Ms^{σ} temperature with PT is caused due to the difference in 1) frictional work done for interface movement against forest dislocations, W_F^D and, 2) the nucleation defect potency (n) of the remaining nucleation sites in retained austenite. The value of W_F^D as function of PT is determined in the carbon partitioning model and is plotted in Figure 47. The nucleation defect potency (n) at each PT has been calculated using the experimentally measured Ms^{σ} temperature and is also plotted in Figure 47.

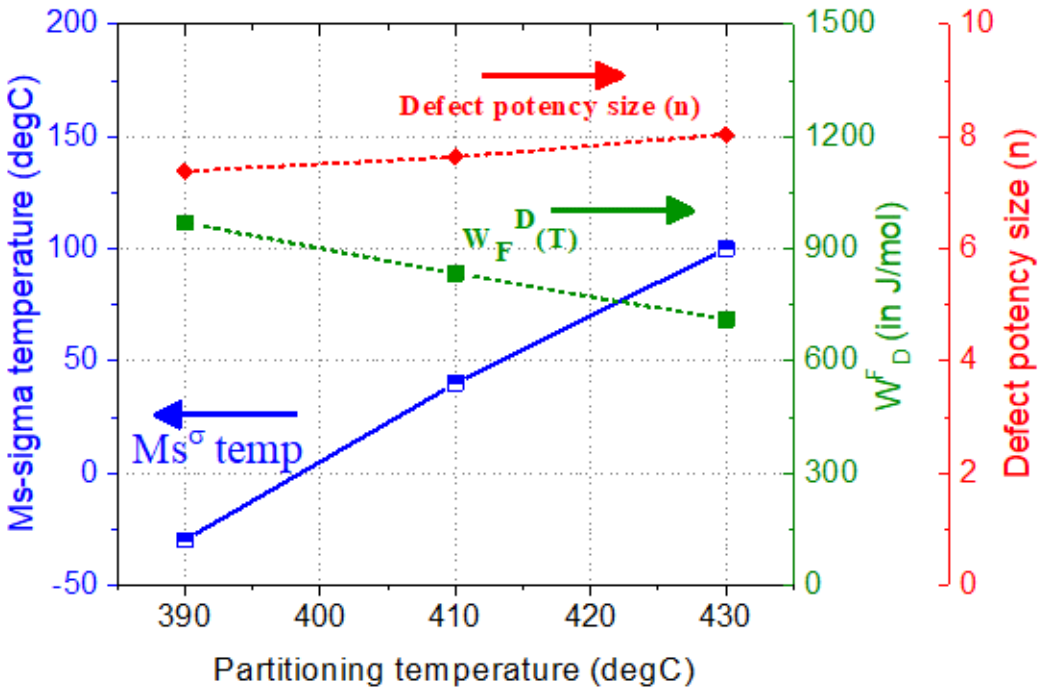

Figure 47: Ms^{σ} temperature variation with partitioning temperature along with calibrated values of W_F^D(PT) used in the partitioning model and defect potency size (n) used in the austenite stability model

3.2. Partition time (P-time)

Previous literature studies have concluded that an optimal partition time is required to maximize retained austenite fraction. Shorter partition time can result in inhomogeneous carbon distribution within retained austenite leading to fresh martensite formation during final quenching in lower C regions. On the other hand, partition time that is too long would lead to excessive carbide precipitation reducing C available for retained austenite. In the current study, the influence of partition time on the Q&P microstructure was studied using a set of experiments performed on Steel 2 (0.18C-2.02Mn-1.55Si-0.15Mo). The alloy was processed according to 5 different heat cycles with the same QT, PT but different P-times. A schematic of the heat cycles is shown in Figure 48. The samples were initially fully austenitized at 900^{o}C for 100secs before being quenched to 290^{o}C aiming for about 80% initial martensite fraction. The partition temperature was fixed at 420^{o}C. The chosen partition times were 10, 30, 60, 100 and 200 seconds.

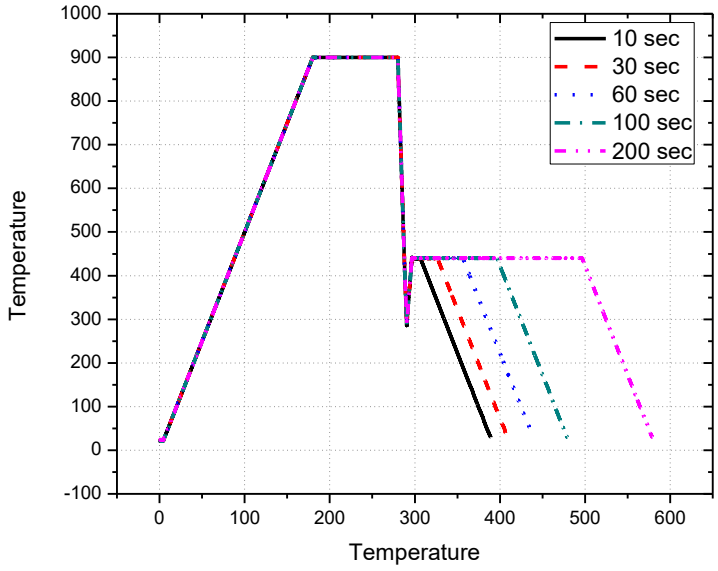

Figure 48: Temperature profile for the Q&P cycles with different partition times

3.2.1. Effect on microstructure and carbon partitioning

The samples were Q&P processed using a quench dilatometer which also measured the change in length of the sample as a function of time. Figure 49(a) plots the temperature and change in length versus time around the quenching step. The sudden increase in sample length just before t=290sec is due to onset of martensitic transformation. The slope of the length curve changes as the sample reaches QT and starts reheating to the PT. The change in length during reheating to PT at 25ºC/sec is attributed to thermal expansion and transformation in the remaining austenite. All the samples show very similar change in length behavior during the quenching and reheating stage. Figure 49(b) shows the change in length versus time for all the samples zooming in on the partition stage (starting t=297sec). Increase in sample length continues at early P-times reaching its peak around P-time=30secs (overall t=327sec). Thereafter, the sample length is seen to decrease with time. Two reasons that contribute to increase in sample length during isothermal holding are 1) transformation in the remaining austenite and, 2) carbon partitioning from martensite to retained austenite [153]. Decrease in sample length can occur from martensite tempering carbide precipitation. The combined effect of these factors results in the final change in length behavior. The variation of length with temperature for the complete cycle is plotted in Figure 50(a). All samples are fully austenitized and follow identical curves until the partition temperature. The final quenching section of the plot is magnified in Figure 50(b) to show the absence of any significant fresh martensite formation during final quenching. The dotted lines represent linear extensions of the expected thermal contraction behavior. The observed deviations would be due to the non-linear coefficient of thermal expansion of the FCC and BCC phases at these low temperatures as shown in the work of Bohemen et al. [155].

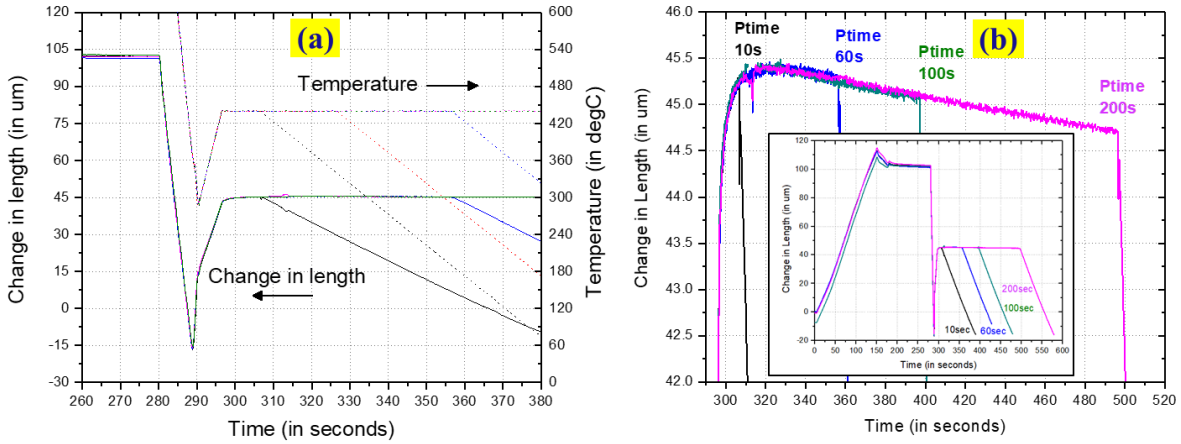

Figure 49: Dilatometer plots for (a) Change in length and temperature versus time zooming around quenching step, (b) Change in length versus time focusing on the partition step with inset of the overall complete plot

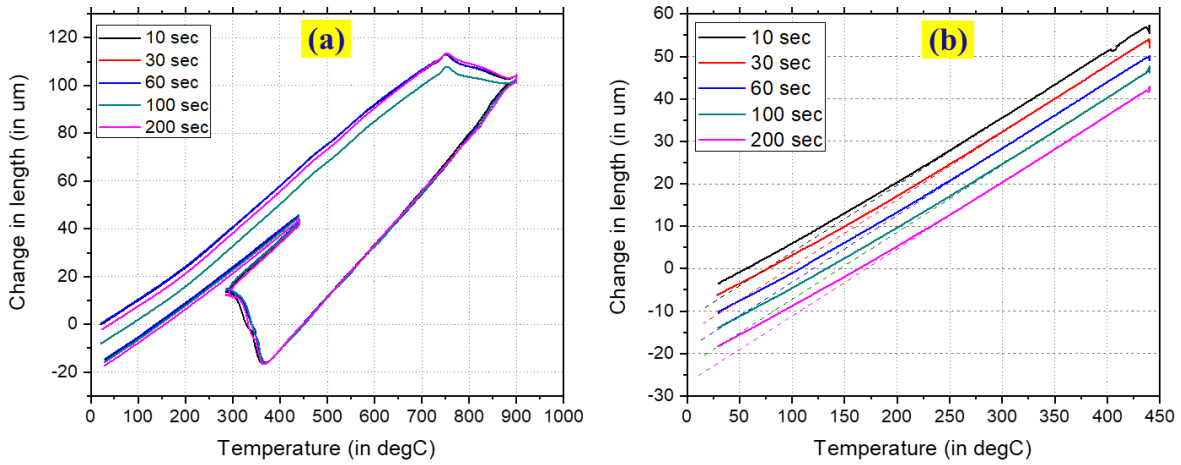

Figure 50: Change in length vs temperature for the (a) overall Q&P cycle, (b) Q&P cycle focusing on the final quenching step

SEM micrographs after nital etching for samples with Ptime of 10 and 200secs are shown in Figure 51. The microstructure in both cases seem very similar and contains mostly tempered martensite with some fraction of retained austenite. Carbide precipitation can be seen inside the martensite laths and lower bainite phase in both cases. However, no distinct difference in amount of carbide precipitation could be observed.

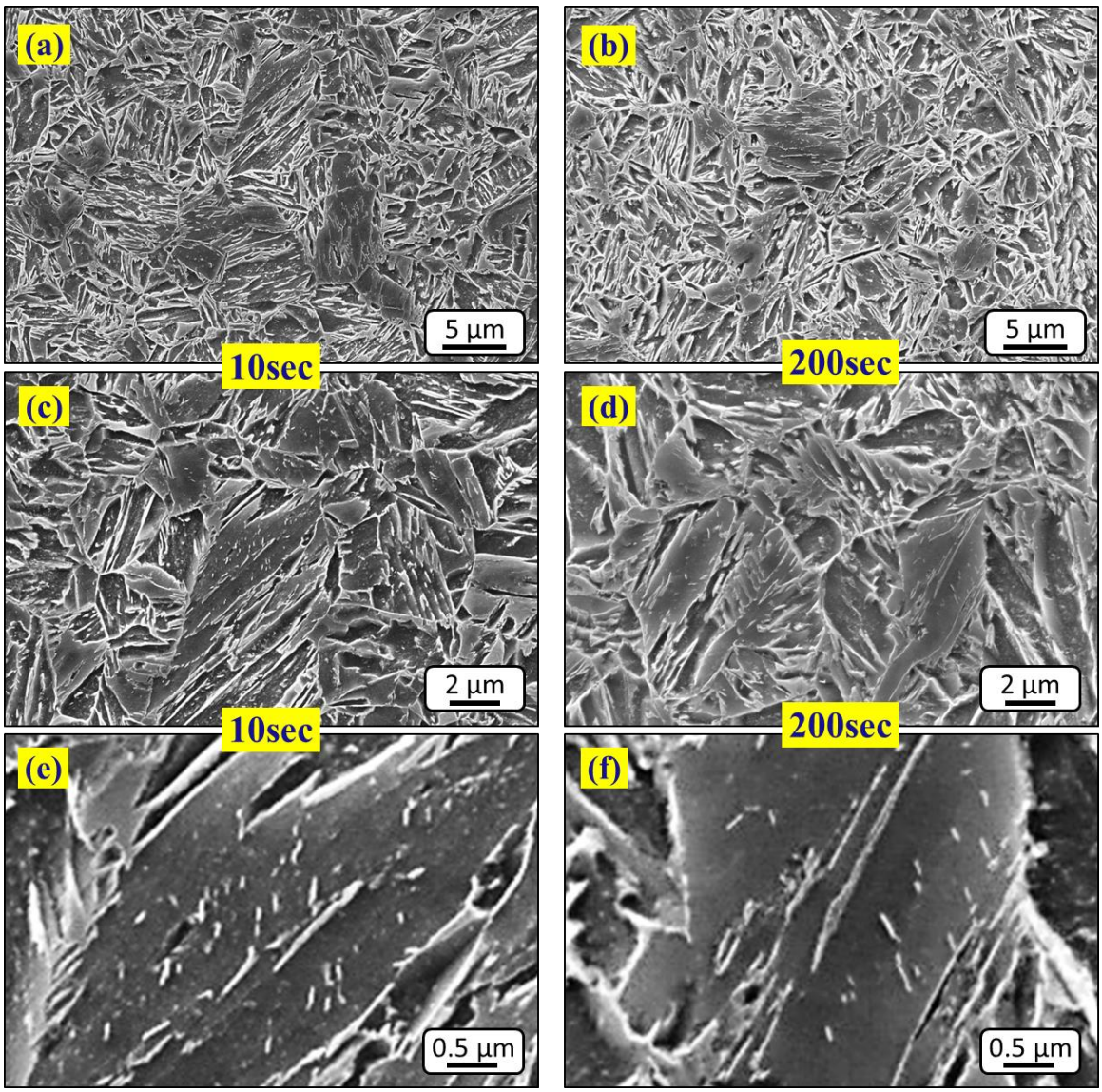

Figure 51: SEM micrographs after Q&P processing with partition time of (a, c, e) 10sec, (b, d, f) 200sec. White dots inside the martensite laths mark carbide precipitates

High energy x-ray diffraction experiments were carried out to accurately determine the austenite phase fraction and its bulk carbon content. The measured values for different Ptime conditions are reported in Table 11. Using these values and an average martensite carbon content from 3DAP experiments (~0.04wt%), we back-calculate the amount of carbon trapped in form of

carbides in the alloy. The wt% of carbon (out of 0.18 wt% nominal C in steel 2) lost to carbides is noted in the table and seems quite similar for the different partition times. The values at early Ptimes could be inaccurate due to higher martensite carbon content. The variation of austenite phase fraction and carbon content is plotted against partition time in Figure 52. Austenite phase fraction is seen to increase slightly with partition time reaching a maximum of about 6% for P-time of 200 secs. Austenite carbon content increases until 60secs after which it starts to decrease. Consistent with the DICTRA simulations to be discussed, the initial increase in carbon content until P-time of 60secs is attributed to continued carbon partitioning from martensite to austenite while afterwards carbide precipitation would reduce the chemical potential for carbon partitioning and thereby decrease austenite carbon content. Error bars for carbon content measurements represent the difference in lattice parameter measurements among the four different austenite intensity peaks from HEXRD.

Table 11: Measured austenite fraction, austenite carbon content and carbon lost in form of carbides for the Q&P cycles with different partition times using Steel 2 samples with QT=290^{o}C and PT=420^{o}C.

Time (sec)	**Austenite frac.** (in %)	**C_{aust}** (wt%)	wt% C in carbides
10	5.8	1.04	(0.082)
30	4.8	1.039	(0.092)
60	5.4	1.09	0.083
100	5.4	1.07	0.084
200	5.9	1.04	0.081

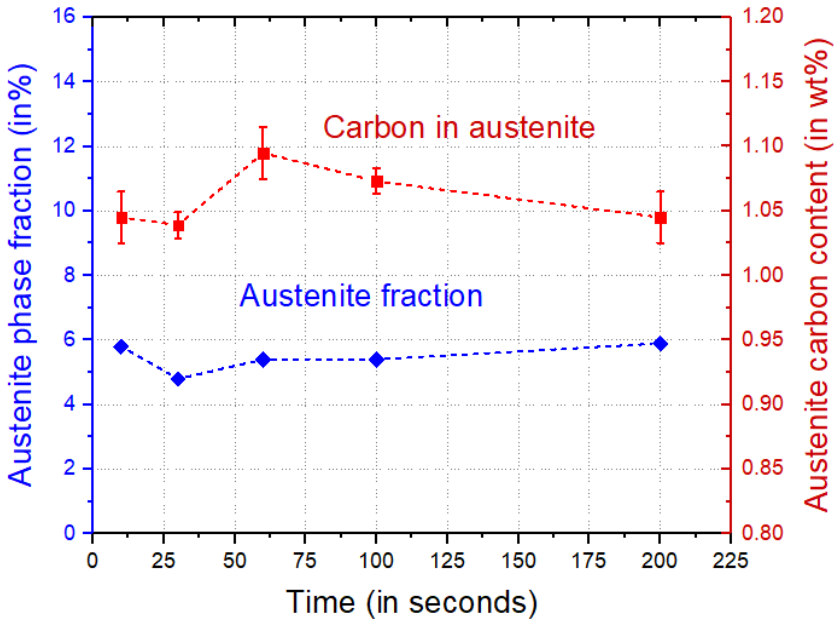

Figure 52: Variation of austenite phase fraction and its carbon content with partition time

3.2.2. DICTRA simulations for effect of Partition time

The evolution of individual phase composition with partition time was simulated using para-equilibrium DICTRA simulations. The detail setup of the simulations has been discussed in section 2.3.3. Similar to PE calculations in ThermoCalc, an effective stored energy term was also added to the free energy of the product phase. The simulations were performed starting with the same composition for martensite and austenite phase. The amount of substitutional alloying elements is set to the nominal alloy composition while the carbon content is set at a value after removing an estimated amount of carbon that would be lost to carbides (typically 50%). The size of the 1D cell for individual phases was set to 0.4μm for martensite and 0.2μm for austenite based on half-width of the phases measured using electron microscopy.

Figure 53 shows the carbon profile in a 1D cell of austenite and martensite for Steel 2 at different partition times when held at the partition temperature of 440^{o}C. A stored energy of 1265 J/mol was added to the ferrite phase as predicted using the stored energy model developed earlier. The

faster diffusion of carbon in martensite results in diffusion of almost all carbon in martensite to the interface region in less than one second of partitioning. Therefore, an initial a pile up of carbon is observed at the interface on the austenite side. The interface is seen to move towards BCC phase at the start of partitioning. Subsequently, diffusion of carbon in the austenite results in increasing the bulk austenite carbon content while decreasing the overall austenite phase fraction due to interface movement towards austenite. Movement of the interface maintains mass balance of carbon in the alloy. The austenite carbon content after 15secs of partitioning at 440°C seems to be homogeneous and reach a value of 1.08wt%. The change in the average austenite carbon content with time is plotted in Figure 55(a). The value is found to closely match the measured carbon content after 60secs of partitioning using HEXRD as noted in Table 11.

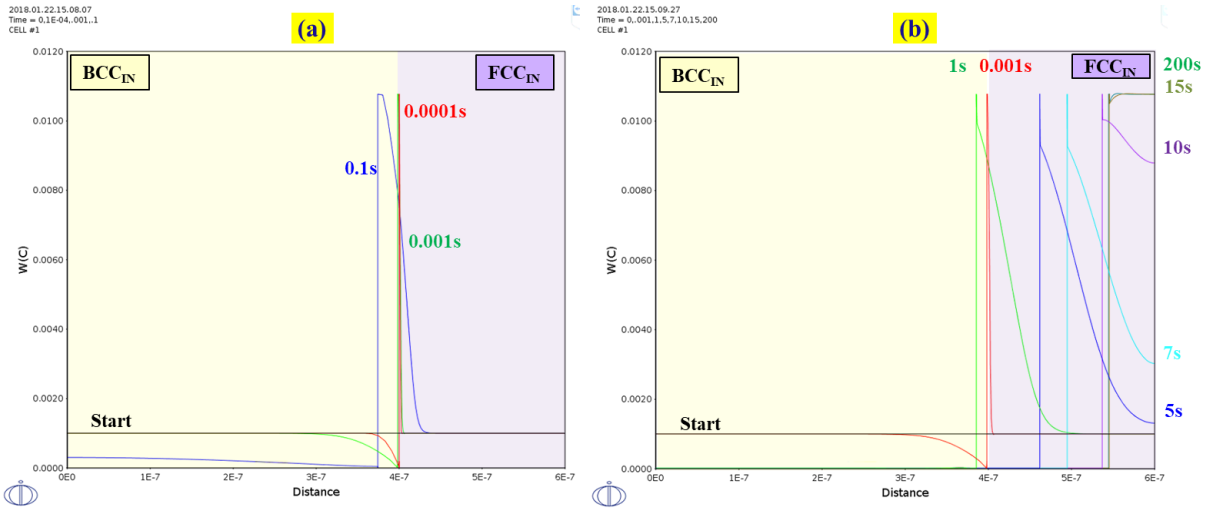

Figure 53: DICTRA simulation results for weight fraction of carbon in martensite (left) and austenite phase (right) for different partition time at partition temperature of 440°C. Stored energy added to BCC phase is 1265 J/mol.

The evolution of carbon content at a different partition temperature of 420°C is also shown in Figure 54. A different value of stored energy (1400J/mol) is added to the ferrite phase for partitioning at 420°C. The final austenite carbon content is predicted to be higher at around 1.1

wt% as seen in Figure 55(b). These simulations can be used to estimate the extra partitioning time required at lower partition temperatures to ensure homogeneous carbon distribution in austenite. The simulations can also be used to predict optimal partition times for different alloy compositions.

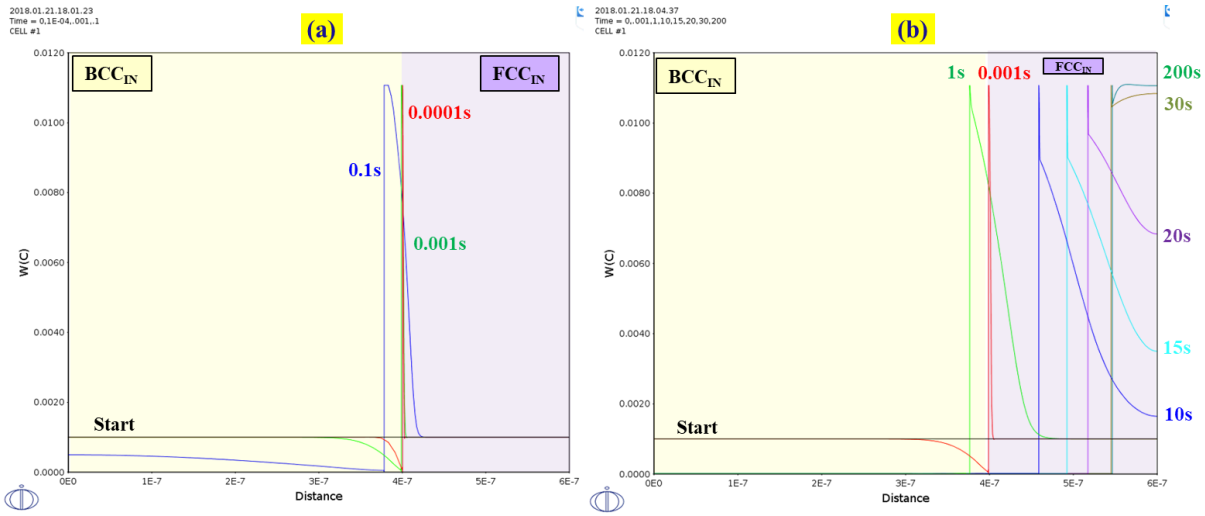

Figure 54: DICTRA simulation results for weight fraction of carbon in martensite (left) and austenite phase (right) for different partition time at partition temperature of 420°C. Stored energy added to BCC phase is 1400 J/mol.

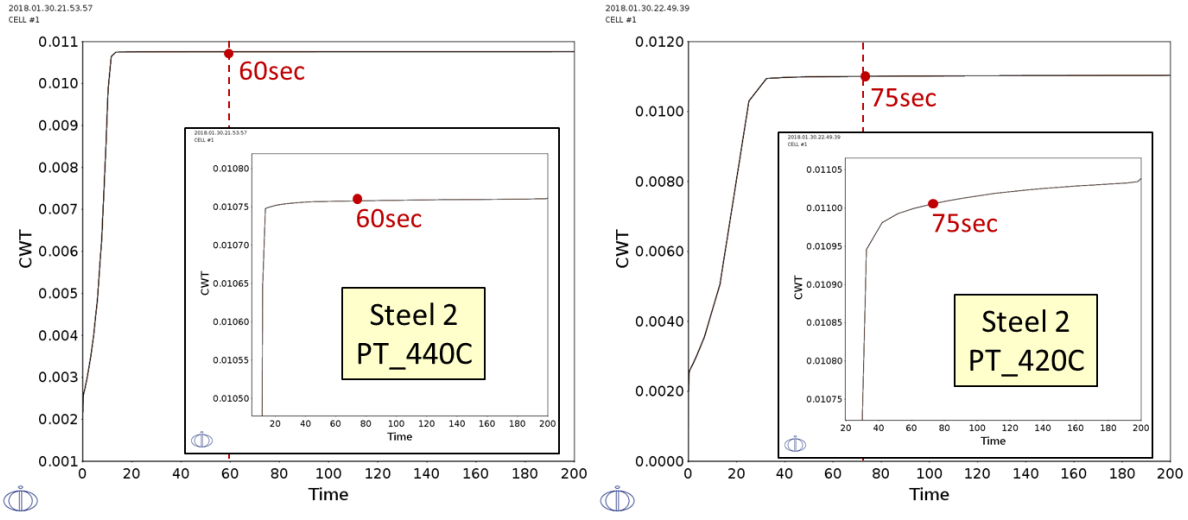

Figure 55: Average carbon content of austenite phase versus partition time at different partition temperatures, (a) 440°C, (b) 420°C as calculated using DICTRA simulations

3.3. Quench temperature (QT)

This section discusses the role of quench temperature and corresponding initial retained austenite content in determining the final microstructure after Q&P processing. Experimental characterization and predictions from the developed thermodynamic models will be compared. The following sub-sections will focus on the effect of QT on various microstructural features such as phase fraction of tempered martensite, austenite carbon content and austenite stability.

3.3.1. Determination of martensite start (Ms) temperature

As discussed previously in section 2.3.1, there are different proposed models to predict the martensite start temperature based on both empirical approaches and mechanistic theory. In the current research, a mechanistic approach was utilized which calculates the Ms temperature by determining the point of intersection of the required nucleation critical driving force and the chemical driving force available for transformation. The predicted critical driving force was discussed earlier while the chemical driving force is calculated using ThermoCalc© software with different available thermodynamic databases.

The predicted Ms values using the commercially available TCFE9 database and the proprietary MART5 database are noted in Table 12 and plotted in Figure 56. The predicted values using the more accurate MART5 database are in good agreement with experimental values. Although both databases give similar results for the given range of alloy composition, the difference between the predicted values increases strongly with increase in carbon content. The effect of carbon and manganese variation on calculated Ms temperature is shown in Figure 57. The difference is due to the difference in the chemical driving force calculated using the databases. MART5

incorporates third-law terms for low temperature calculations and thus can make more reasonable predictions than TCFE9.

Table 12: Experimentally measured Ms temperature versus predicted values using two different thermodynamic databases (TCFE9 and MART5)

	Ms exp (°C) Dilatometer	Model Ms (°C) MART5 database	Model Ms (°C) TCFE9 database
Steel 1	354	354	368
Steel 2	377	371	387
Steel 121	390	373	385
Steel 122	405	406	414
Steel 123	390	370	366
Steel 124	355	358	369
Steel 125	330	334	344
Steel 126	375	402	400
Steel 130	340	370	373

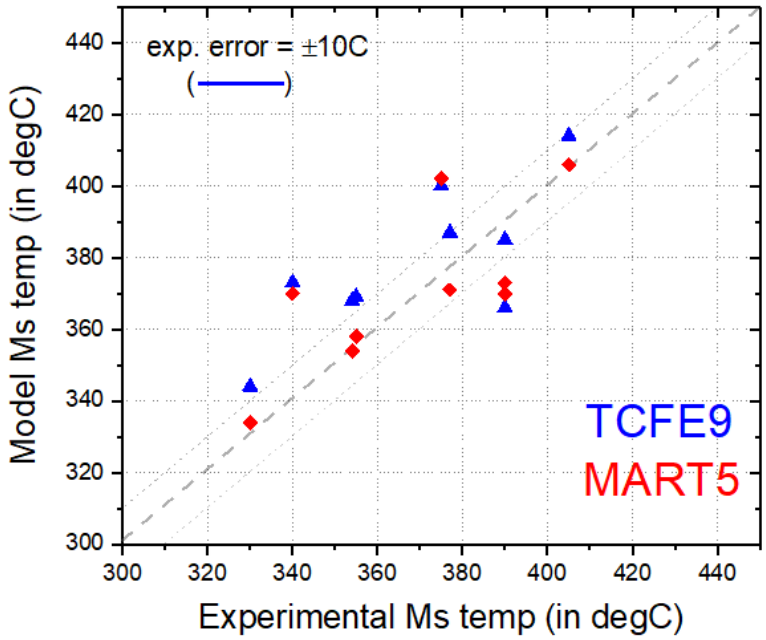

Figure 56 Plot of model predicted vs experimentally measured Ms temperature (using two different databases, TCFE9 and MART5)

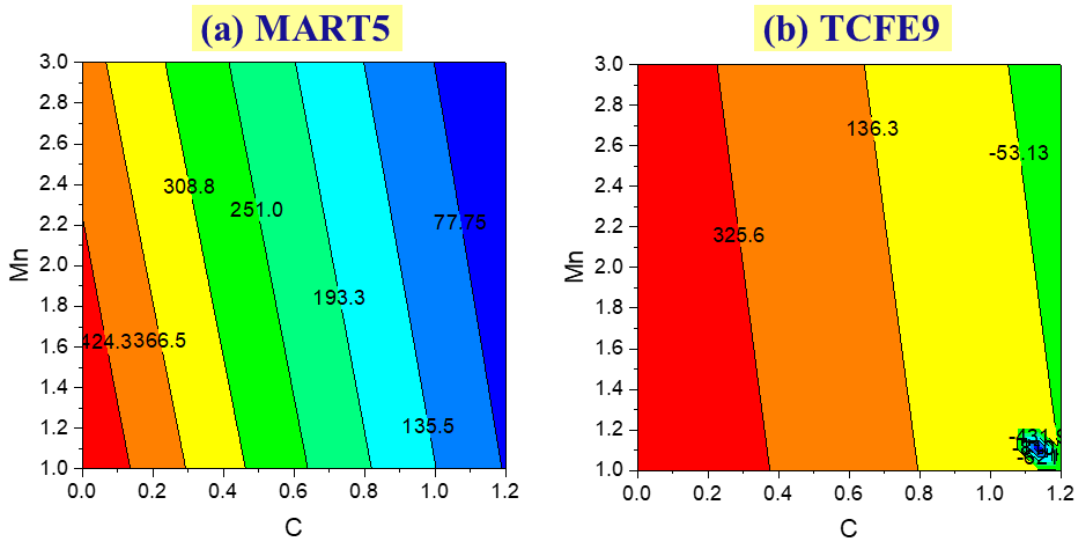

Figure 57: Calculated values of martensite start (Ms) temperature using (a)MART5 database and (b)TCFE9 database

3.3.2. Determination of martensite phase fraction

One of the key attributes of the Q&P microstructure decided by the quench temperature (QT) is the martensite phase fraction. The martensite fraction directly affects the material strength and influences the carbon available for partitioning to austenite. Dilatometer experiments were carried out on all the studied alloys by quenching them from single phase austenite to RT at a rate of 60K/sec or higher. The individual alloy compositions are listed in Table 6. The plots for the change in length of sample versus time are shown in Figure 58. All the alloys are austenitized above Ac3 temperature and then quenched (>60K/s) to room temperature. The calculated plots for martensite fraction versus quench temperature are shown by dotted lines in Figure 59. Decrease in manganese content increases the Ms temperature as seen comparing the steel 121 and steel 122 alloys. Increase in alloy carbon also decreases the Ms temperature as seen comparing steel 122 and steel 123.

As discussed earlier in section 2.3.1, different martensite phase fraction models have been proposed to model the martensite fraction as function of the quench temperature. The current work uses the mechanistic *Fe-martbain* model in the proprietary CMD software platform to predict the martensite fraction as a function of QT for all studied alloy compositions. The predicted values in solid lines are plotted alongside the measured values as dotted lines in Figure 59**,** showing reasonable agreement. Some of the model default parameters which were slightly modified to better describe the current system are as follows: G_{el} correction = 80 J/mol, Grain size number = 6 (~40um grain size), alpha = 0.33, P_{max} = 8.0e16, V_{bar} = 7.4e-17.

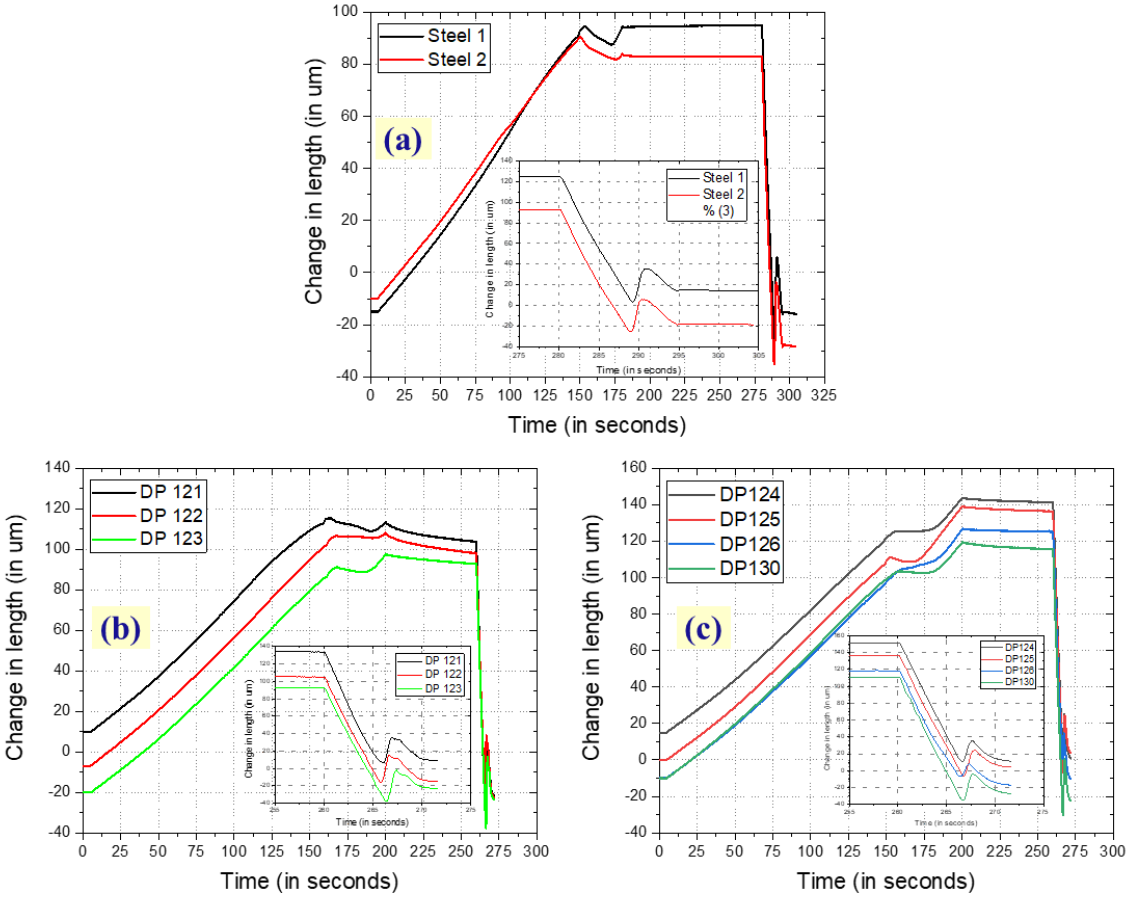

Figure 58 Dilatometer experiment results of change in length versus time for (a) Steel 1 & 2, (b) Steel 121,122,123, (c) Steel 124,125,126,130

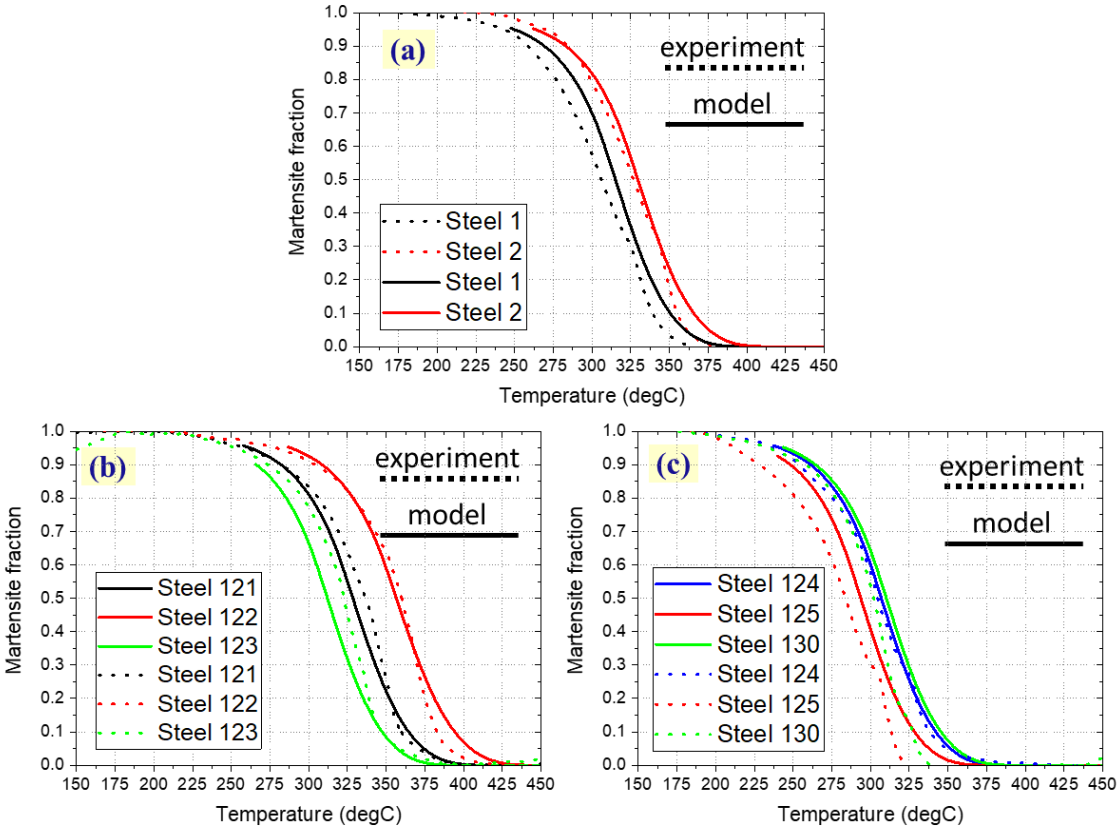

Figure 59: Experimentally measured Ms fraction using dilatometer and Fe-martbain model predicted values for (a) Steel 1 & 2, (b) Steel 121, 122, 123, (c) Steel 124, 125, 130

3.3.3. Effect on Q&P microstructure and carbon partitioning

The role of quench temperature on the microstructure after Q&P processing was studied on Steel 130 (0.25C-1.5Mn-2Si-0.2Mo-0.04Nb) with a Ms temperature of ~340^{o}C. Dilatometer measured fraction of martensite formed upon quenching to different QTs is plotted in Figure 60(a). Seven different QTs with different starting martensite fraction were chosen for microstructural analysis as marked by the red dots in Figure 60(a). The Q&P cycles are shown in Figure 60(b) with an inset showing a magnified plot of the region around the quench step. A prior full austenitization and fast quench treatment was performed before the Q&P cycle to ensure a more homogeneous

and similar starting microstructure in all cases. The samples were fully austenitized at 930°C for 100secs and quenched (60K/sec) to the different QTs. The samples were then immediately reheated to a PT of 430°C and held there for 60secs. Subsequently the samples were fast cooled (60K/sec) to room temperature. The quench temperatures along with the starting austenite fraction (after initial quenching) are listed in Table 13.

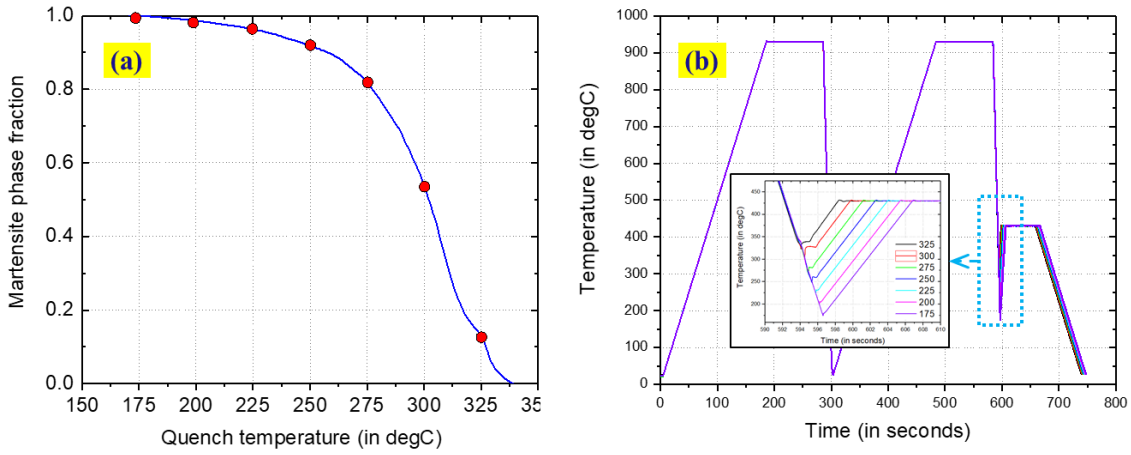

Figure 60: (a) Martensite phase fraction versus quench temperature with the marks denoting temperatures chosen for experimental study in Steel 130, (b) Temperature time plot for the Q&P cycle with prior quenching, inset magnifies the region around reheating step from QT to PT

Figure 61(a) plots the change in length versus temperature for the different Q&P cycles focusing on the quenching and partitioning step. Depending on the QT, the samples undergo initial martensite transformation to different degree of completion. Small differences in the transformation start temperature are due to experimental error and sample to sample variation. The amount of length change during isothermal holding at PT of 430°C is higher for lower QT cycles. The curves for different QTs are shifted along the y-axis for clearer comparison. Figure 61(c) plots a section of change in length versus time during Q&P heat cycle focusing around the quenching and partitioning step. The curves are shifted along the y-axis to clearly represent the

effect of change in QT. As the higher QT results in lesser fraction of initial martensite and thereby higher fraction of austenite at the beginning of the partitioning step, the increase in length during isothermal holding at PT varies with the resulting amount of bainitic transformation in the austenite during carbon partitioning. Higher starting austenite fraction results in larger length change associated with more bainite transformation. In the case of the lower QTs, tempering of the martensite leads to more carbide precipitation that results in a decrease in the length of the sample during partitioning. The length change during partitioning varies systemically with change in initial austenite content as seen in Figure 61(d). The partition time to reach maximum length change during partitioning decreases with decrease in starting austenite content. The maximum is seen clearly in the case of QT 225^{o}C at approximately P-time of 30secs. The change in length versus temperature during the final quenching step in Figure 61(b) shows a systematic deviation from the extrapolated straight lines due to non-linear thermal expansion at lower temperatures. Larger deviation from linear behavior is associated with lower austenite fraction in the microstructure based on the work of Bohemen [155]. Lower QT samples have higher deviations consistent with their lesser amount of retained austenite which is also measured by HEXRD measurements as shown later. The dilatation curves show no evidence of fresh martensite formation during the final cooling step.

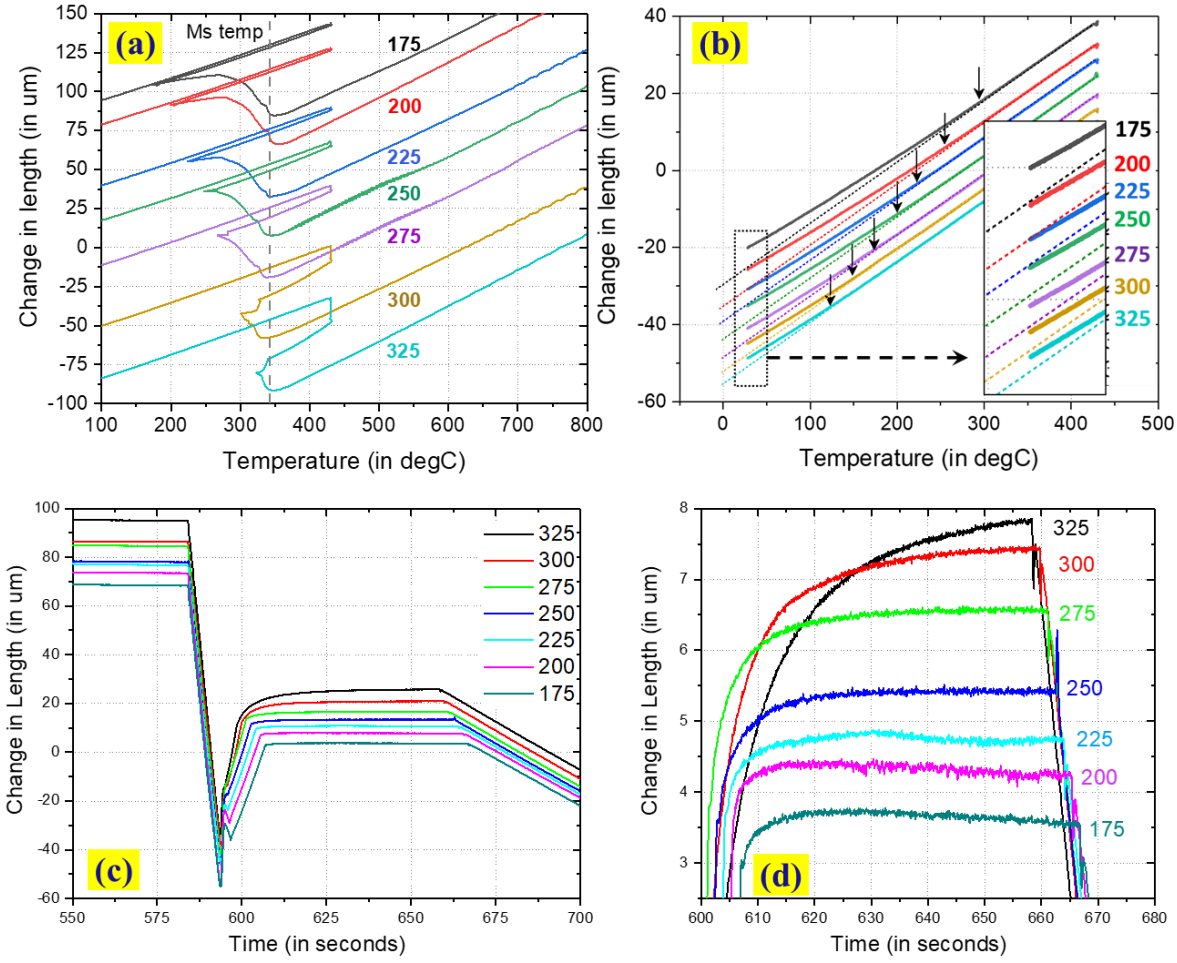

Figure 61: (a) Change in length versus temperature plot for Q&P cycles with different QT, zooming in on the quench & partition section.
(b) Change in length versus temperature focusing on the final quenching step,
(c) Change in length versus time for the Q&P cycles with magnified image focussing on the partition step shown in (d).

SEM micrographs after three selected Q&P cycles (QT_175, QT_250, QT_325) are shown in Figure 62. The microstructure in all three cases looks similar due to similarities of microstructural features of tempered martensite and lower bainite. However, the QT_175 sample has likely more carbides as estimated by qualitative analysis of the number of fine dots inside the laths.

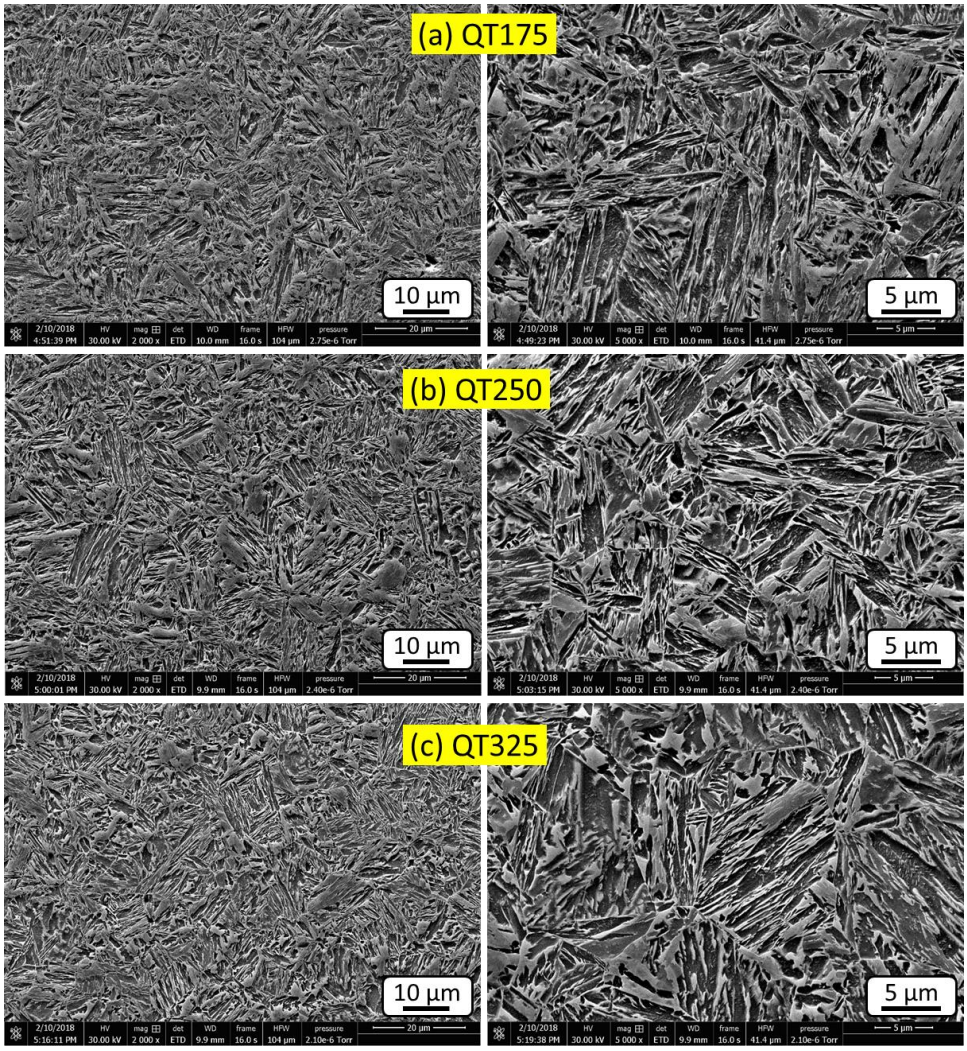

Figure 62: SEM micrographs after Q&P processing with QT of (a) 175^{o}C, (b) 250^{o}C, (c) 325^{o}C

EBSD experiments were performed to analyze the distribution and morphology of austenite phase in the final microstructure. The results for two different quench temperature cases (QT_250 and QT_325) are shown in Figure 63. OIM color maps for individual phases with superimposed band contrast images show the phase orientations and their distribution. The phase maps indicate slightly larger blocky austenite in the case of higher QT sample. This is consistent with previous experimental studies reporting more blocky austenite in the case of bainitic

microstructures compared to martensite. The lesser amount of initial martensite is thus expected to result in higher fraction of blocky austenite due to less amount of interlath austenite films.

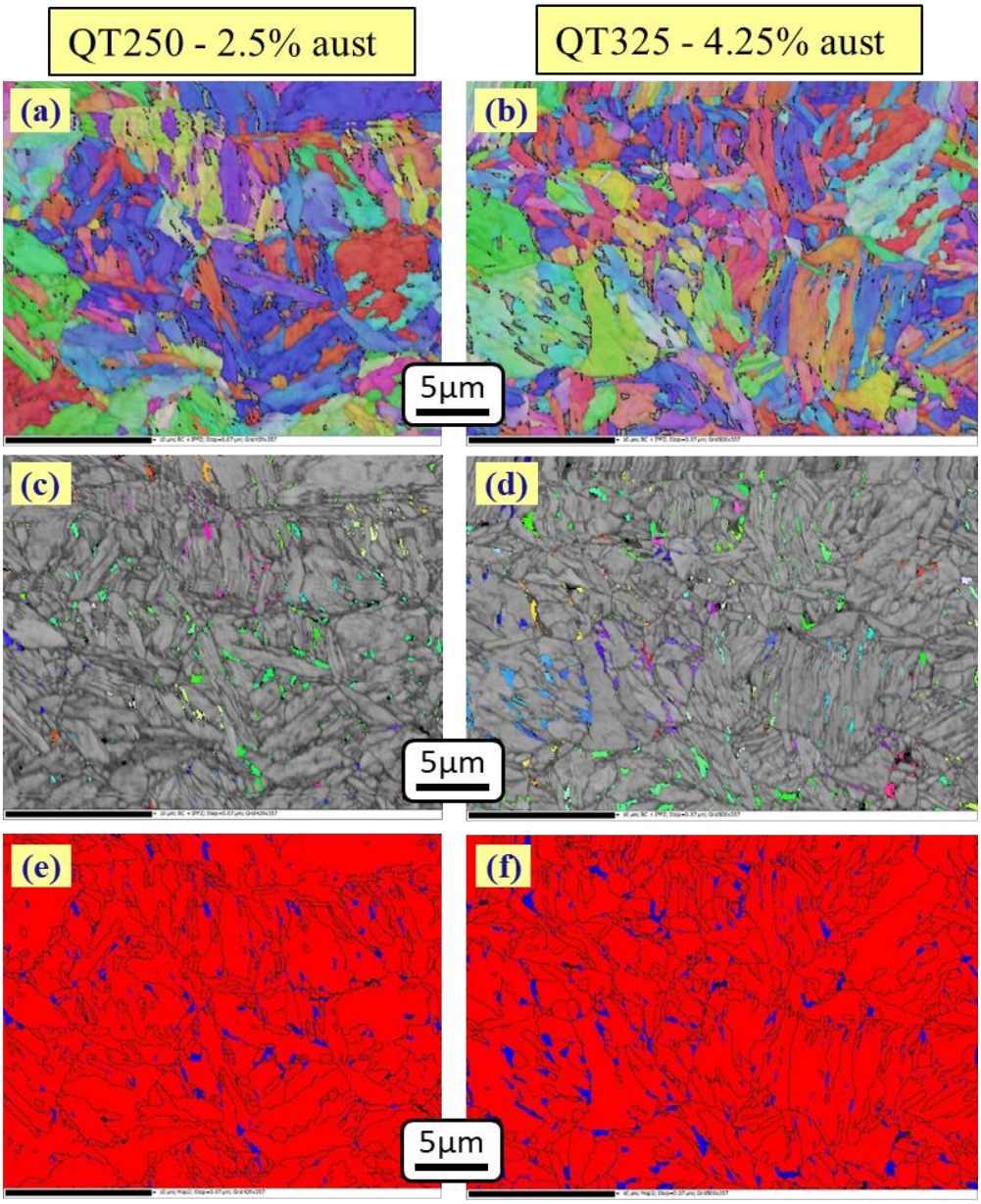

Figure 63: EBSD analysis of Steel 130 samples after Q&P processing at two different quench temperatures. (a, b) IPF color maps for martensite+bainite superimposed on band contrast image, (c,d) IPF color maps for austenite phase superimposed with band contrast map, (e,f) phase map with blue representing austenite and red for martensite/bainite phase.
Note: Color legend for (111) is blue, (001) is red and (101) is green.

Diffraction studies using high energy synchrotron radiation were performed to determine the individual phase fractions and their compositions. The measured quantities for the different QT samples are listed in Table 13. Austenite carbon content and phase fraction measured from HEXRD experiments are plotted against QT in Figure 64(a). Austenite phase fraction decreases with decrease in quench temperature until QT_250 after which it increases with further decrease in QT. The carbon content of the austenite phase also decreases with decrease in quench temperature but then jumps up from QT_250 to QT_225 and subsequently continues to decrease down to QT_175. The variation observed with QT is small compared to the observed variation with PT showed in section 3.1.2. Through W_F^D, austenite carbon content is affected by the dislocation density in the matrix which may be dependent on the fraction of initial martensite compared to bainite formed during partitioning. Lower quench temperature results in higher martensite fraction with high dislocation density that increases the effective stored energy by increasing the W_F^D frictional work. Increase in the effective stored energy would thus reduce the austenite carbon content. However, the carbon content is observed to be higher for QT_225 compared to QT_250. This correlates with a reversal of the direction of austenite-martensite interface movement in between these two temperatures. Figure 64(b) plots the starting austenite phase fraction after the quenching step and the final austenite fraction for the different QT samples. During the partitioning step, austenite fraction decreases for all samples with QT>250^{o}C while for QT<250 the final austenite fraction is very close or higher than the starting austenite fraction. Thus, the direction of movement of FCC/BCC interface is reversed moving towards austenite phase for QT<250^{o}C. In such scenario, the dissipated energy component is added to the product FCC phase resulting in the increase of austenite carbon content. The total

value of effective stored energy in this case would be different and depend on the dislocation density ahead of the moving interface. Figure 65(b) plots the austenite carbon content and calculated values of effective stored energy for the different QTs. Interface reversal is associated with a step change in effective stored energy of about 20J/mol. Figure 65(b) plots the fraction of alloy carbon lost in the form of carbides for the different QTs. The loss of carbon increases with decrease in QT corresponding to the increase in initial martensite fraction. The reversal of the direction of interface movement also seems to result in a step change in amount of carbide precipitation.

Table 13: Measured quantities for samples with different QT
(Steel 130, PT=430C, Ptime=60secs)

QT	C_aust	Starting Austenite	Final Austenite	C lost to carbides	Fraction of alloy C in carbides	Effective SE	W_F^D (W_F^{SS}=617)
^oC	wt%	%	%	wt%	%	J/mol	J/mol
175	1.182	1	5.2	0.15	60.2%	1370	753
200	1.184	2	4.8	0.16	62.0%	1370	753
225	1.202	5	4.1	0.16	64.9%	1360	743
250	1.158	9	7.6	0.13	50.0%	1380	763
275	1.163	19	7.5	0.13	50.3%	1380	763
300	1.179	45	8	0.12	47.6%	1370	753
325	1.18	85	9.6	0.10	40.2%	1370	753

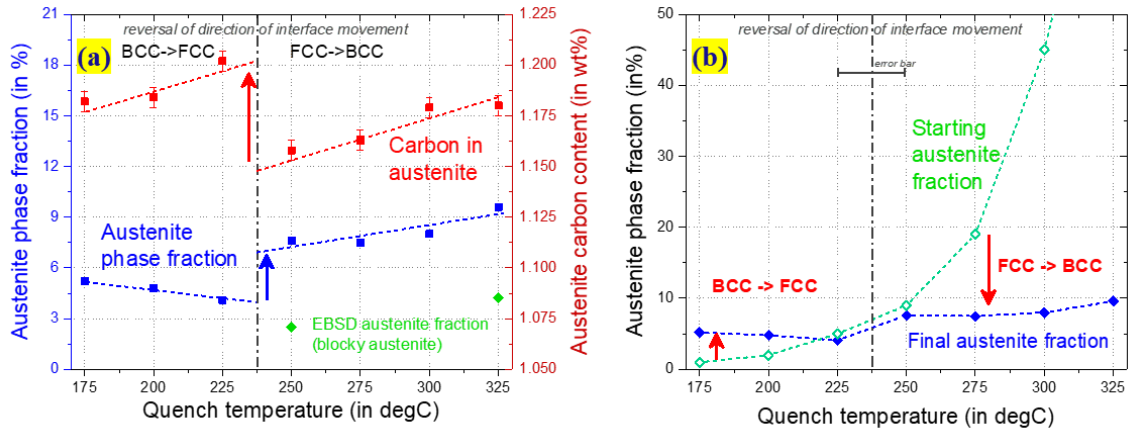

Figure 64: (a) Final austenite phase fraction and carbon content versus quench temperature, (b) Initial and final austenite fraction versus quench temperature

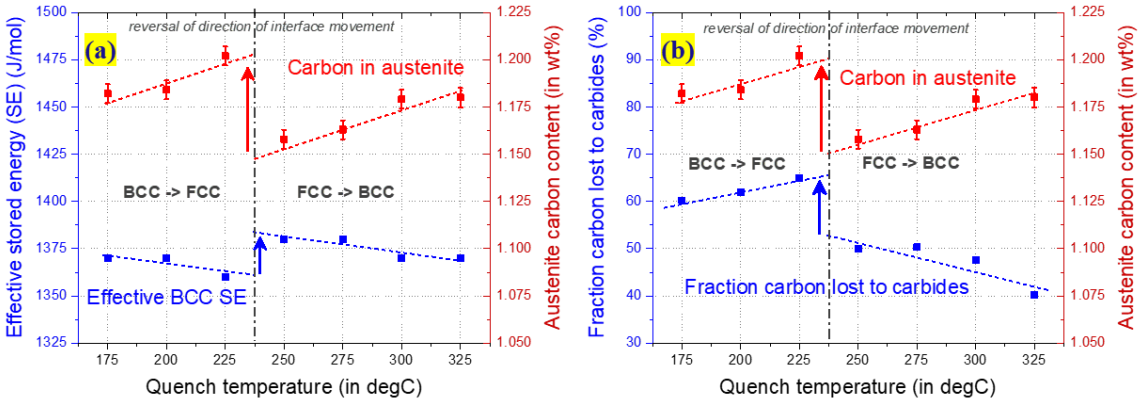

Figure 65: (a) Variation of calculated effective stored energy and (b) calculated fraction of alloy carbon lost to carbides for different QT. The austenite carbon content is also plotted in both cases

Similar analysis to quantify the effect of QT was carried out using data from the thesis research of T. Koopmans on a fully austenitized 0.2C-3.5Mn-1.5Si0.5Mo alloy with a PT of 400^{o}C for 50sec [61]. The plots for austenite carbon content, fraction of alloy carbon lost to carbides along with individual phase fractions as functions of QT are shown in Figure 66. Austenite carbon content decreases with QT at higher QT temperatures similar to the current work. An increase in austenite carbon content at low QT is consistent with the idea of reversal of the direction of interface movement, but the region of reversal is not as clearly established as shown in Figure

66(b). Detailed differences in the two studies could be explained by considering the effect of insufficient P-time at the PT. In the current work, the 0.25C-1.5Mn alloy is held at a PT of 440°C for 60secs to ensure complete partitioning compared to the Koopmans alloy, 0.2C-3.5Mn which is held at a PT of 400°C for 50secs. The partitioning condition in Koopmans work may not be sufficient for completion of the reverse austenite transformation. The fraction of alloy carbon lost in form of carbides is also seen to increase with decrease in QT.

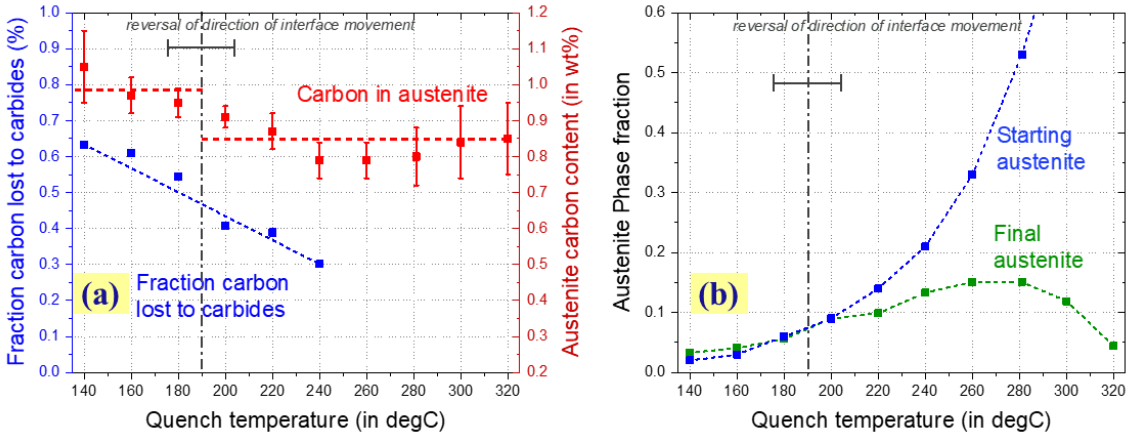

Figure 66: Reported measurements after Q&P processing of 0.2C-3.5Mn-1.5Si0.5Mo alloy at PT of 400C for 50sec in the thesis work of T. Koopmans [61].
(a) Austenite carbon content and fraction of alloy carbon lost to carbides versus QT,
(b) Starting austenite (after quench step) and final austenite fraction versus QT.

3.3.4. Predicted effect on austenite stability

The effect of QT on the austenite stability can be predicted by determining its influence on the various factors contributing to austenite stability which include the following:

1) Austenite carbon content
2) Defect potency of nucleation sites in the retained austenite
3) Forest dislocation content

The variation in carbon content of austenite with QT should result in different austenite stability similar to its variation with PT. The change in austenite carbon content with quench temperature is much smaller compared to that of partition temperature and therefore the stability variation due to this factor is expected to be small. Difference in austenite stability could also result from variation in the defect potency (*n*) values of the remaining nucleation sites in austenite. The defect potency of nucleation sites in austenite for martensite transformation follow a distribution from highly potent sites to lesser potent ones. The highly potent sites are the first to nucleate martensite upon quenching (corresponding to n~13 at Ms) while the lower potent ones remain unused due to interrupted quenching at the QT. For lower QTs, the unused nucleation sites would have an average potency much smaller compared to higher QTs. This is consistent with the n~7.5 determined in Table 9 for the retained austenite. According to the mechanistic theory of ΔG_{Crit}, lower defect potency (*n*) of nucleation sites means a higher critical driving force for transformation and thus higher austenite stability:

$$\Delta G_{Crit} = -\left(G_{el} + \frac{2\gamma}{nd}\right) - W_F^D - W_F^{SS}$$

Lower QT may produce higher dislocation density associated with the higher fraction of formed martensite, increasing W_F^D. Thus, lower QT could promote more stable retained austenite.

Overall, the combined effect of the above factors would determine the austenite stability for different QT conditions. Except for austenite carbon content, the other two factors favor higher austenite stability for lower quench temperatures.

Chapter 4. Carbide precipitation and Multiple austenite stability in Q&P steels

4.1. Carbide precipitation

As discussed earlier in section 1.4.4, carbide precipitation is one of the major factors limiting mechanical properties of Q&P steels. Carbide precipitation reduces the amount of carbon available to partition and stabilize austenite thus limiting the final retained austenite fraction. The alloys studied in the current work also have a very significant fraction of alloy carbon lost to carbides. Microstructural characterization tools were utilized to study the precipitated carbides. Depending on the alloy composition and partition temperature conditions, multiple experimental studies on Q&P steels have demonstrated the presence of different types of carbides. Some of the commonly reported carbides are cementite and transition carbides (ε-carbide). Higher partition temperatures (>~400^{o}C) usually result in cementite precipitation whereas transition carbides are observed for lower partition temperatures.

4.1.1. Microstructural characterization

Carbide precipitation in the Q&P alloys studied in the current work was observed using SEM microscopy as shown earlier in Figure 51. The carbides are usually seen as fine dots inside the martensite laths or in the lower bainite regions. HEXRD experiments were also performed to detect intensity peaks from precipitated carbides to identify the type of carbides and their volume fraction. Intensity versus two-theta angle plots for scans with long dwell time around a cementite intensity peak showed faint peaks as shown earlier in Figure 41(b). The carbide precipitates were realized to be too small and low in volume fraction to be clearly detected due to peak broadening and low peak intensity. 3DAPT experiments performed on Q&P processed Steel 1 samples showed the presence of carbides in the martensite matrix. The tip reconstructions with the carbon

atoms (in red dots) and manganese atoms (in blue dots) distribution in the different phases are shown in Figure 67. The austenite phase is clearly enriched in carbon while the martensite phase is depleted of carbon. The carbides are seen to precipitate in the martensite phase. The precipitates are found close to the austenite/martensite interface and also well inside the martensite matrix. Proximity histograms plotting the averaged variation of composition perpendicular to the martensite/carbide interface are shown alongside the tip reconstructions. The carbides are enriched with more than 15at% of carbon. Despite the small partition time in Q&P cycles, substitutional alloying elements have clearly begun partitioning in between the carbide and martensite phase. As expected for cementite, manganese and chromium are slightly enriched in the carbide while silicon is depleted. The composition of the carbides along with the neighboring BCC matrix are listed in Table 14. The precipitated carbides can be formulated as $(Fe_{0.91}Mn_{0.05}Si_{0.03}Cr_{0.01})_3C_{0.62}$.

Table 14 Composition of carbide and matrix from one of the 3DAPT reconstructions

(at%)	BCC matrix	Carbide
Fe	93.94%	75.1%
Al	0.04%	0.13%
C	0.10%	17.1%
Cr	0.37%	0.71%
Mn	2.24%	4.16%
Si	3.23%	2.61%

Although carbide composition could be accurately determined using 3DAPT experiments, quantitative analysis of the amount of carbide precipitation is quite difficult using APT or TEM experiments. As discussed earlier, the amount of carbide precipitation can be estimated by

determining the amount of starting alloy carbon content lost in the form of carbides. This was calculated by subtracting the amount of carbon in the austenite phase and the martensite phase from the overall alloy carbon content. The amount of lost carbon for a set of different alloys with different Q&P processing studied in the current work is shown in Table 15. The analysis led to useful insights about the role of composition and partition temperature on carbide precipitation. The differences due to other processing conditions were minimized by choosing the quench temperature in all cases to have 80% of starting martensite fraction and using minimum necessary partition times for different PTs to avoid unnecessary excess carbide precipitation. The results confirm a significant amount of the alloy carbon content (30-70%) is lost in the form of carbides in all the alloys. The fraction of lost carbon for different composition and PT are plotted in Figure 68. The variation of carbon lost to carbides with PT is observed to be smaller compared to the variation with composition. The amount of carbide precipitation (or carbon loss) can be correlated with the para-equilibrium (PE) driving force for cementite precipitation and coarsening rate constant for cementite precipitation in the martensite matrix as described in the next section. The values of these parameters for the different Q&P alloys studied in the current work are listed in Table 15. The highlighted compositions in Figure 68 at the same PT of 430^{o}C implies that decreasing the amount of substitutional element Mn and addition of interstitial element C leads to an increase in the amount of carbides. The alloy with 0.25C-1.5Mn has more carbide precipitation compared to 0.2C-2.2Mn in correlation with an increase in the coarsening rate constant while 0.3C-1Mn has even more carbides despite a lower coarsening rate but higher PE driving force for cementite precipitation.

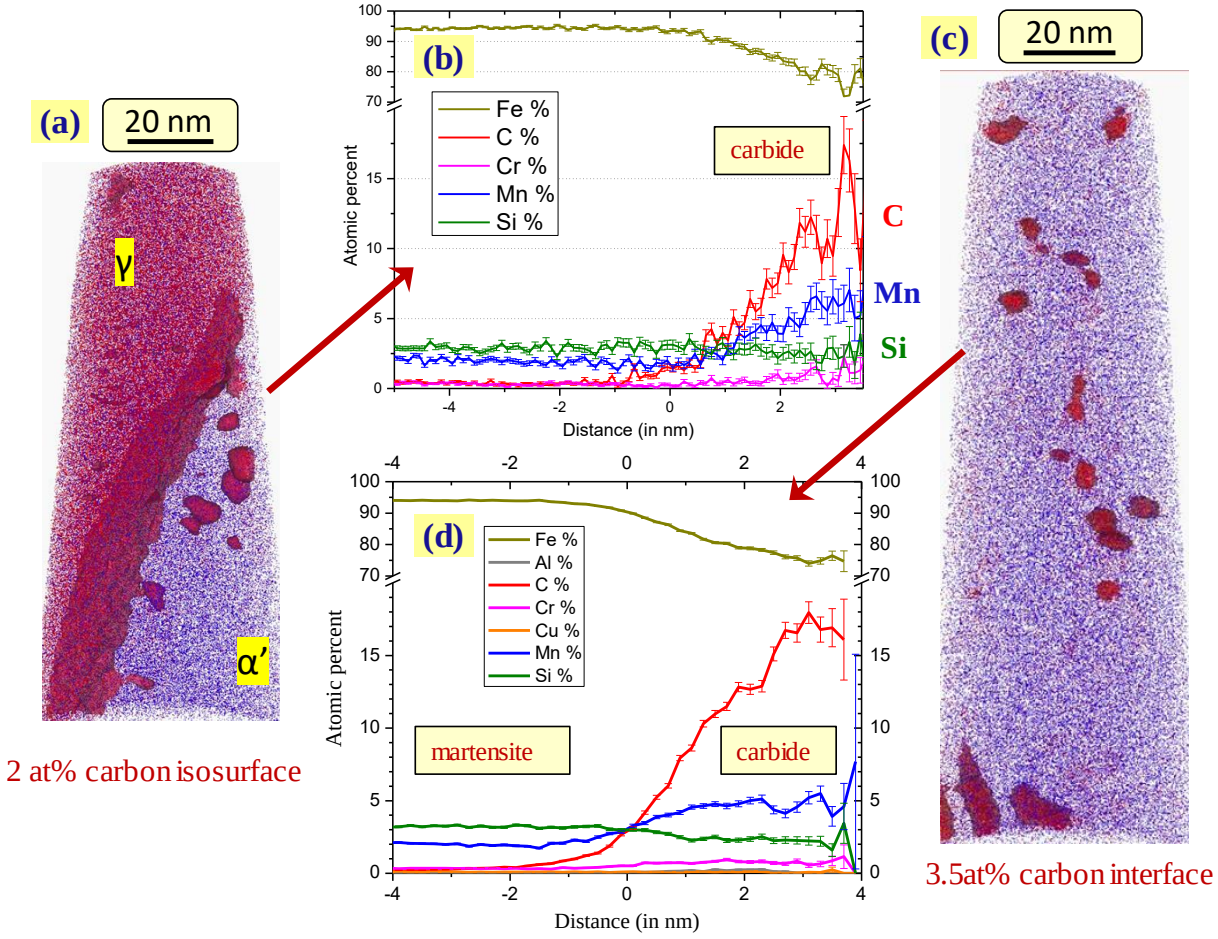

Figure 67: 3D APT results observed in Steel 1 for QT300_PT450_100s processing. (a) Tip reconstruction showing the austenite martensite interface along with carbides in the martensite outlined by an artificial 2wt% carbon isosurface, (b) Proximity histogram showing the averaged composition variation across the martensite/carbide interface. (c) Tip reconstruction showing carbides inside the martensite matrix outlined by a 3.5at% carbon isosurface, (d) Proximity histogram showing the averaged composition variation perpendicular to the martensite/carbide interface

Table 15: Carbon lost to carbides for different alloys & processing along with the para-equilibrium driving force for carbide precipitation and coarsening rate constant (**carbon content calculated using the empirical eq. used in the current work*)

No.	**Alloy composition (in wt%)**	**QT (ºC)**	**PT (ºC)**	**Ptime (sec)**	**Aust frac (%)**	**C_{Aust} (wt%)**	**C lost to carbides (wt%)**	**fraction alloyC lost**	**PE DF cementite (KJ/mol)**	**Coarsen rate const. (m^2/s/J/mol)**
Steel 1	0.2C 2.2Mn 1.5Si 0.2Cr	270	430	75	8.2	1	0.081	0.406	5.16	5.65E-29
Steel 1	0.2C 2.2Mn 1.5Si 0.2Cr	270	410	100	6.9	1.05	0.090	0.452	5.42	1.10E-29
Steel 1	0.2C 2.2Mn 1.5Si 0.2Cr	270	390	150	7.2	1.1	0.084	0.418	5.69	1.97E-30
Steel 2	0.18C 2Mn 1.55Si 0.15Mo	290	420	75	5.3	1.11	0.083	0.463	5	2.44E-28
Steel 2	0.18C 2Mn 1.55Si 0.15Mo	290	440	60	6.9	1.08	0.068	0.379	4.73	1.05E-27
Steel 121	0.2C 1.8Mn 1.5Si 0.2Mo (+B,Ti)	310	420	75	6.5	1.17	0.087	0.433	5.21	2.22E-28
Steel 122	0.2C 1Mn 1.5Si 0.2Mo (+B,Ti)	325	450	60	1.1	1.36	0.145	0.727	4.69	1.83E-27
Steel 123	0.3C 1Mn 1.5Si 0.2Mo (+B,Ti)	300	430	75	5.6	1.44	0.182	0.605	5.55	4.49E-28
Steel 130	0.25C 1.5Mn 2Si 0.2Mo	275	410	100	7.5	1.23	0.121	0.483	4.33	9.66E-29
Steel 130	0.25C 1.5Mn 2Si 0.2Mo	275	430	60	7.5	1.16	0.126	0.503	4.07	4.47E-28
Lit. [69]	0.28C 1.5Mn 1.6Si **1Cr**	240	400	180	17	1.2*	0.043	0.150	5.38	1.04e-30
Lit. [49]	0.2C 4Mn 1.6Si **1Cr**	210	450	300	32	0.3*	0.077	0.390	4.64	1.64e-28

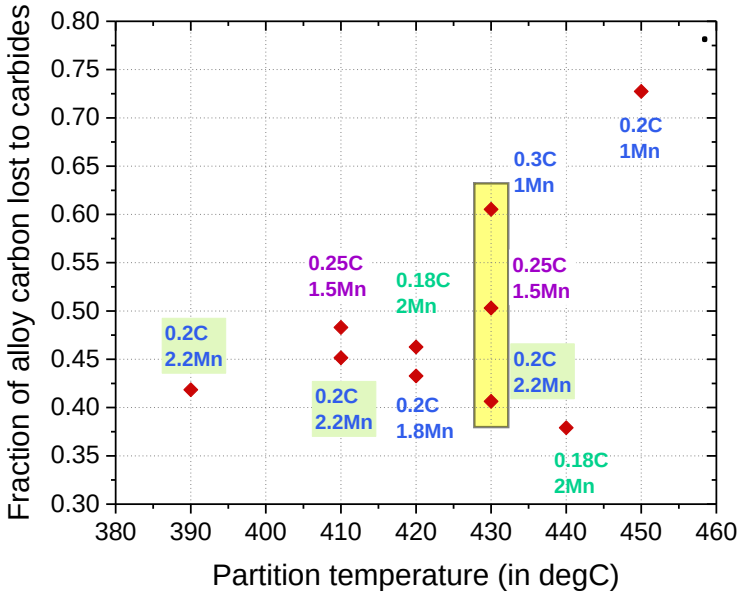

Figure 68: Fraction of alloy carbon lost to carbides versus partition temperature for different alloy compositions. Note: QT was fixed to have same fraction of initial martensite while partition time was different for different PT to minimize their effect

4.1.2. Modeling cementite precipitation behavior

The current section summarizes attempts to relate the observed carbide precipitation behavior to the two different thermodynamic and kinetic parameters: 1) Para-equilibrium driving force (DF) for cementite precipitation and 2) Coarsening rate constant for cementite inside the martensite matrix. In the 3DAPT reconstructions shown earlier the carbides were found to have composition closer to para-cementite than equilibrium cementite. The addition of silicon to Q&P alloys is also known to reduce carbide precipitation as it is an effective inhibitor of para-equilibrium cementite. These observations suggest a potential correlation between the PE driving force for cementite precipitation and the amount of carbide precipitation. Thermodynamics of carbide precipitation is accounted in the DF calculations however diffusion kinetics of precipitation would also play an important role because of the short duration of the Q&P heat cycles. Since most of carbide precipitation is seen inside the martensite laths, the coarsening rate constant for cementite in the martensite matrix would be a useful parameter to estimate diffusional precipitation kinetics. The variation of PE driving force and coarsening rate constant can help correlate the effect of alloying elements and partition temperature on carbide precipitation. The variation of PE driving force for cementite precipitation with composition at a given PT of 400^{o}C is shown in Figure 69(a). Silicon is seen to be most effective in bringing down the DF while manganese and especially carbon increase it. Addition of Mo and Cr brings down the DF marginally. The variation of coarsening rate constant calculated using Kuehmann-Voorhees model [156] in the proprietary CMD software is shown in Figure 69(b). Increasing the amount of carbon and Mo reduces the coarsening rate constant while addition of Si and Mn seem to increase it. Chromium is predicted to be especially effective in reducing the rate constant by

orders of magnitude. The desirable effect of Cr addition in inhibiting carbide precipitation is confirmed by the work of Seo et. al. [69] on a fully austenitized 0.28C-1.5Mn-1.6Si-1Cr alloy partitioned at 400°C for 180s. The Cr addition in this case dramatically reduces the amount of alloy carbon lost to carbides to approximately 15%. However, the same authors showed much higher carbide precipitation despite Cr addition in a 0.2C-4Mn-1.6Si-1Cr steel owing to higher PT of 450°C and longer partition time of 300s [49]. The predicted temperature sensitivity of the PE DF and coarsening rate parameters are summarized in Figure 69(c) and (d).

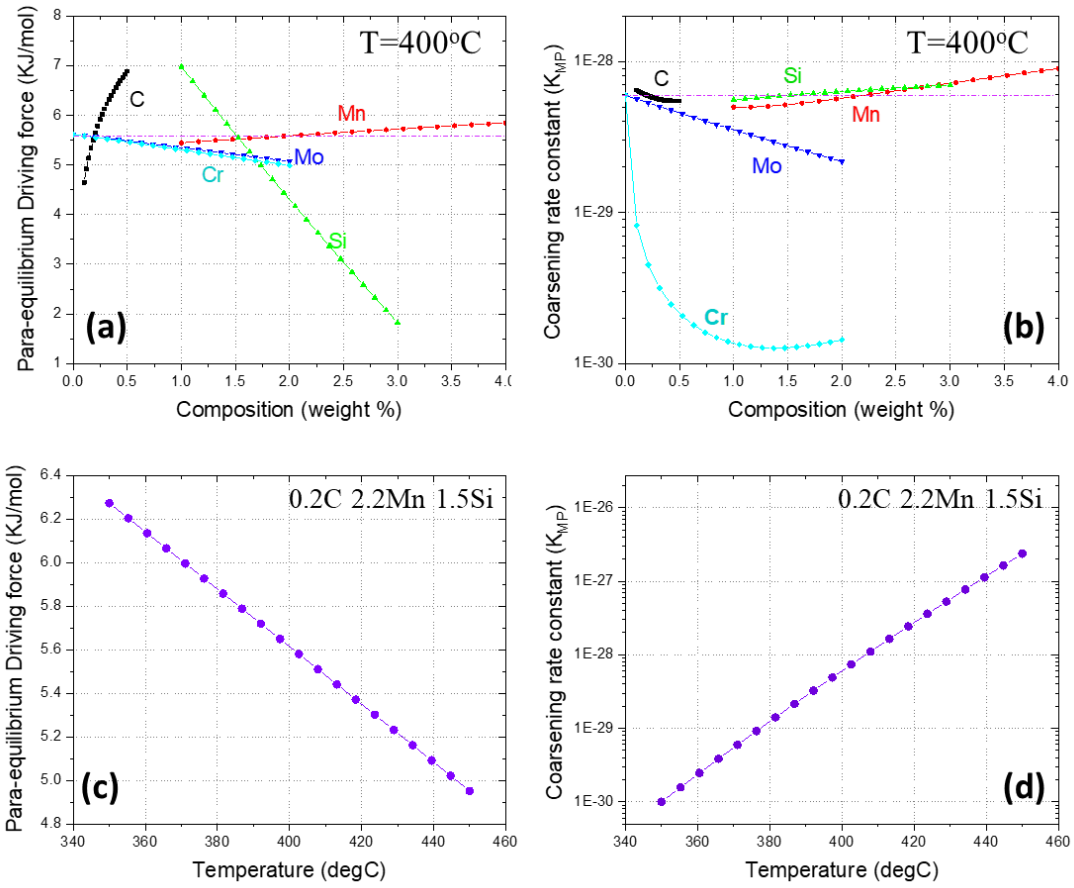

Figure 69 Variation of (a) PE Driving force for cementite precipitation and
(b) Coarsening rate of cementite in BCC as function of composition of alloying elements,
(c) PE driving force of cementite precipitation and
(d) Coarsening rate of cementite in BCC as function of partitioning temperature.
Note: Base condition for all calculations is 0.2C 2.2Mn 1.5Si 0Cr 0Mo at 400°C

The calculated values for PE cementite DF and coarsening rate constant of cementite are tabulated for all alloys and Q&P conditions studied in the current work and the literature Cr-bearing alloys in Table 15. The plot of alloy carbon lost to carbides versus PE cementite DF in Figure 70(a) shows no clear correlation compared to that of coarsening rate constant shown in Figure 70(b). The combined variation with both quantities plotted together is shown in Figure 70(c). As emphasized by the 1Cr alloy, a lower rate constant value is seen to be more effective in bringing down the carbide fraction compared to lower PE cementite DF.

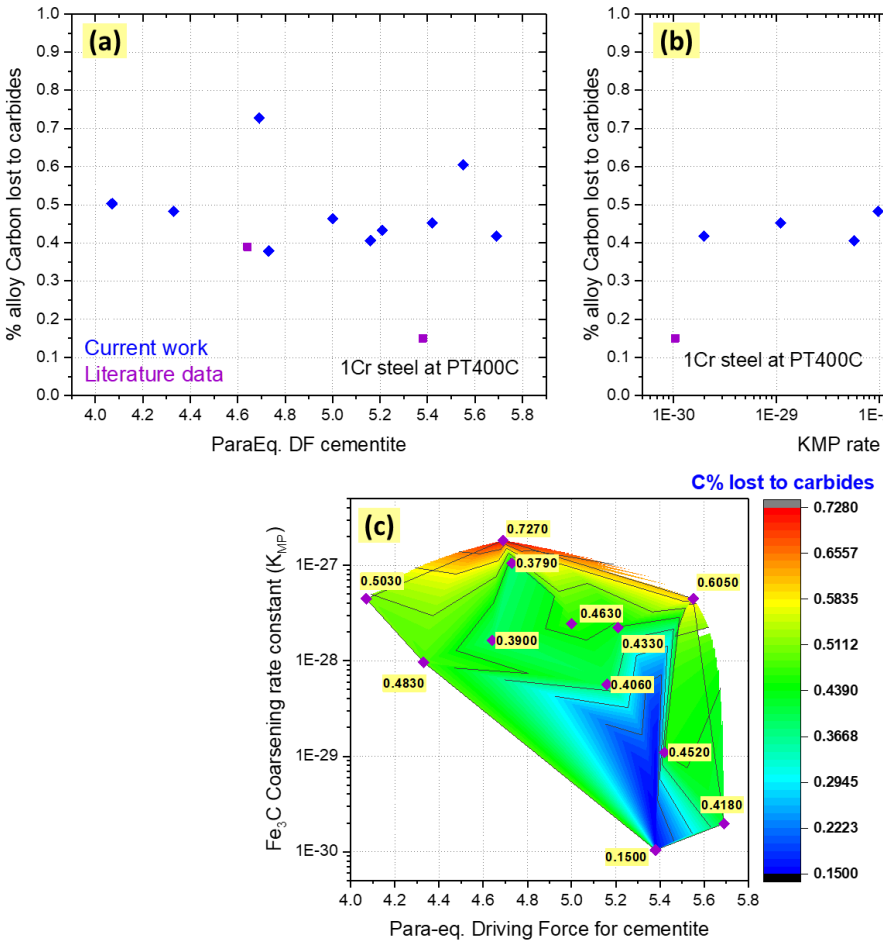

Figure 70 Plot of experimentally calculated fraction of alloy carbon lost to carbides versus calculated values of (a) para-eq DF for cementite precipitation and (b) coarsening rate constant (K_{MP}) of cementite in martensite. (c) Contour filled color map showing the variation of carbide precipitation with change in PE DF and Coarsening rate constant.

4.2. Multiple austenite stability

As noted in the discussion in section 1.4.3, the different factors influencing mechanical austenite stability in Q&P steels include 1) size & morphology, 2) composition, and 3) orientation. A distribution of any one of these factors in the microstructure could potentially result in a distributed austenite stability in the material. In comparison to TRIP steels with ferrite/bainite/austenite constituents, the microstructure of Q&P steels is known to be more inhomogeneous with respect to size and composition of austenite due to the martensitic transformation. The retained austenite in Q&P steels has different morphologies (film-type vs blocky) and possible variation in composition, especially carbon content. These inhomogeneities would impact the austenite stability and thereby the measured ductility.

Multiple specimen tensile tests at different test temperatures were performed on Steel 1 & Steel 2 samples to determine the austenite stability in terms of the Ms^{σ} temperature. Steel 1 and 2 were processed with Q&P cycles of QT270_PT410_100s and QT290_PT420_75s respectively. The measured mechanical properties are plotted against test temperature in Figure 71. The observed Ms^{σ} temperature and peak ductility temperature are marked in the figure. The measured Ms^{σ} temperatures matched closely with the values obtained using the single-specimen Bolling-Richman tests as shown in Figure 72. Previous research efforts in the case of TRIP steels[30] and the QP980 alloy[146], have found the peak ductility temperature to be typically 20 degrees Celsius above the Ms^{σ} temperature. In contrast to these results, the peak ductility measured for the current alloys are found to be well below the Ms^{σ} temperature. One explanation for such behavior could be a bimodal austenite stability in these alloys. The experimentally measured Ms^{σ} temperature corresponds to the least stable austenite while the ductility behavior is influenced by

the combined effect of austenite of all stabilities. Higher stability austenite would eventually transform at lower test temperatures and result in the improved ductility below the measured Ms^{σ} temperature.

The bimodal austenite stability could be due to two possible reasons, 1) the different size or morphology of austenite and/or 2) differences in austenite carbon content. Two different morphology of austenite have clearly been observed in these alloys using electron microscopy with the blocky morphology commonly regarded to have lesser stability compared to the film-type interlath austenite. The second possible reason for different austenite stability would be compositional inhomogeneity in the retained austenite, such as a bimodal distribution in austenite carbon content.

To determine the relative influence of these factors, the microstructure of the tensile tested samples at three different test temperatures were analyzed close to the fracture surface to determine the remaining austenite phase fraction and its carbon content. The chosen test temperatures for both alloys are highlighted by red circles on the uniform elongation values in Figure 71. The measured austenite phase fraction, carbon content and uniform elongation corresponding to the chosen test temperatures are also tabulated in the figure. For the highest chosen test temperature, no significant austenite transformation is noted during tensile testing. The intermediate test temperature samples have a fraction of the austenite with low stability transform during testing while almost the entire austenite transforms to martensite in case of the lowest test temperature samples. The carbon content of the remaining austenite after tensile test was measured to determine the possibility of carbon inhomogeneity. However, the results show slightly higher carbon in Steel 2 and no enrichment in Steel 1 for the intermediate test

temperature samples. This indicates that compositional inhomogeneity is unlikely to be the dominant cause behind bimodal stability of retained austenite. The measured carbon content for the lowest test temperature samples are possibly inaccurate due to extremely low austenite volume fraction. EBSD experiments were also performed on the chosen tensile tested samples of Steel 2 to see the differences in austenite morphology. The OIM phase maps for the three cases are shown in Figure 73. In comparison to sample tested at 68^{o}C, the one tested at 6^{o}C is seen to have a quite reduced fraction of blocky austenite. The sample however contains 3% RA as measured using HEXRD, likely in the form of film-type austenite. Lowering the test temperature increases the driving force for transformation resulting in transformation of less stable blocky austenite at 6^{o}C and both blocky and film-type austenite at -39^{o}C. This would suggest that morphology (film vs blocky) is the dominant reason behind the bimodal austenite stability.

Intensity plots for the chosen tensile tested samples of both alloys obtained from HEXRD experiments are shown in Figure 74. The carbon content of the remaining austenite after tensile testing was estimated using the average lattice parameter measured from the remaining austenite peaks as tabulated at the top of Figure 71. At the lowest test temperature, almost all the retained austenite undergo transformation resulting in only a few low intensity austenite peaks. In both alloys, the remaining austenite peak after testing at the lowest temperature is found to be the (222) austenite peak. The strong residual texture is likely associated with the orientation dependence of austenite mechanical stability.

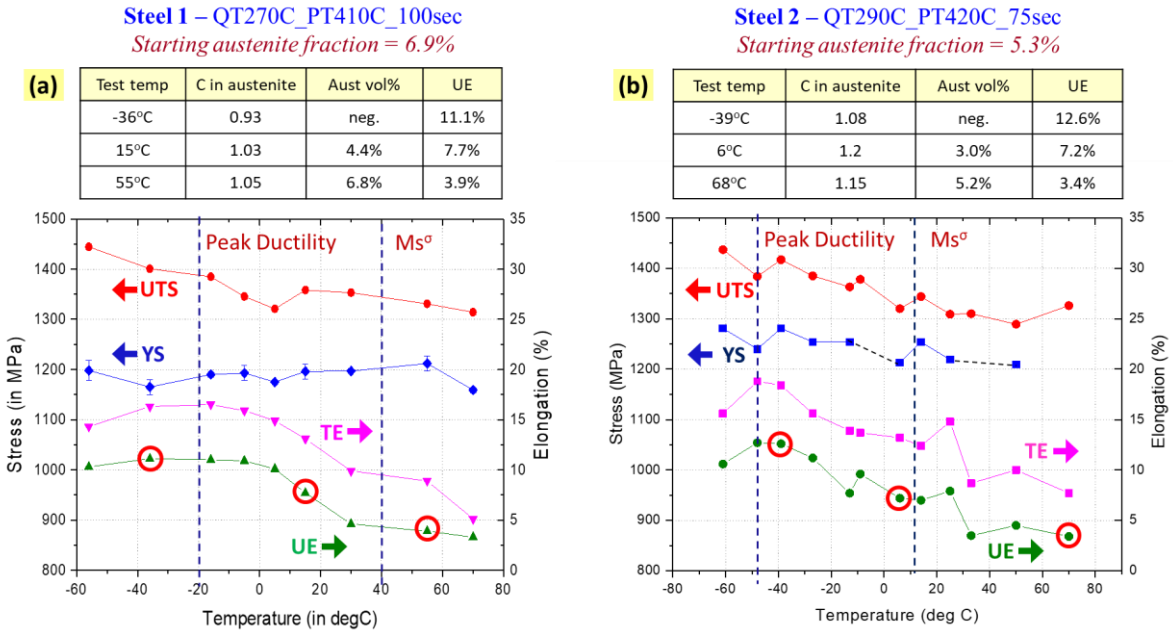

Figure 71 Observed mechanical properties variation with tensile testing temperature for (a)Steel 1 and (b)Steel 2. Also shown above are the austenite carbon content and phase fraction post-failure close to fracture surface at some testing temperatures

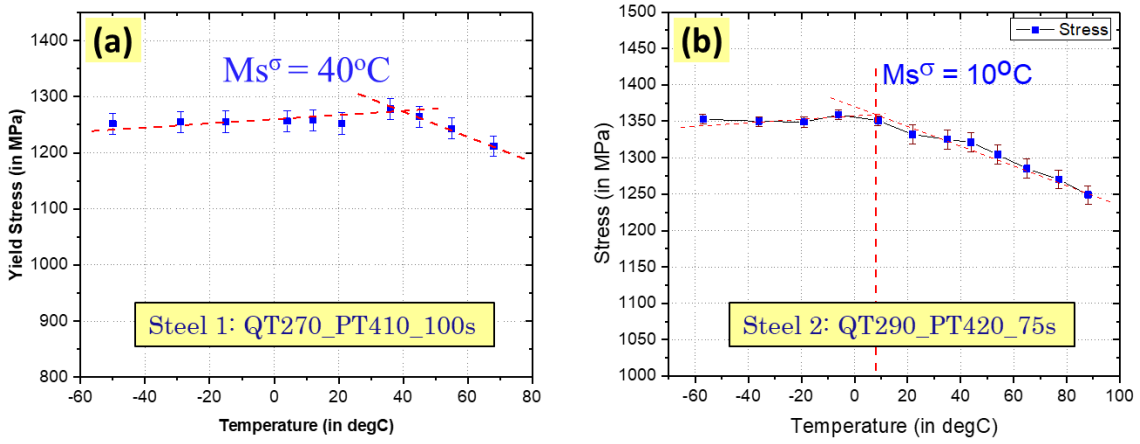

Figure 72 Single specimen tests for measuring Ms^{σ} temperature in case of (a) Steel 1 and (b) Steel 2 with noted Q&P parameters

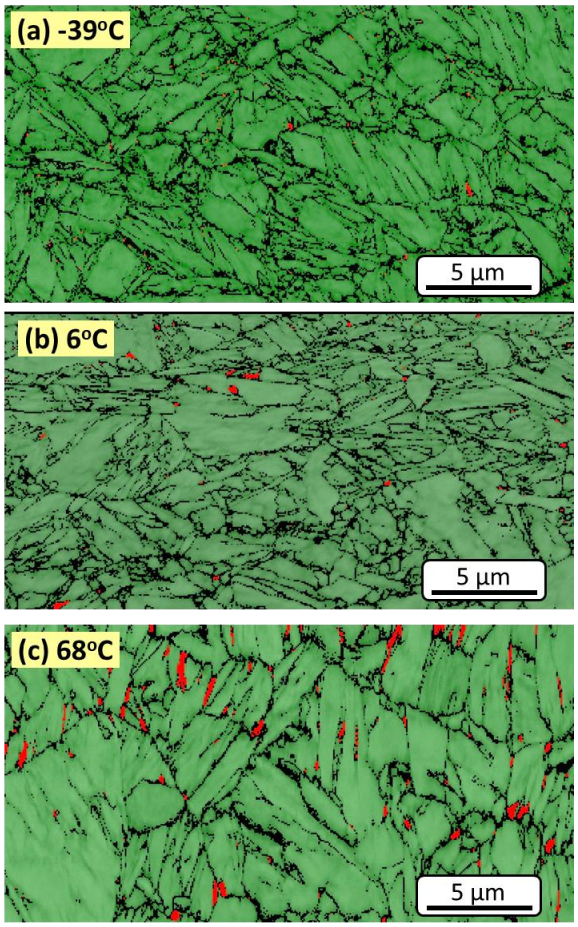

Figure 73: EBSD phase map of Q&P processed Steel 2 samples after undergoing uniaxial tensile testing at (a) -39°C, (b) 6°C, (c) 68°C. The specimens were obtained from close to the fracture surface of the rectangular tensile samples. Red – FCC, Green – BCC.

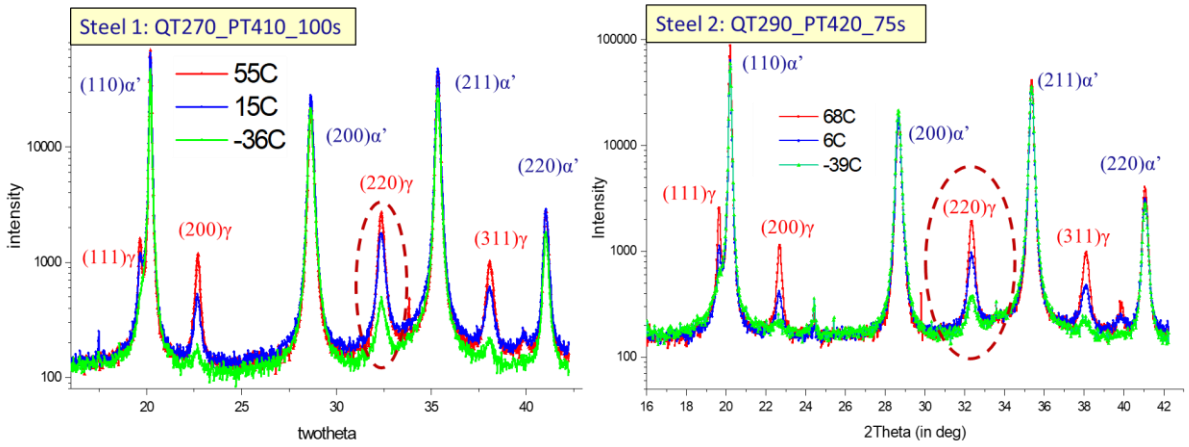

Figure 74 Intensity vs 2Theta angle from HEXRD experiments of samples after tensile testing at different test temperatures in case of (a) Steel 1 and (b) Steel 2

The very different relation between Ms^{σ} temperature and peak ductility temperature for martensite/austenite microstructure compared to the ferrite/bainite/austenite case raises the question of a possible difference in the temperature dependent ductility of martensite. This was investigated by comparing the tensile properties of Q&P processed Steel 130 samples with fully martensitic samples of the same alloy as a function of test temperature. Fully martensitic samples were prepared by quenching the steel from the single-phase austenite region using a liquid nitrogen bath at -190^{o}C. The sample was subsequently reheated to 100^{o}C and isothermally held at that temperature for 1hr to ensure tempering of martensite without any reverse austenite transformation. The variation of measured mechanical properties with test temperature comparing samples are shown in Figure 75(a). The ductility values (TE and UE) for fully martensite sample (denoted with open markers) show no significant variation with test temperature. This confirms that the variation in ductility for Q&P samples with test temperature is due to the TRIP effect in the retained austenite. The dramatic effect of retained austenite on the stress-strain behavior of the steel can be seen in Figure 75(b). Despite the expected relative softness of the austenite, substantial amounts of austenite have little effect on the yield strength. The overall softening effect of TRIP greatly reduces the UTS. The dramatic increase in ductility is associated with the reshaping of the σ-ε curves as shown by the plot of work hardening rate versus true strain at different test temperatures in Figure 76. Q&P samples retain much higher strain hardening at higher strain levels due to TRIP effect, especially at lower test temperatures, reflecting the optimum rate of transformation for flow stabilization. The trend is consistent with the σ-σ "curvature reversing" effect of TRIP previously shown in fully austenite steels.

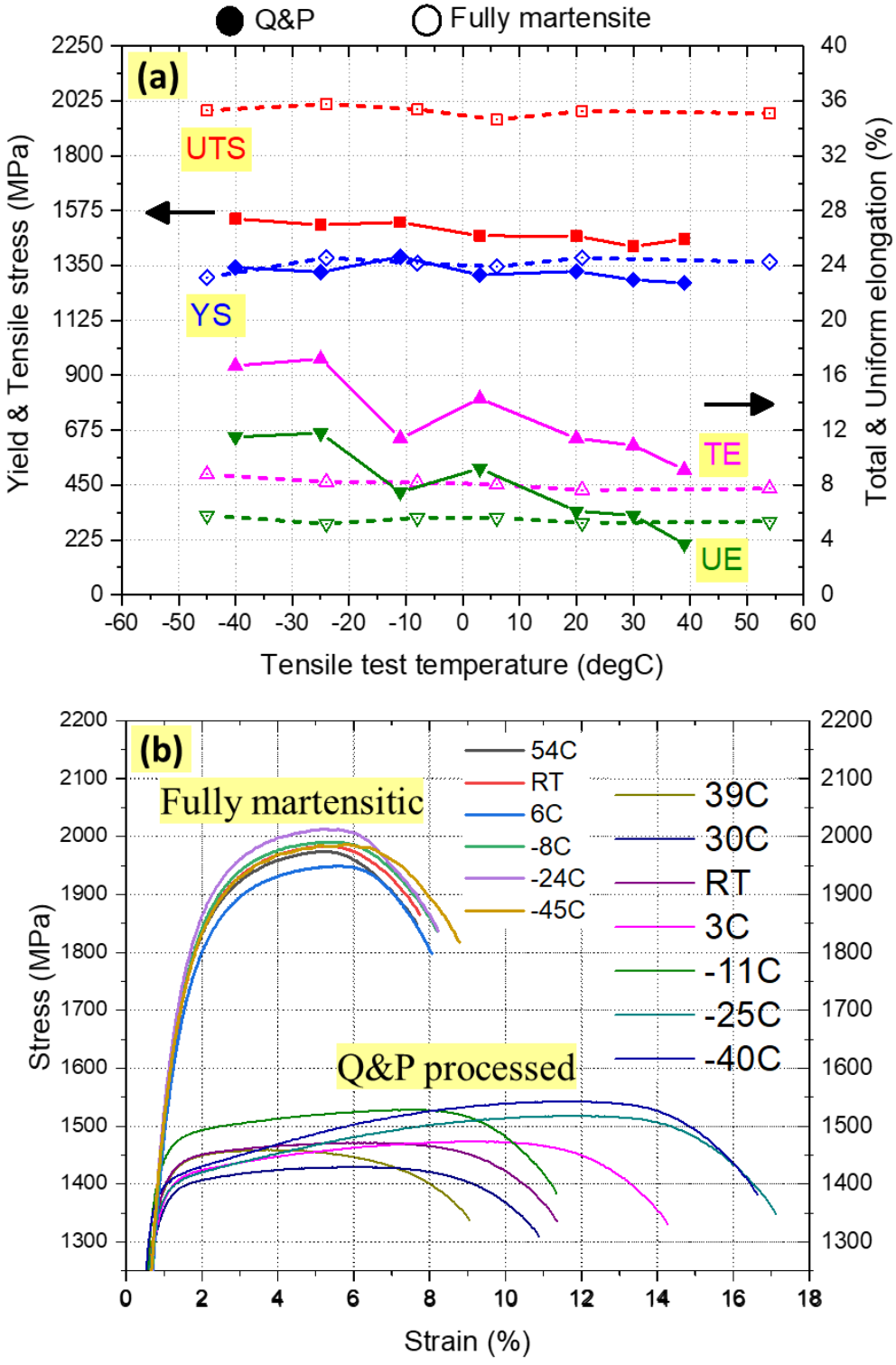

Figure 75 (a) Mechanical properties variation with test temperature and, (b) Engineering stress-strain plots for Q&P processed and fully martensitic specimens of Steel 130

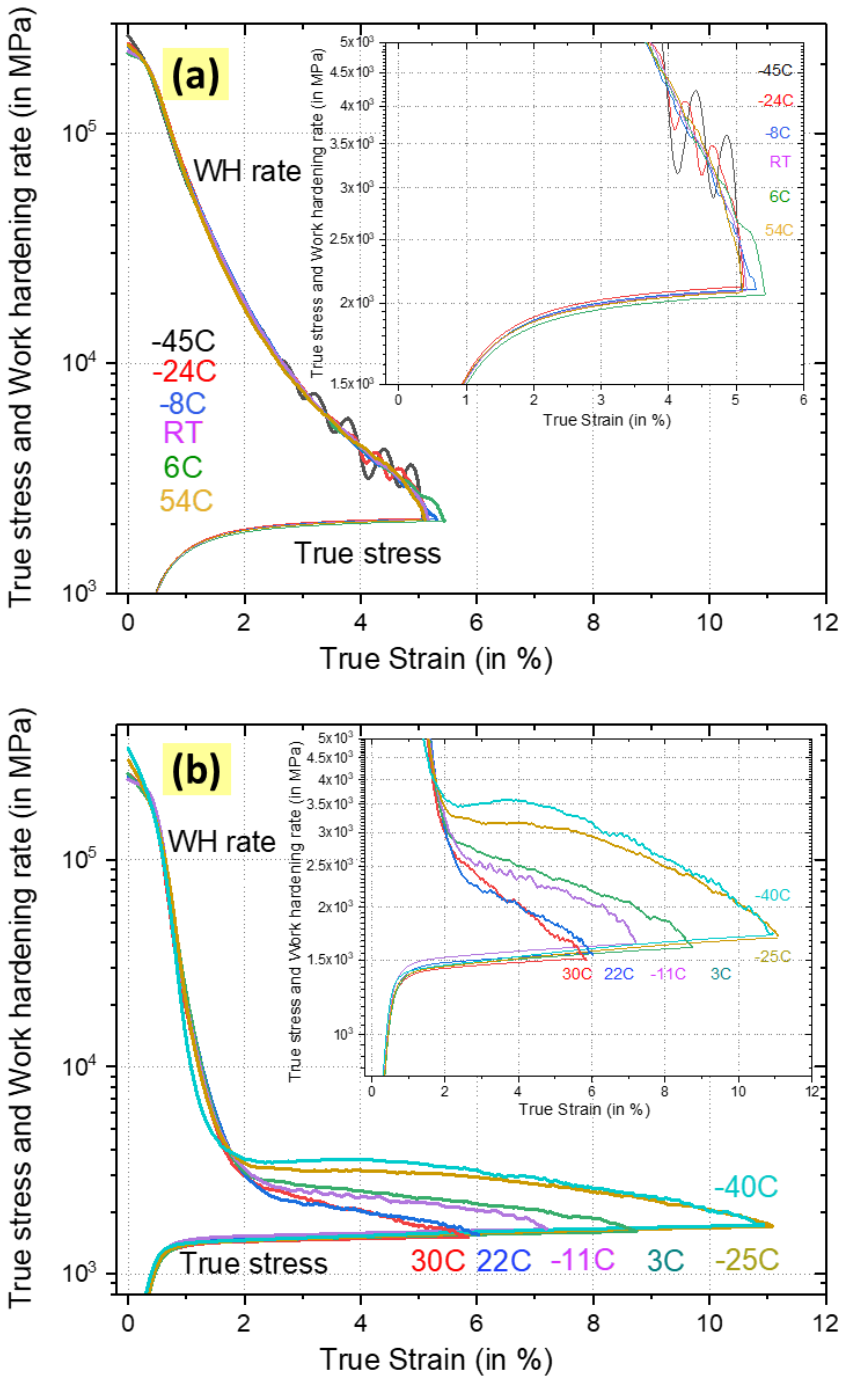

Figure 76 Work hardening rate vs true strain at different test temperatures in case of (a) fully martensitic samples, (b) Q&P processed samples of Steel 130

Chapter 5. Influence of alloy composition and New designed alloys

5.1. Model predicted effect of alloy composition

Thermodynamic models developed in the current work to predict carbon partitioning and austenite stability in Q&P steels were discussed earlier in section 2.3. These models are comprised of physical parameters whose dependence on temperature and composition has been previously established based on mechanistic understanding of the phase transformations and calibrated using experimental measurements. The use of these physical parameters enables the developed models to be truly predictive for composition and processing condition ranges beyond those used in their calibration. Model predictions of the variation of austenite carbon content and its stability in terms of Ms^{σ} temperature as a function of alloy composition are shown in Figure 77(a) and Figure 77(b). The effect of partition temperature on both quantities for a given alloy composition is also shown in Figure 77(c).

Addition of Mn and Cr decreases the austenite carbon content while addition of Si and Mo do not make significant changes to it. The addition of any alloying element is observed to decrease the carbon partitioned to austenite and thereby decreases the austenite stability marked by higher Ms^{σ} temperatures. Carbon and Manganese are seen to have the most impact on carbon partitioning and consequently austenite stability. While Mn is commonly assumed to raise austenite stability in these steels, the model clearly shows that Mn is a strong austenite destabilizer under Q&P processing conditions. This comes from a combination of its effect on Paraequilibrium thermodynamics of carbon, and its strong contribution to the W_F^{SS} solution hardening term in the total effective stored energy.

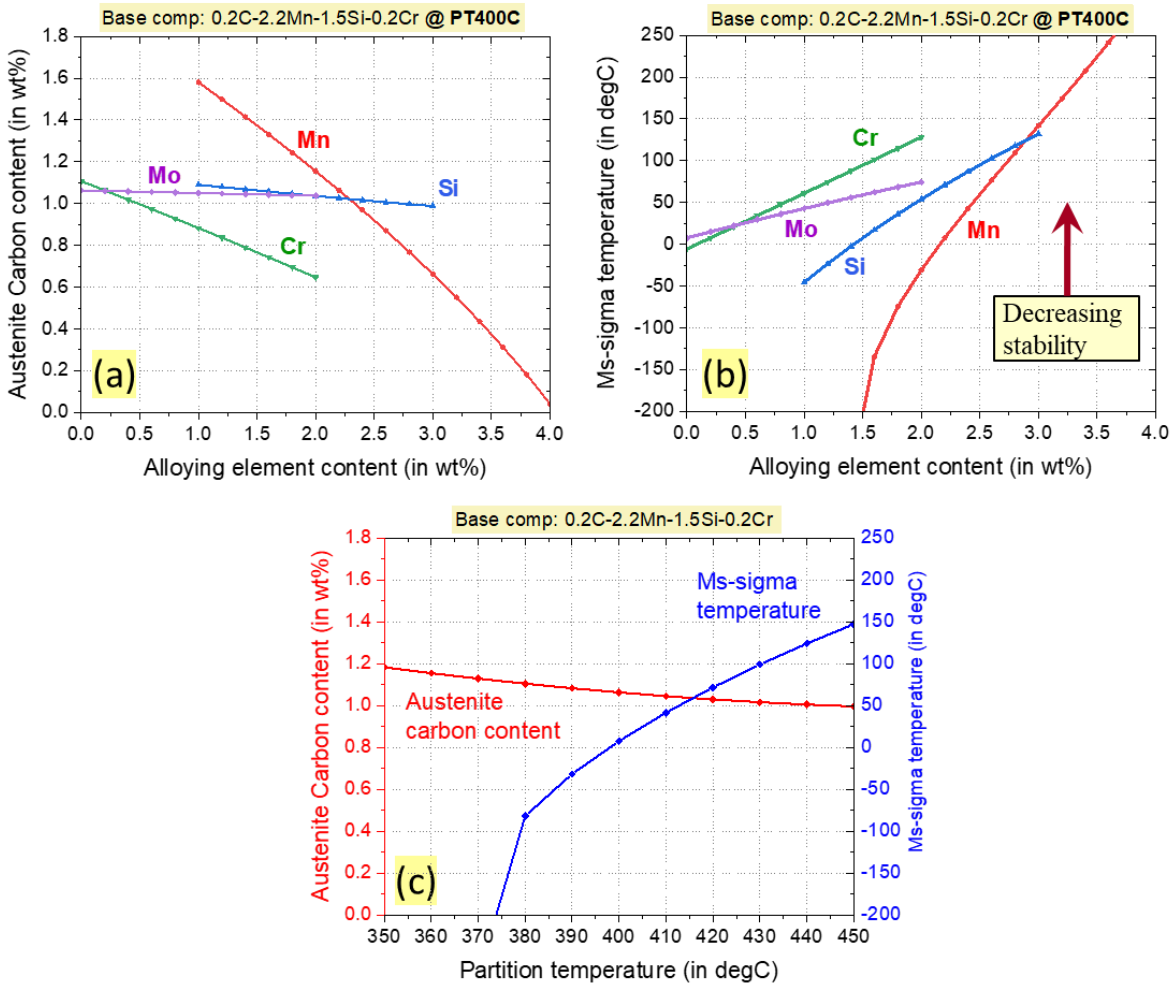

Figure 77: Influence of alloy composition on (a) Austenite carbon content and (b) Ms-sigma temperature as predicted by the thermodynamic models developed in current work.

5.2. New designed alloys and Q&P cycles

The microstructural analysis and measured mechanical properties of Q&P processed Steel 1 samples with different PT were utilized to develop the thermodynamic models to predict carbon partitioning and austenite stability as functions of alloy composition and PT. These models along with the previously discussed thermodynamic parameters to control carbide precipitation were used to design a set of 7 new alloy compositions and corresponding Q&P cycles to further validate the developed models and achieve higher performance levels. These steels were designated as Steel 121-130 with their compositions listed in Table 6. The alloy compositions were decided with the aim of reducing Mn addition to the steel as it is predicted to increase the para-equilibrium driving force for cementite precipitation. The decrease in alloy hardenability and austenite stability due to Mn reduction were compensated by increasing the alloy carbon content and/or by the addition of B, Ti to the alloy. Steel 121 to 123 were designed to incrementally reduce Mn content while increasing C content to see its impact on austenite stability and carbide precipitation. The impact of Cu/Ni addition on improving the strength levels of Q&P steels by Cu precipitation strengthening and their influence on austenite stability were investigated with Steel 124, 125. Steel 126, 130 are alloys with reduced Mn content but without B/Ti addition to improve hardenability. Individually optimized Q&P processing cycles for maximizing ductility were determined for each alloy composition and are listed in Table 16. All the alloys were fully austenitized and quenched to a QT chosen to have ~80% of martensite formed upon initial quenching. The chosen PT ensures optimal austenite stability to provide peak ductility at room temperature. The P-time was chosen as the shortest time required to ensure compositional homogeneity in austenite while avoiding excess carbide precipitation.

5.2.1. Microstructure and mechanical properties

Dilatometer experiments were performed to investigate the phase transformation behavior occurring during Q&P processing of all the designed alloys. Figure 78 plots change in length against temperature for all the 7 designed alloys. The reduction in length during initial heating stage starting around 750^{o}C is due to the BCC to FCC transformation. The transformation in some cases reaches close to completion during the heating stage which is marked by the curve regaining its upwards slope because of thermal expansion. In other cases, transformation continues during isothermal holding marked by the decrease in length at the austenitization temperature of 930^{o}C. Austenitization is seen to be complete or very close to completion in all cases except Steel 122. Low carbon and manganese content of Steel 122 results in a higher Ac3 temperature that doesn't allow complete austenitization at 930^{o}C for 180s. Other than Steel 126, no other alloy showed signs of ferrite or bainite transformation during the quenching step. Due to its low manganese content and absence of any B/Ti addition, Steel 126 has insufficient hardenability and undergoes ferrite transformation during quenching starting around 800^{o}C. The abrupt increase in length close to 350^{o}C in all the alloys is due to onset of martensitic transformation. The increase in length at PT again corresponds to continuing BCC transformation in the remaining austenite along with carbon partitioning. No significant fresh martensite formation is seen in any of the alloys during the final quenching step. Based on dilatometer results, the final microstructure in all cases except Steel 122 and 126 are expected to be close to the desired Q&P microstructure consisting of tempered martensite and retained austenite.

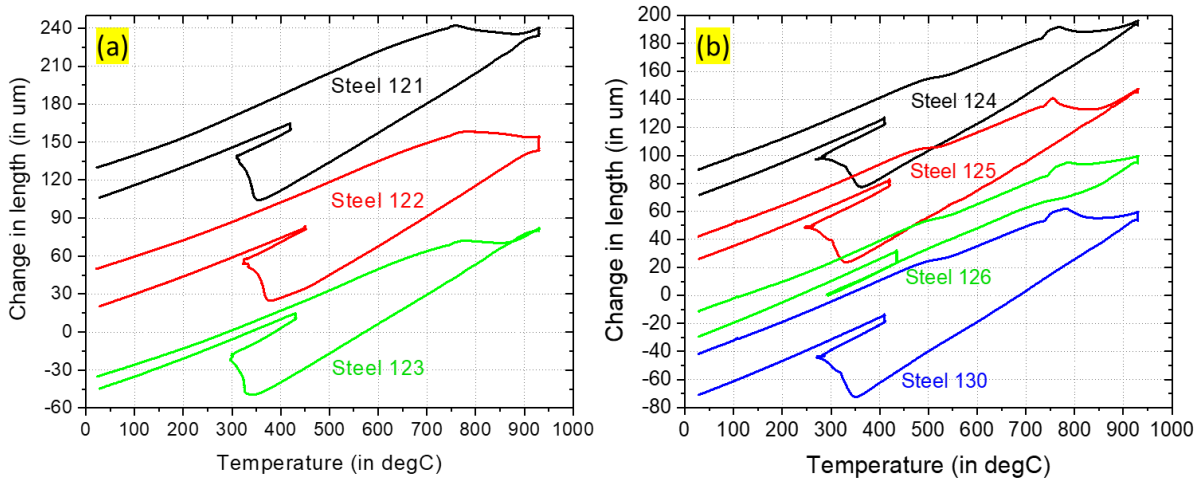

Figure 78: Dilatometer experiment results showing change in length versus temperature during Q&P cycle for (a) Steel 121, 122, 123, (b) Steel 124, 125, 126, 130

SEM micrographs of the Q&P processed samples after light nital etching are shown in Figure 79 and Figure 80. The incomplete austenitization of the low-Mn Steel 122 is confirmed by the significant amount of intercritical ferrite in the microstructure. A fraction of the remaining austenite undergoes martensitic transformation during the quenching step. The microstructure in steel 121 and 123 consists predominantly of martensite along with some amount of retained austenite and carbides. In the case of Steel 124 and 125, the microstructure consists primarily of martensite with small amount of intercritical ferrite mostly found close to the prior austenite grain boundaries. Low hardenability of Steel 126 results in ferrite and/or bainite transformation in the austenite during the quenching step. The remaining austenite undergoes bainite transformation during the partitioning step and fresh martensite transformation during final quenching step. The final microstructure is thereby seen to consist of ferrite, bainite, retained austenite and fresh martensite. The microstructure for steel 130 is much closer to the desired

Q&P microstructure consisting of tempered martensite and retained austenite along with some fraction of carbides.

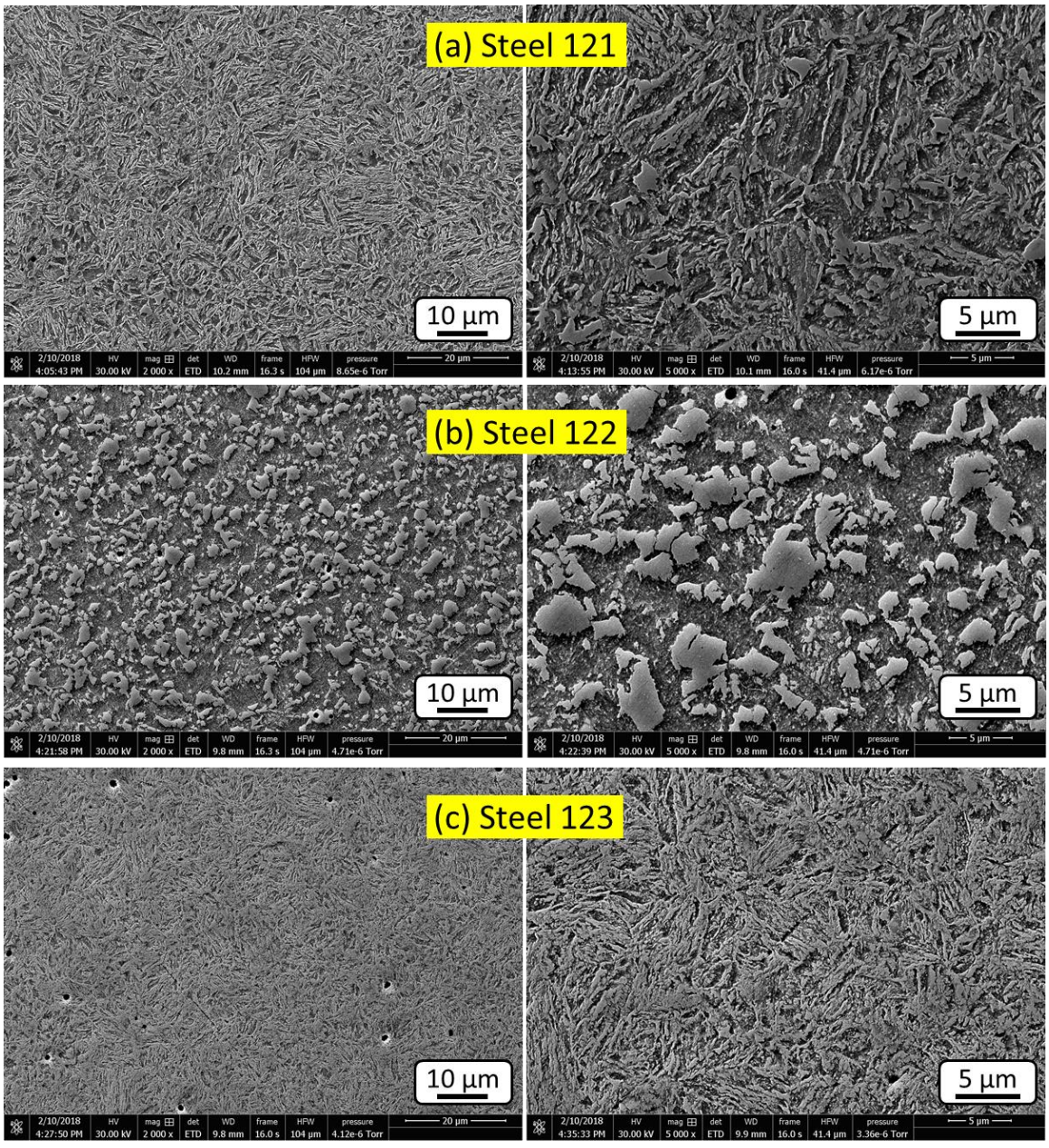

Figure 79: SEM images after Q&P processing of (a) Steel 121, (b) Steel 122, (c) Steel 123

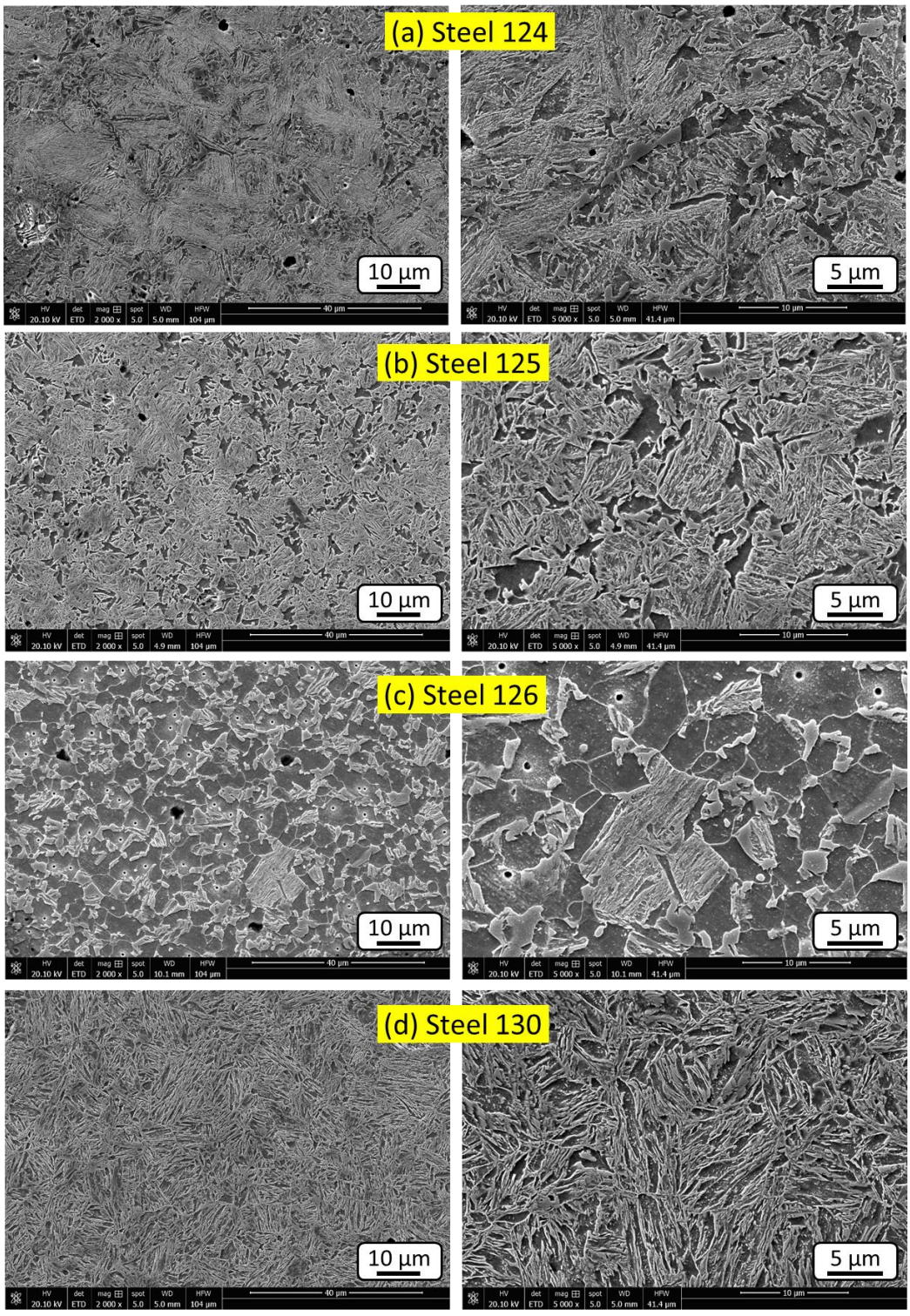

Figure 80: SEM micrographs after Q&P processing of
(a) Steel 124, (b) Steel 125, (c) Steel 126, (d) Steel 130

HEXRD experiments were performed to determine the austenite phase fraction and its carbon content for all the designed alloys. The measured values along with the measured mechanical properties of the alloys are listed in Table 16. The retained austenite fraction is the least in the case of the alloy with low C and Mn alloying additions. The individual engineering stress-strain plots for the alloys are plotted in Figure 81. Steel 126 has lower strength and higher ductility due to the high phase fraction of intercritical ferrite in the microstructure. The addition of Cu/Ni does not improve the alloy strength, attributed to insufficient time at the PT for copper precipitation. The improvement in ductility due to the TRIP effect in the retained austenite is confirmed by the curvature of the strain hardening rate plots shown in Figure 82. Steel 121 and 124 are found to have the best ductility with uniform elongation close to 10%.

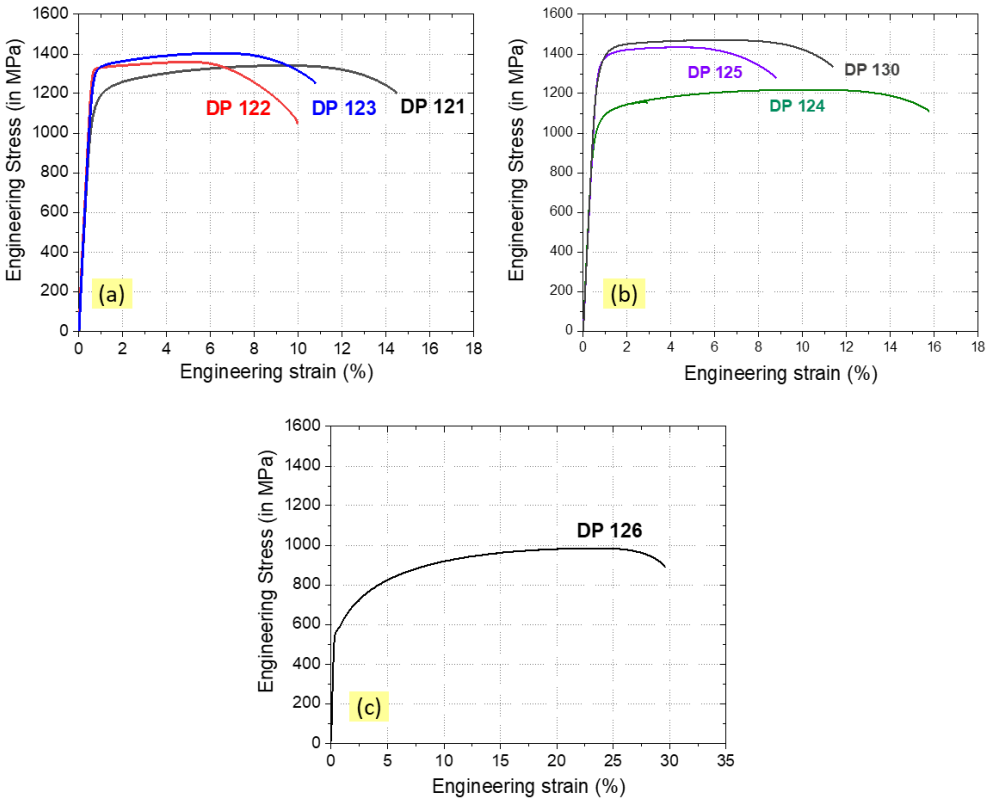

Figure 81 Engineering stress-strain plots for new prototype alloys
(a) Steel 121, 122, 123, (b) Steel 124, 125, 130, (c) Steel 126

Table 16 Q&P cycles for new prototype steels with observed austenite phase fraction, carbon content and alloy mechanical properties

	QT (ºC)	PT (ºC)	Ptime (sec)	Aust (%)	C_{Aust} (wt%)	0.2 YS (MPa)	UTS (MPa)	TE (%)	UE (%)
Steel 121	310	420	75	6.5	1.17	1116	1342	14.5	9.3
Steel 122	325	450	60	1.1	1.36	1326	1360	10	5.2
Steel 123	300	430	75	5.6	1.44	1310	1404	10.8	6.4
Steel 124	275	410	250	14.4	1.4	1007	1220	15.7	10.3
Steel 125	250	420	250	11.8	1.79	1350	1434	8.8	4.2
Steel 126	295	435	75	22.9	1.398	567	985	29.6	23.5
Steel 130	275	410	100	7.5	1.23	1325	1471	11.4	6.1

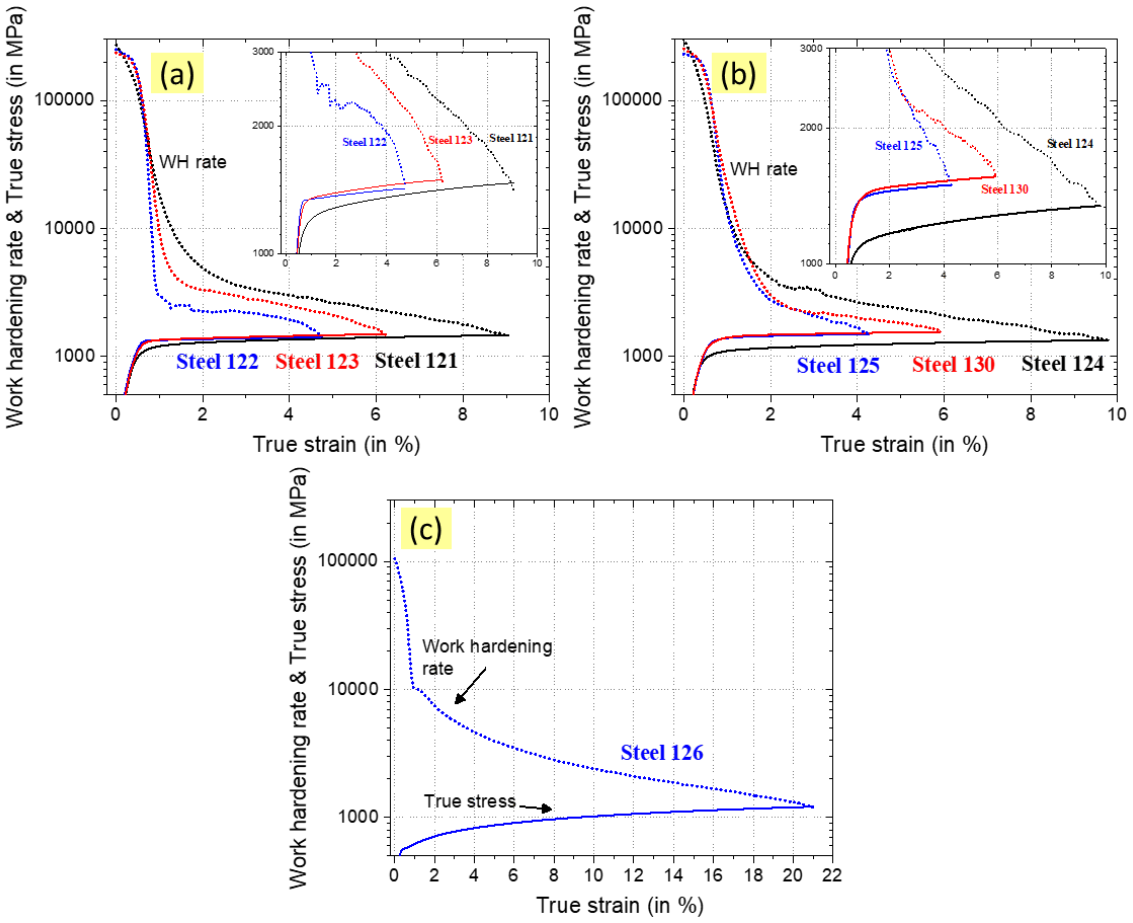

Figure 82: Work hardening rate and true stress plotted versus true strain in case of RT tensile tests for (a) Steel 121, 122, 123, (b) Steel 124, 125, 130, (c) Steel 126

5.2.2. Experimental validation of developed thermodynamic models

The designed alloys were evaluated to validate the developed models for carbon partitioning and austenite stability. Table 17 lists the measured and model predicted values for austenite carbon content and the austenite stability (Ms^{σ} temperature). The austenite carbon content was measured for all the alloys, while Ms^{σ} temperature was not measured in the case of Q&P processing performed only by dilatometer. The measured and predicted values plotted in Figure 83 establish that the models can reliably predict the austenite carbon content and its associated stability. The error bar noted in austenite carbon measurements is from the difference between lattice parameter measurements from 4 austenite peaks while error in Ms^{σ} temperature is an average error of estimation due to fitting of peaks in yield stress versus temperature plots.

Table 17: New designed alloy compositions and their optimal Q&P cycle parameters. Experimental measurements and modeling pedictions for austenite carbon content and its associated stability.

Steel No.	Alloy composition (wt%)	QT (°C)	PT (°C)	Ptime (sec)	Aust. fraction (%)	C_{Aust} HEXRD (wt%)	C_{Aust} model (wt%)	Ms^{σ} exper. (°C)	Ms^{σ} model (°C)
2	0.18C 2Mn 1.55Si 0.15Mo	290	420	75	5.3	1.11	1.18	15	28
2	0.18C 2Mn 1.55Si 0.15Mo	290	440	60	6.9	1.08	1.15	-	-
121	0.2C 1.8Mn 1.5Si 0.2Mo (+ B,Ti)	310	420	75	6.5	1.17	1.25	5	6
122	0.2C 1Mn 1.5Si 0.2Mo (+ B,Ti)	325	450	60	1.1	1.36	1.52	-	-
123	0.3C 1Mn 1.5Si 0.2Mo (+ B,Ti)	300	430	75	5.6	1.44	1.41	10	-10
130	0.25C 1.5Mn 2Si 0.2Mo	275	410	100	7.5	1.23	1.29	-5	-7
130	0.25C 1.5Mn 2Si 0.2Mo	275	430	60	7.5	1.16	1.26	-	-

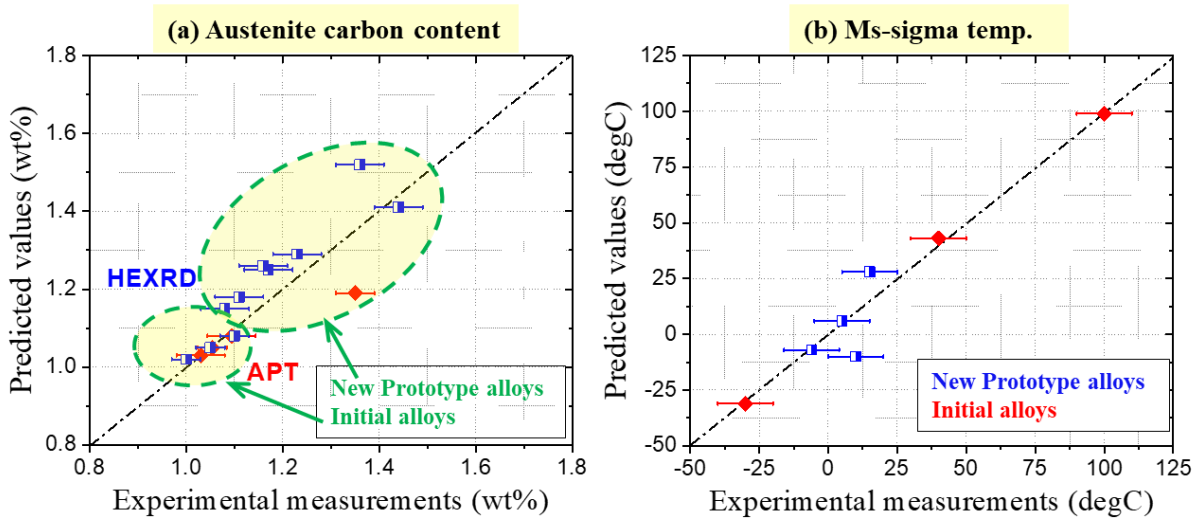

Figure 83: Predicted values versus experimental measurements for (a) Austenite carbon content, (b) Austenite stability in terms of its Ms^{σ} temperature

5.3. New optimized Q&P cycles considering multiple austenite stability

The observations of multiple austenite stability in most of the currently studied Q&P alloys suggest the possibility of further improvement in mechanical properties by changing the processing parameters to ensure optimal stability for the maximum austenite fraction instead of the least stable fraction. New Q&P cycles for Steel 130 alloy with PT of 430^{o}C and P-time of 60s were designed aiming to bring the ductility peak at low temperature (as shown in Figure 75(a)) corresponding to higher stability austenite closer to room temperature. The samples were first prepared in the dilatometer and evaluated for phase composition. The austenite carbon content was measured to be 1.163 wt% at PT of 430^{o}C compared to 1.23 wt% at PT of 410^{o}C. The results confirm lower austenite carbon content and overall austenite stability by increasing the PT. Standard ASTM subsize specimens are currently under preparation to be tested for their mechanical properties and austenite stability.

Chapter 6. Summary and proposed future work

The current work involved microstructural characterization of a set of low carbon TRIP steels subjected to Q&P heat cycles with varying process parameters. The influence of alloy composition and three processing parameters; partition temperature (PT), partition time (Ptime) and quench temperature (QT) on the microstructure was thoroughly investigated. Electron microscopy was utilized to identify microstructural constituents and determine the distribution of microstructural phases. High energy x-ray diffraction and atom probe tomography were used to accurately determine individual phase fractions and their compositions. Dilatometer studies were carried out to quantify phase transformations occurring during Q&P processing. Mechanical properties of the alloys and the austenite stability in the final microstructure were evaluated using uniaxial tensile tests. Thermodynamics-based mechanistic models based on the theory of coupled diffusional/displacive transformation were calibrated to predict the austenite carbon content and retained austenite stability in the final Q&P microstructure. The models were validated using a set of new designed alloys subjected to individually optimized Q&P processing.

The main conclusions drawn from the work can be summarized as follows:

1. Consistent with previous studies, the microstructure after fully austenitic Q&P processing of low carbon TRIP steels consisted mainly of tempered martensite and carbon enriched retained austenite, with typically some amount of bainite transformation and carbide precipitation occurring during the partitioning step. 3DAPT experiments along with HEXRD measurements quantified carbon enrichment in the austenite phase and depletion in the martensite phase along with significant loss (40-50%) of alloy carbon in the form of carbides.

2. Final austenite carbon content is confirmed to vary most strongly with partitioning temperature (PT), with higher carbon content at lower PT. Based on the theory of coupled diffusional/displacive transformation a carbon partitioning model using para-equilibrium simulations with added temperature-dependent 'effective stored energy' contribution was developed to predict the austenite carbon content taking into account both stored and dissipated energies associated with displacive interfacial motion. Dependence of the effective stored energy on PT and alloy composition was established. The variation of stored energy with PT was consistent with the difference in the forest dislocation density ahead of the moving austenite/martensite interface as affected by dislocation recovery. The developed carbon partitioning model was validated with measurements from a set of new designed alloys subjected to individually optimized Q&P cycles.
3. The stability of the retained austenite in the final Q&P microstructure was quantified in terms of the characteristic Ms^{σ} temperature below which transformation controls yielding. Experimental measurements of the Ms^{σ} temperature using uniaxial tensile tests confirmed systematic variation of austenite stability with austenite carbon content and therefore with PT. Lower PT resulted in higher austenite carbon content yielding higher austenite stability as represented by lower Ms^{σ} temperature. Based on martensite nucleation theory, an austenite stability model to thermodynamically calculate the Ms^{σ} temperature was calibrated for Q&P steels, defining the critical free energy (ΔG_{crit}) required for martensite transformation and its dependence on PT and alloy composition. The variation of critical free energy with PT was correlated to the change in forest dislocation density during the partitioning step and the potency of nucleation sites in the

retained austenite was identified. The developed stability model was also validated with Ms^{σ} measurements on the set of new designed alloy compositions.

4. A smaller variation of final austenite carbon content with initial quench temperature (QT) was determined using measurements from one chosen alloy composition. Carbon enrichment in austenite was established to be dependent on the direction of movement of the austenite/martensite interface in association with a sign reversal of the contribution of interfacial dissipation to the effective BCC stored energy. Reversal of the direction of interface movement towards the martensite phase (BCC -> FCC transformation) resulted in higher carbon partitioning but also led to more carbide precipitation in association with the higher initial martensite content.
5. Consistent with DICTRA diffusion simulations, the effect of partition time on carbon partitioning was also confirmed using HEXRD experiments. The austenite carbon content increased initially to reach a peak value at the predicted time scale, after which it decreased with further increase in time attributed to the effect of carbide precipitation.
6. Carbide precipitation in the final Q&P microstructure was confirmed by SEM, HEXRD and 3DAPT experiments. Carbide precipitates were found to be slightly enriched in manganese and depleted in silicon. The silicon content of the carbides was closer to para-cementite compared to predicted full-equilibrium cementite. The variation of amount of carbide precipitation was correlated with the variation in two parameters: 1) Para-equilibrium driving force for cementite formation and, 2) Coarsening rate constant for cementite inside martensite. The correlation predicts the most effective alloying element

in delaying carbide precipitation during Q&P processing is Cr, as supported by available literature data.

7. The existence of multiple austenite stability in the retained austenite was confirmed via multiple specimen tensile tests at varying test temperatures. The cause of multiple stability was attributed to the presence of two different morphologies in the retained austenite i.e. blocky vs film-type.
8. The models calibrated in the current work for carbon partitioning and austenite stability can be used together to determine the optimal fully austenitic Q&P cycle for any given alloy composition. The optimal heat treatment would ensure the maximum benefit to uniform elongation from TRIP effect in the retained austenite and thus result in the best possible combination of strength and ductility for any given composition.

Suggested ideas for future efforts in continuation of the current work could include:

1) Validate the predicted effect of QT on the retained austenite stability by performing single specimen and multiple specimen tensile tests at different test temperatures.
2) Utilize newer characterization instruments to accurately determine the change in carbide precipitation with processing parameters i.e. QT, PT and Ptime. Correlate the observed differences with fundamental parameters to be able to better control carbide precipitation behavior.
3) Perform experimental studies on currently investigated alloys processed with modified Q&P cycles to bring the peak ductility observed in multiple specimen tensile tests to material use temperature or room temperature.

4) Based on the carbide kinetic correlations, explore Cr-modified compositions to greatly reduce competing carbide precipitation and achieve Q&P martensite/austenite steels with greater amounts of optimal stability austenite for greater TRIP-enabled performance.

References

1. Keeler, S.; Kimchi, M. Advanced High-Strength Steels Application Guidlines Version 5.0. *WorldAutoSteel* **2014**.
2. Tamarelli, C. M. The evolving use of advanced high-strength steels for automotive applications. *Steel martket Dev. institute, Autosteel* **2011**.
3. Matlock, D. K.; Speer, J. G.; De Moor, E.; Gibbs, P. J. Recent developments in advanced high strength sheet steels for automotive applications: an overview. *Jestech* **2012**, *15*, 1–12.
4. Zackay, V. F.; Parker, E. R.; Fahr, D.; Busch, R. The enhancement of ductility in high strength steels. *Trans. ASM* **1967**, *60*, 252–259.
5. Bhandarkar, D.; Zackay, V.; Parker, E. Stability and mechanical properties of some metastable austenitic steels. *Metall. Mater. Trans. B* **1972**, *3*, 2619–2631, doi:10.1007/BF02644238.
6. Schultz, R. A.; Abraham, A. K. Metallic Material Trends For North American Light Vehicles. *Ducker Worldwide, Gt. Des. Steel Semin.* **2011**.
7. Olson, G. B. Transformation Plasticity and the Stability of Plastic Flow. In *Deformation, processing and structure*; G. Krauss, Ed.; ASM Materials science, 1984; pp. 391–424 ISBN 0871701758.
8. Sun, F.; Zhang, J. Y.; Marteleur, M.; Gloriant, T.; Vermaut, P.; Laillé, D.; Castany, P.; Curfs, C.; Jacques, P. J.; Prima, F. Investigation of early stage deformation mechanisms in a metastable β titanium alloy showing combined twinning-induced plasticity and transformation-induced plasticity effects. *Acta Mater.* **2013**, *61*, 6406–6417, doi:10.1016/J.ACTAMAT.2013.07.019.
9. Olson, G. B. Mechanically-induced phase transformations in alloys. *Encycl. Mater. Sci. Eng.* **1986**, 2929–2932.
10. Jacques, P. J. Transformation-induced plasticity for high strength formable steels. *Curr. Opin. Solid State Mater. Sci.* **2004**, *8*, 259–265, doi:10.1016/j.cossms.2004.09.006.
11. Olson, G. B.; Azrin, M. Transformation Behavior of TRIP steels. *Metall. Trans. A* **1978**, *9*, 713–721, doi:10.1007/BF02659928.
12. Pereloma, E.; Gazder, A.; Timokhina, I. Retained Austenite: Transformation-Induced Plasticity. In *Encyclopedia of Iron, Steel, and Their Alloys*; CRC Press, 2016; pp. 3088–3103 ISBN 9781466511040.
13. Olson, G. B.; Cohen, M. A general mechanism of martensitic nucleation: Part I. General concepts and the FCC → HCP transformation. *Metall. Trans. A* **1976**, *7*, 1897–1904, doi:10.1007/BF02659822.
14. Olson, G. B.; Cohen, M. Stress-assisted isothermal martensitic transformation: Application to TRIP steels. *Metall. Trans. A* **1982**, *13*, 1907–1914, doi:10.1007/BF02645934.
15. Olson, G. B.; Cohen, M. Kinetics of strain-induced martensitic nucleation. *Metall. Trans.*

A **1975**, *6*, 791–795, doi:10.1007/BF02672301.

16. Narutani, T.; Olson, G. B.; Cohen, M. Constitutive Flow Relations for Austenitic Steels During Straininduced Martensitic Transformation. *Le J. Phys. Colloq.* **1982**, *43*, C4-429-C4-434, doi:10.1051/jphyscol:1982465.
17. Stringfellow, R. G.; Parks, D. M.; Olson, G. B. A constitutive model for transformation plasticity accompanying strain-induced martensitic transformations in metastable austenitic steels. *Acta Metall. Mater.* **1992**, *40*, 1703–1716, doi:10.1016/0956-7151(92)90114-T.
18. Demeri, M. Y. *Advanced High-strength Steels: Science, Technology, and Applications*; 2013; ISBN 1627080058.
19. Wang, J.; van der Zwaag, S. Stabilization Mechanisms of Retained Austenite in Transformation-Induced Plasticity Steel. *Metall. Mater. Trans. A* **2001**, *32*, 1527–1539, doi:10.1007/s11661-001-0240-5.
20. Blondé, R.; Jimenez-Melero, E.; Zhao, L.; Wright, J. P.; Brück, E.; Van Der Zwaag, S.; Van Dijk, N. H. High-energy X-ray diffraction study on the temperature-dependent mechanical stability of retained austenite in low-alloyed TRIP steels. *Acta Mater.* **2012**, *60*, 565–577, doi:10.1016/j.actamat.2011.10.019.
21. Jimenez-Melero, E.; van Dijk, N. H.; Zhao, L.; Sietsma, J.; Offerman, S. E.; Wright, J. P.; van der Zwaag, S. Characterization of individual retained austenite grains and their stability in low-alloyed TRIP steels. *Acta Mater.* **2007**, *55*, 6713–6723, doi:10.1016/j.actamat.2007.08.040.
22. Chiang, J.; Lawrence, B.; Boyd, J. D.; Pilkey, A. K. Effect of microstructure on retained austenite stability and work hardening of TRIP steels. *Mater. Sci. Eng. A* **2011**, *528*, 4516–4521, doi:10.1016/j.msea.2011.02.032.
23. Sugimoto, K.; Misu, M.; Kobayashi, M.; Shirasawa, H. Effects of second Phase Morphology on Retained Austenite Morphology and Tensile Properties in a Trip-Aided Dual-Phase Steel Sheet. *ISIJ Int.* **1993**, *33*, 775–782, doi:10.2355/isijinternational.33.775.
24. Koh-ichi Sugimoto, Akinobu Kanda, Ryo Kikuchi, Shun-ichi Hashimoto, Takahiro Kashima, S. I. Ductility and Formability of Newly Developed High Strength Low Alloy TRIP-aided Sheet Steels with Annealed Martensite Matrix.
25. Zhang, S.; Findley, K. O. Quantitative assessment of the effects of microstructure on the stability of retained austenite in TRIP steels. *Acta Mater.* **2013**, *61*, 1895–1903, doi:10.1016/j.actamat.2012.12.010.
26. Lomholt, T. N.; Adachi, Y.; Bastos, a; Pantleon, K.; Somers, M. a J. Partial transformation of austenite in Al–Mn–Si TRIP steel upon tensile straining: an in situ EBSD study. *Mater. Sci. Technol.* **2013**, *29*, 1383–1388, doi:10.1179/1743284713Y.0000000292.
27. Haidemenopoulos, G. N.; Vasilakos, A. N. On the thermodynamic stability of retained austenite in 4340 steel. *J. Alloys Compd.* **1997**, *247*, 128–133, doi:10.1016/S0925-8388(96)02574-1.

28. Haidemenopoulos, G. N.; Katsamas, A. I.; Aravas, N. Stability and constitutive modelling in multiphase TRIP steels. *Steel Res. Int.* **2006**, *77*, 720–726, doi:10.1002/srin.200606453.

29. Brandt, M. L. Bainitic Stabilization of Austenite in Low Alloy Sheet Steels, Doctoral Thesis, Northwestern university, 1997.

30. Gong, J. Predictive Process Optimization for Fracture Ductility in Automotive TRIP Steels, Doctoral Thesis, Northwestern university, 2013.

31. Durand-Charre, M. *Microstructure of Steels and Cast Irons*; Springer, 2004; ISBN 3662087294.

32. Ghosh, G.; Olson, G. B. Precipitation of paraequilibrium cementite: Experiments, and thermodynamic and kinetic modeling. *Acta Mater.* **2002**, *50*, 2099–2119, doi:10.1016/S1359-6454(02)00054-X.

33. Olson, G. B.; Bhadeshia, H. K. D. H.; Cohen, M. Coupled diffusional/displacive transformations. *Acta Metall.* **1989**, *37*, 381–390, doi:10.1016/0001-6160(89)90222-8.

34. Olson, G. B.; Bhadeshia, H. K. D. H.; Cohen, M. Coupled diffusional/displacive transformations: Part II. Solute trapping. *Metall. Trans. A* **1990**, *21*, 805–809, doi:10.1007/BF02656563.

35. Aziz, M. J. Model for solute redistribution during rapid solidification. *J. Appl. Phys.* **1982**, *53*, 1158–1168, doi:10.1063/1.329867.

36. Mujahid, S. A.; Bhadeshia, H. K. D. H. Coupled diffusional/displacive transformations: Effect of carbon concentration. *Acta Metall. Mater.* **1993**, *41*, 967–973, doi:10.1016/0956-7151(93)90031-M.

37. Mujahid, S. A.; Bhadeshia, H. K. D. H. Coupled diffusional/displacive transformations: Addition of substitutional alloying elements. *J. Phys. D. Appl. Phys.* **2001**, *34*, 2573–2580, doi:10.1088/0022-3727/34/17/301.

38. Speer, J. G.; Streicher, A. M.; Matlock, D. K.; Rizzo, F.; Krauss, G. Quenching and partitioning: A fundamentally new process to create high strength trip sheet microstructures. In *Materials Science and Technology 2003 Meeting*; Chicago, IL, United states, 2003; pp. 505–522.

39. Edmonds, D. V.; He, K.; Rizzo, F. C.; De Cooman, B. C.; Matlock, D. K.; Speer, J. G. Quenching and partitioning martensite-A novel steel heat treatment. *Mater. Sci. Eng. A* **2006**, *438–440*, 25–34, doi:10.1016/j.msea.2006.02.133.

40. Speer, J. G.; Streicher, A. M.; Matlock, D. K.; Rizzo, F.; Krauss, G. Quenching and Partitioning A Fundamentally New Process to create high strength trip sheet microstructure Available online: https://getinfo.de/app/Quenching-and-Partitioning-A-Fundamentally-New/id/BLCP%3ACN050898361 (accessed on Apr 26, 2015).

41. De Cooman, B. C. Structure-properties relationship in TRIP steels containing carbide-free bainite. *Curr. Opin. Solid State Mater. Sci.* **2004**, *8*, 285–303, doi:10.1016/j.cossms.2004.10.002.

42. Moor, E. De; Speer, J. G.; Matlock, D. K.; Kwak, J.-H.; Lee, S.-B. Effect of Carbon and

Manganese on the Quenching and Partitioning Response of CMnSi Steels. *ISIJ Int.* **2011**, *51*, 137–144, doi:10.2355/isijinternational.51.137.

43. Kähkönen, J.; Pierce, D. T.; Speer, J. G.; De Moor, E.; Thomas, G. A.; Coughlin, D.; Clarke, K.; Clarke, A. Quenched and Partitioned CMnSi Steels Containing 0.3 wt.% and 0.4 wt.% Carbon. *JOM* **2015**, *68*, 210–214, doi:10.1007/s11837-015-1620-4.

44. Kähkönen, M. J.; De Moor, E.; Speer, J.; Thomas, G. Carbon and Manganese Effects on Quenching and Partitioning Response of CMnSi-Steels. *SAE Int. J. Mater. Manuf.* **2015**, *8*, 2015-01–0530, doi:10.4271/2015-01-0530.

45. Meyer, M. De; Vanderschueren, D.; Cooman, B. C. De The Influence of the Substitution of Si by Al on the Properties of Cold Rolled C-Mn-Si TRIP Steels. *ISIJ Int.* **1999**, *39*, 813–822, doi:10.2355/isijinternational.39.813.

46. De Moor, E.; Speer, J. G.; Föjer, C.; Penning, J. Effect of Si, Al, Mo Alloying on Tensile Properties Obtained by Quenching and Partitioning. *Proc. Mater. Sci. Technol.* **2009**, 1554–1563.

47. Morito, S.; Nishikawa, J.; Maki, T. Dislocation Density within Lath Martensite in Fe-C and Fe-Ni Alloys. *ISIJ Int.* **2003**, *43*, 1475–1477, doi:10.2355/isijinternational.43.1475.

48. Diego-calderón, I. De; Knijf, D. De; Molina-aldareguia, J. M. Effect of Q & P parameters on microstructure development and mechanical behaviour of Q & P steels. *Rev. Metal.* **2015**, *51*, 1–12.

49. Seo, E. J.; Cho, L.; Estrin, Y.; De Cooman, B. C. Microstructure-mechanical properties relationships for quenching and partitioning (Q&P) processed steel. *Acta Mater.* **2016**, *113*, 124–139, doi:10.1016/j.actamat.2016.04.048.

50. Arlazarov, A.; Bouaziz, O.; Masse, J. P.; Kegel, F. Characterization and modeling of mechanical behavior of quenching and partitioning steels. *Mater. Sci. Eng. A* **2015**, *620*, 293–300, doi:10.1016/j.msea.2014.10.034.

51. Knijf, D. De; Silva, E. P. Da; Föjer, C.; Petrov, R. Study of heat treatment parameters and kinetics of quenching and partitioning cycles. *Mater. Sci. Technol.* **2014**.

52. Kim, B.; Celada, C.; San Martín, D.; Sourmail, T.; Rivera-Díaz-del-Castillo, P. E. J. The effect of silicon on the nanoprecipitation of cementite. *Acta Mater.* **2013**, *61*, 6983–6992, doi:10.1016/j.actamat.2013.08.012.

53. Kim, B.; Sietsma, J.; Santofimia, M. J. The role of silicon in carbon partitioning processes in martensite/austenite microstructures. *Mater. Des.* **2017**, *127*, 336–345, doi:10.1016/J.MATDES.2017.04.080.

54. Zhu, C.; Cerezo, A.; Smith, G. D. W. Carbide characterization in low-temperature tempered steels. *Ultramicroscopy* **2009**, *109*, 545–552, doi:10.1016/j.ultramic.2008.12.007.

55. Zhang, J.; Ding, H.; Misra, R. D. K.; Wang, C. Enhanced stability of retained austenite and consequent work hardening rate through pre-quenching prior to quenching and partitioning in a Q-P microalloyed steel. *Mater. Sci. Eng. A* **2014**, *611*, 252–256, doi:10.1016/j.msea.2014.05.074.

56. Santofimia, M. J.; Zhao, L.; Sietsma, J. Overview of Mechanisms Involved During the Quenching and Partitioning Process in Steels. *Metall. Mater. Trans. A* **2011**, *42*, 3620–3626, doi:10.1007/s11661-011-0706-z.

57. Santofimia, M. J.; Nguyen-Minh, T.; Zhao, L.; Petrov, R.; Sabirov, I.; Sietsma, J. New low carbon Q&P steels containing film-like intercritical ferrite. *Mater. Sci. Eng. A* **2010**, *527*, 6429–6439, doi:10.1016/J.MSEA.2010.06.083.

58. Yan, S.; Liu, X.; Liu, W. J.; Liang, T.; Zhang, B.; Liu, L.; Zhao, Y. Comparative study on microstructure and mechanical properties of a C-Mn-Si steel treated by quenching and partitioning (Q&P) processes after a full and intercritical austenitization. *Mater. Sci. Eng. A* **2017**, *684*, 261–269, doi:10.1016/j.msea.2016.12.026.

59. Li, W. song; Gao, H. ye; Nakashima, H.; Hata, S.; Tian, W. huai Microstructural evolution and mechanical properties of a low-carbon quenching and partitioning steel after partial and full austenitization. *Int. J. Miner. Metall. Mater.* **2016**, *23*, 906–919, doi:10.1007/s12613-016-1306-0.

60. Clarke, A. J. Carbon Partitioning Into Austenite From Martensite In A Silicon-Containing High Strength Sheet Steel, Doctoral Thesis, Colorado school of mines, 2006.

61. Koopmans, T. T. W. Thermal stability of retained austenite in Quenching & Partitioning steels, MS Thesis, Delft University of Technology, 2015.

62. Sun, J.; Yu, H. Microstructure development and mechanical properties of quenching and partitioning (Q&P) steel and an incorporation of hot-dipping galvanization during Q&P process. *Mater. Sci. Eng. A* **2013**, *586*, 100–107, doi:10.1016/j.msea.2013.08.021.

63. HajyAkbary, F.; Sietsma, J.; Miyamoto, G.; Furuhara, T.; Santofimia, M. J. Interaction of carbon partitioning, carbide precipitation and bainite formation during the Q&P process in a low C steel. *Acta Mater.* **2016**, *104*, 72–83, doi:10.1016/j.actamat.2015.11.032.

64. Huyghe, P.; Malet, L.; Caruso, M.; Georges, C.; Godet, S. On the relationship between the multiphase microstructure and the mechanical properties of a 0.2C quenched and partitioned steel. *Mater. Sci. Eng. A* **2017**, *701*, 254–263, doi:10.1016/j.msea.2017.06.058.

65. Santofimia, M. J.; Zhao, L.; Petrov, R.; Kwakernaak, C.; Sloof, W. G.; Sietsma, J. Microstructural development during the quenching and partitioning process in a newly designed low-carbon steel. *Acta Mater.* **2011**, *59*, 6059–6068, doi:10.1016/j.actamat.2011.06.014.

66. Clarke, A. J.; Speer, J. G.; Miller, M. K.; Hackenberg, R. E.; Edmonds, D. V.; Matlock, D. K.; Rizzo, F. C.; Clarke, K. D.; De Moor, E. Carbon partitioning to austenite from martensite or bainite during the quench and partition (Q&P) process: A critical assessment. *Acta Mater.* **2008**, *56*, 16–22, doi:10.1016/j.actamat.2007.08.051.

67. Kähkönen, J. Quenching and Paritioning Response of Carbon-Manganese-Silicon Sheet Steels Containing Nickel, Molybdenum, Aluminum, and Copper Additions, Colorado School of Mines, 2016.

68. Diego Calderón, M. I. de Mechanical properties of advanced high-strength steels produced via quenching and partitioning, 2015.

69. Seo, E. J.; Cho, L.; De Cooman, B. C. Application of quenching and partitioning (Q&P) processing to press hardening steel. *Metall. Mater. Trans. A Phys. Metall. Mater. Sci.* **2014**, *45*, 4022–4037, doi:10.1007/s11661-014-2316-z.

70. Zhou, S.; Zhang, K.; Wang, Y.; Gu, J. F.; Rong, Y. H. High strength-elongation product of Nb-microalloyed low-carbon steel by a novel quenching-partitioning-tempering process. *Mater. Sci. Eng. A* **2011**, *528*, 8006–8012, doi:10.1016/j.msea.2011.07.008.

71. Sun, J.; Yu, H.; Wang, S.; Fan, Y. Study of microstructural evolution, microstructure-mechanical properties correlation and collaborative deformation-transformation behavior of quenching and partitioning (Q&P) steel. *Mater. Sci. Eng. A* **2014**, *596*, 89–97, doi:10.1016/j.msea.2013.12.054.

72. Tan, X.; Xu, Y.; Yang, X.; Liu, Z.; Wu, D. Effect of partitioning procedure on microstructure and mechanical properties of a hot-rolled directly quenched and partitioned steel. *Mater. Sci. Eng. A* **2014**, *594*, 149–160, doi:10.1016/j.msea.2013.11.064.

73. Xiong, X. C.; Chen, B.; Huang, M. X.; Wang, J. F.; Wang, L. The effect of morphology on the stability of retained austenite in a quenched and partitioned steel. *Scr. Mater.* **2013**, *68*, 321–324, doi:10.1016/j.scriptamat.2012.11.003.

74. Choi, K. S.; Zhu, Z.; Sun, X.; De Moor, E.; Taylor, M. D.; Speer, J. G.; Matlock, D. K. Determination of carbon distributions in quenched and partitioned microstructures using nanoscale secondary ion mass spectroscopy. *Scr. Mater.* **2015**, *104*, 79–82, doi:10.1016/j.scriptamat.2015.03.027.

75. De Knijf, D.; Föjer, C.; Kestens, L. A. I.; Petrov, R. Factors influencing the austenite stability during tensile testing of Quenching and Partitioning steel determined via in-situ Electron Backscatter Diffraction. *Mater. Sci. Eng. A* **2015**, *638*, 219–227, doi:10.1016/j.msea.2015.04.075.

76. Li, W. S.; Gao, H. Y.; Nakashima, H.; Hata, S.; Tian, W. H. In-situ study of the deformation-induced rotation and transformation of retained austenite in a low-carbon steel treated by the quenching and partitioning process. *Mater. Sci. Eng. A* **2016**, *649*, 417–425, doi:10.1016/J.MSEA.2015.09.076.

77. Hidalgo, J.; Findley, K. O.; Santofimia, M. J. Thermal and mechanical stability of retained austenite surrounded by martensite with different degrees of tempering. *Mater. Sci. Eng. A* **2017**, *690*, 337–347, doi:10.1016/j.msea.2017.03.017.

78. Jang, J. H.; Kim, I. G.; Bhadeshia, H. K. D. H. ε-Carbide in alloy steels: First-principles assessment. *Scr. Mater.* **2010**, *63*, 121–123, doi:10.1016/J.SCRIPTAMAT.2010.03.026.

79. Pierce, D. T.; Coughlin, D. R.; Williamson, D. L.; Clarke, K. D.; Clarke, A. J.; Speer, J. G.; De Moor, E. Characterization of transition carbides in quench and partitioned steel microstructures by Mössbauer spectroscopy and complementary techniques. *Acta Mater.* **2015**, *90*, 417–430, doi:10.1016/j.actamat.2015.01.024.

80. Pierce, D. T.; Coughlin, D. R.; Williamson, D. L.; Kähkönen, J.; Clarke, A. J.; Clarke, K. D.; Speer, J. G.; De Moor, E. Quantitative investigation into the influence of temperature on carbide and austenite evolution during partitioning of a quenched and partitioned steel.

Scr. Mater. **2016**, *121*, 5–9, doi:10.1016/j.scriptamat.2016.04.027.

81. Santofimia, M. J.; Zhao, L.; Sietsma, J. Microstructural Evolution of a Low-Carbon Steel during Application of Quenching and Partitioning Heat Treatments after Partial Austenitization. *Metall. Mater. Trans. A* **2008**, *40*, 46–57, doi:10.1007/s11661-008-9701-4.

82. Kim, D. H.; Speer, J. G.; Kim, H. S.; De Cooman, B. C. Observation of an Isothermal Transformation during Quenching and Partitioning Processing. *Metall. Mater. Trans. A* **2009**, *40*, 2048–2060, doi:10.1007/s11661-009-9891-4.

83. Toji, Y.; Matsuda, H.; Herbig, M.; Choi, P.-P.; Raabe, D. Atomic-scale analysis of carbon partitioning between martensite and austenite by atom probe tomography and correlative transmission electron microscopy. *Acta Mater.* **2014**, *65*, 215–228, doi:10.1016/j.actamat.2013.10.064.

84. Jiang, H.; Zhuang, B.; Duan, X.; Wu, Y.; Cai, Z. Element distribution and diffusion behavior in Q&P steel during partitioning. *Int. J. Miner. Metall. Mater.* **2013**, *20*, 1050–1059, doi:10.1007/s12613-013-0833-1.

85. Zhou, S.; Zhang, K.; Wang, Y.; Gu, J. F.; Rong, Y. H. The mechanism of high strength-ductility steel produced by a novel quenching-partitioning-tempering process and the mechanical stability of retained austenite at elevated temperatures. *Metall. Mater. Trans. A Phys. Metall. Mater. Sci.* **2012**, *43*, 1026–1034, doi:10.1007/s11661-011-0929-z.

86. Speer, J. G.; Assunção, F. C. R.; Matlock, D. K.; Edmonds, D. V. The "quenching and partitioning" process: background and recent progress. *Mater. Res.* **2005**, *8*, 417–423, doi:10.1590/S1516-14392005000400010.

87. Emmanuel De Moor; Gibbs, P. J.; Speer, J. G.; Matlock, D. K. Strategies for Third-Generation Advanced High-Strength SteelDevelopment. *Iron Steel Technol. 7(11)* **2010**, 133–144.

88. Lighweight Materials 2016 Annual Report. *Dep. Energy* **2017**.

89. Sun, X. *Development of 3rd Generation Advanced High Strength Steels (AHSS) with an Integrated Experimental and Simulation Approach*; 2013;

90. Smith, C. S. *A Search for Structure*; 1981; ISBN 0262191911.

91. Olson, G. B. Computational Design of Hierarchically Structured Materials. *Science (80-.).* **1997**, *277*, 1237–1242, doi:10.1126/science.277.5330.1237.

92. Olson, G. Designing a new material world. *Science (80-.).* **2000**.

93. Olson, G. B.; Cohen, M. A general mechanism of martensitic nucleation: Part II. FCC → BCC and other martensitic transformations. *Metall. Trans. A* **1976**, *7*, 1905–1914, doi:10.1007/BF02659823.

94. Ruhl, R.; Cohen, M. Splat Quenching of Iron-Carbon Alloys. In *Transactions of The Metallurgical Society of AIME*; 1969; Vol. 245, p. 241.

95. Dyson, D. J.; Holmes, B. Effect of alloying additions on the lattice parameter of austenite. *J. Iron Steel Inst.* **1970**, *208*, 469–474.

96. Larson, D. J.; Prosa, T. J.; Ulfig, R. M.; Geiser, B. P.; Kelly, T. F. *Local Electrode Atom Probe Tomography*; Springer New York: New York, NY, 2013; ISBN 978-1-4614-8720-3.

97. Miller, M. K. *Atom Probe Tomography: Analysis at the Atomic Level*; Kluwer Academic/Plenum publishers: New York, 2000;

98. Sha, W.; Chang, L.; Smith, G. D. W.; Liu Cheng; Mittemeijer, E. J. Some aspects of atom-probe analysis of FeC and FeN systems. *Surf. Sci.* **1992**, *266*, 416–423, doi:10.1016/0039-6028(92)91055-G.

99. Li, Y. J.; Choi, P.; Borchers, C.; Westerkamp, S.; Goto, S.; Raabe, D.; Kirchheim, R. Atomic-scale mechanisms of deformation-induced cementite decomposition in pearlite. *Acta Mater.* **2011**, *59*, 3965–3977, doi:10.1016/j.actamat.2011.03.022.

100. Padmanava, S. Computational Design and Analysis of High Strength Austenitic TRIP Steels for Blast Protection Applications, Doctoral Thesis, Northwestern university, 2008.

101. Larson, D. J.; Prosa, T. J.; Ulfig, R. M.; Geiser, B. P.; Kelly, T. F. Specimen Preparation. In *Local Electrode Atom Probe Tomography*; Springer New York: New York, NY, 2013; pp. 25–53.

102. Richman, R. H.; Bolling, G. F. Stress, deformation, and martensitic transformation. *Metall. Trans.* **1971**, *2*, 2451–2462, doi:10.1007/BF02814882.

103. Wang, J.; van der Wolk, P.; van der Zwaag, S. Determination of martensite start temperature in engineering steels Part I. empirical relations describing the effect of steel chemistry. *Mater. Trans.* **2000**, *41*, 761–768, doi:10.2320/matertrans1989.41.761.

104. Sourmail, T.; Garcia-Mateo, C. Critical assessment of models for predicting the Ms temperature of steels. *Comput. Mater. Sci.* **2005**, *34*, 323–334, doi:10.1016/j.commatsci.2005.01.002.

105. Johansson, C. H. Thermodynamisch begründete Deutung der Vorgänge bei der Austenit-Martensit-Umwandlung. *Arch. Eisenhüttenwes.* **1937**, *11*, 241–251.

106. Kaufman, L.; Cohen, M. Thermodynamics and kinetics of martensitic transformations. *Prog. Met. Phys.* **1958**, *7*, 165–246, doi:10.1016/0502-8205(58)90005-4.

107. Hsu, T. Y.; Hongbing, C. On calculation of Ms and driving force for martensite transformation in Fe-C. *Acta Metall.* **1984**, *32*, 343–348.

108. Ghosh, G.; Olson, G. B. Kinetics of F.C.C. → B.C.C. heterogeneous martensitic nucleation—I. The critical driving force for athermal nucleation. *Acta Metall. Mater.* **1994**, *42*, 3361–3370, doi:10.1016/0956-7151(94)90468-5.

109. Wang, J.; Wolk, P. J. van der; Zwaag, S. van der Determination of Martensite Start Temperature for Engineering Steels Part II. Correlation between Critical Driving Force and <I>M</I>s Temperature. *Mater. Trans. JIM* 2000, *41*, 769–776.

110. Grujicic, M.; Olson, G. B.; Owen, W. S. Mobility of martensitic interfaces. *Metall. Trans. A* **1985**, *16*, 1713–1722, doi:10.1007/BF02670359.

111. Grujicic, M.; Olson, G. B.; Owen, W. S. Mobility of the β1-γ 1 ′ martensitic interface in

Cu-Al-Ni: Part I. Experimental measurements. *Metall. Trans. A* **1985**, *16*, 1723–1734, doi:10.1007/BF02670360.

112. Ghosh, G.; Olson, G. B. Kinetics of F.c.c. → b.c.c. heterogeneous martensitic nucleation—II. Thermal activation. *Acta Metall. Mater.* **1994**, *42*, 3371–3379, doi:10.1016/0956-7151(94)90469-3.
113. Ghosh, G.; Olson, G. B. Computational thermodynamics and the kinetics of martensitic transformation. *J. Phase Equilibria* **2001**, *22*, 199–207, doi:10.1361/105497101770338653.
114. Stormvinter, A.; Borgenstam, A.; Ågren, J. Thermodynamically Based Prediction of the Martensite Start Temperature for Commercial Steels. *Metall. Mater. Trans. A* **2012**, *43*, 3870–3879, doi:10.1007/s11661-012-1171-z.
115. van Bohemen, S. M. C.; Morsdorf, L. Predicting the Ms temperature of steels with a thermodynamic based model including the effect of the prior austenite grain size. *Acta Mater.* **2017**, *125*, 401–415, doi:10.1016/j.actamat.2016.12.029.
116. Olson, G. B.; Tsuzaki, K.; Cohen, M. Statistical aspects of martensitic nucleation. *Mat. Res. Soc. Symp. Proc.* **1987**, *57*, 129–148, doi:10.1557/PROC-57-129.
117. Huyan, F.; Hedström, P.; Höglund, L.; Borgenstam, A. A Thermodynamic-Based Model to Predict the Fraction of Martensite in Steels. *Metall. Mater. Trans. A Phys. Metall. Mater. Sci.* **2016**, *47*, 4404–4410, doi:10.1007/s11661-016-3604-6.
118. Koistinen, D. P.; Marburger, R. E. A general equation prescribing the extent of the austenite-martensite transformation in pure iron-carbon alloys and plain carbon steels. *Acta Metall.* **1959**, *7*, 59–60, doi:10.1016/0001-6160(59)90170-1.
119. van Bohemen, S. M. C.; Sietsma, J. Effect of composition on kinetics of athermal martensite formation in plain carbon steels. *Mater. Sci. Technol.* **2009**, *25*, 1009–1012, doi:10.1179/174328408X365838.
120. Lee, S. J.; Van Tyne, C. J. A kinetics model for martensite transformation in plain carbon and low-alloyed steels. *Metall. Mater. Trans. A Phys. Metall. Mater. Sci.* **2012**, *43*, 422–427, doi:10.1007/s11661-011-0872-z.
121. Magee, C. L. The nucleation of martensite. *Phase Transform.* **1970**, 115–156.
122. Seo, E. J.; Cho, L.; De Cooman, B. C. Modified Methodology for the Quench Temperature Selection in Quenching and Partitioning (Q&P) Processing of Steels. *Metall. Mater. Trans. A Phys. Metall. Mater. Sci.* **2016**, *47*, 3797–3802, doi:10.1007/s11661-016-3579-3.
123. Lin, M.; Olson, G. B.; Cohen, M. Distributed-activation kinetics of heterogeneous martensitic nucleation. *Metall. Trans. A* **1992**, *23*, 2987–2998, doi:10.1007/BF02646117.
124. Ghosh, G.; Olson, G. B. The kinetics of lath martensitic transformation. *J. Phys. IV* **2003**, *112*, 139–142, doi:10.1051/jp4:2003851.
125. Caballero, F. G.; Santofimia, M. J.; García-Mateo, C.; de Andrés, C. G. Time-Temperature-Transformation Diagram within the Bainitic Temperature Range in a

Medium Carbon Steel. *Mater. Trans.* **2004**, *45*, 3272–3281, doi:10.2320/matertrans.45.3272.

126. Behera, A. Low temperature bainite and martensite transformations in QP steel. *ArcelorMittal Glob. R&D* **2015**.
127. Song, T.; De Cooman, B. C. Effect of boron on the isothermal bainite transformation. *Metall. Mater. Trans. A Phys. Metall. Mater. Sci.* **2013**, *44*, 1686–1705, doi:10.1007/s11661-012-1522-9.
128. Toji, Y.; Miyamoto, G.; Raabe, D. Carbon partitioning during quenching and partitioning heat treatment accompanied by carbide precipitation. *Acta Mater.* **2015**, *86*, 137–147, doi:10.1016/j.actamat.2014.11.049.
129. Seo, E. J.; Cho, L.; De Cooman, B. C. Kinetics of the partitioning of carbon and substitutional alloying elements during quenching and partitioning (Q&P) processing of medium Mn steel. *Acta Mater.* **2016**, *107*, 354–365, doi:10.1016/j.actamat.2016.01.059.
130. De Knijf, D.; Santofimia, M. J.; Shi, H.; Bliznuk, V.; Föjer, C.; Petrov, R.; Xu, W. In situ austenite–martensite interface mobility study during annealing. *Acta Mater.* **2015**, *90*, 161–168, doi:10.1016/j.actamat.2015.02.040.
131. Thomas, G. A.; Speer, J. G. Interface migration during partitioning of Q&P steel. *Mater. Sci. Technol.* **2014**, *30*, 998–1007, doi:10.1179/1743284714Y.0000000546.
132. Bhadeshia, H. K. D. H.; Christian, J. W. Bainite in steels. *Metall. Trans. A* **1990**, *21*, 767–797, doi:10.1007/BF02656561.
133. Behera, A. K.; Olson, G. B. Nonequilibrium thermodynamic modeling of carbon partitioning in quench and partition (Q&P) steel. *Scr. Mater.* **2018**, *147*, 6–10, doi:10.1016/j.scriptamat.2017.12.027.
134. Ghosh, G.; Olson, G. B. The isotropic shear modulus of multicomponent Fe-base solid solutions. *Acta Mater.* **2002**, *50*, 2655–2675, doi:10.1016/S1359-6454(02)00096-4.
135. Ohtsuka, H.; Olson, G. B. Kinetics of thermoelastic martensitic transformations. In *International symposium on shape memory materials*; Beijing, China, 1994; pp. 17–23.
136. Ohtsuka, H.; Takashima, K.; Olson, G. B. Nonthermoelastic and Thermoelastic Martensitic Transformation Behavior Characterized by Acoustic Emission in an Fe-Pt Alloy. In *Materials Research Society Symposium - Proceedings*; 1997; pp. 407–412.
137. Olson, G. B.; Hsieh, K. C.; Bhadeshia, H. K. D. H. On the critical driving force for the nucleation of displacive transformations in steels. In *Microstructures LCS '94, Iron and Steel Inst. of Japan, Tokyo.*; 1994.
138. Hsieh, K. C. On the critical driving force for the nucleation of displacive transformations in steels, MS Thesis, Northwestern university, 1994.
139. Bhadeshia, H. K. D. H.; Edmonds, D. V. The mechanism of bainite formation in steels. *Acta Metall.* **1980**, *28*, 1265–1273, doi:10.1016/0001-6160(80)90082-6.
140. Bhadeshia, H. K. D. H. Thermodynamic analysis of isothermal transformation diagrams. *Met. Sci.* **1982**, *16*, 159–165, doi:10.1179/030634582790427217.

141. Matsuda, H.; Bhadeshia, H. K. D. H. Kinetics of the bainite transformation. *Proc. R. Soc. A Math. Phys. Eng. Sci.* **2004**, *460*, 1707–1722, doi:10.1098/rspa.2003.1225.

142. Borgenstam, A.; Höglund, L.; Ågren, J.; Engström, A. DICTRA, a tool for simulation of diffusional transformations in alloys. *J. Phase Equilibria* **2000**, *21*, 269–280, doi:10.1361/105497100770340057.

143. Hilkhuijsen, P.; Geijselaers, H. J. M.; Bor, T. C.; Perdahcioğlu, E. S.; vd Boogaard, A. H.; Akkerman, R. Strain direction dependency of martensitic transformation in austenitic stainless steels: The effect of γ-texture. *Mater. Sci. Eng. A* **2013**, *573*, 100–105, doi:10.1016/j.msea.2013.02.036.

144. De Knijf, D.; Petrov, R.; Föjer, C.; Kestens, L. A. I. Effect of fresh martensite on the stability of retained austenite in quenching and partitioning steel. *Mater. Sci. Eng. A* **2014**, *615*, 107–115, doi:10.1016/j.msea.2014.07.054.

145. Jacques, P. J.; Delannay, F.; Ladrière, J. On the influence of interactions between phases on the mechanical stability of retained austenite in transformation-induced plasticity multiphase steels. *Metall. Mater. Trans. A Phys. Metall. Mater. Sci.* **2001**, *32*, 2759–2768, doi:10.1007/s11661-001-1027-4.

146. Wang, L.; Speer, J. G. Quenching and Partitioning Steel Heat Treatment. *Metallogr. Microstruct. Anal.* **2013**, *2*, 268–281, doi:10.1007/s13632-013-0082-8.

147. Haidemenopoulos, G. N.; Katsamas, A. I.; Aravas, N. Stability and Constitutive Modelling in Multiphase TRIP Steels Modelling of the Retained Austenite Stability. *Steel Res. Int.* **2006**, *77*.

148. Patel, J. R.; Cohen, M. Criterion for the action of applied stress in the martensitic transformation. *Acta Metall.* **1953**, *1*, 531–538, doi:10.1016/0001-6160(53)90083-2.

149. Olson, G. B.; Tsuzaki, K.; Cohen, M. Statistical aspects of martensitic nucleation. In *Mat. Res. Soc. Symposium Proc.*; 1987; Vol. 57, pp. 129–148.

150. Santofimia, M. J.; Petrov, R. H.; Zhao, L.; Sietsma, J. Microstructural analysis of martensite constituents in quenching and partitioning steels. *Mater. Charact.* **2014**, *92*, 91–95, doi:10.1016/j.matchar.2014.03.003.

151. Maheswari, N.; Chowdhury, S. G.; Hari Kumar, K. C.; Sankaran, S. Influence of alloying elements on the microstructure evolution and mechanical properties in quenched and partitioned steels. *Mater. Sci. Eng. A* **2014**, *600*, 12–20, doi:10.1016/j.msea.2014.01.066.

152. Arlazarov, A.; Ollat, M.; Masse, J. P.; Bouzat, M. Influence of partitioning on mechanical behavior of Q&P steels. *Mater. Sci. Eng. A* **2016**, *661*, 79–86, doi:10.1016/j.msea.2016.02.071.

153. Somani, M. C.; Porter, D. A.; Karjalainen, L. P.; Misra, R. D. K. On Various Aspects of Decomposition of Austenite in a High-Silicon Steel During Quenching and Partitioning. *Metall. Mater. Trans. A* **2013**, *45*, 1247–1257, doi:10.1007/s11661-013-2053-8.

154. Behera, A. K.; Olson, G. B. Experimental Characterization and Modeling of Carbon Partitioning in a Quench and Partition (Q&P) Steel. In *International Symposium on New Developments in Advanced High-Strength Sheet Steels*; AIST, 2017; pp. 321–329.

155. van Bohemen, S. M. C. Austenite in multiphase microstructures quantified by analysis of thermal expansion. *Scr. Mater.* **2014**, *75*, 22–25, doi:10.1016/j.scriptamat.2013.11.005.

156. Kuehmann, C. J.; Voorhees, P. W. Ostwald ripening in ternary alloys. *Metall. Mater. Trans. A* **1996**, *27*, 937–943, doi:10.1007/BF02649761.